NANYANG TECHNOLOGICAL UNIVERSITY

LEAD-FREE FERROELECTRIC FILMS BY PULSED LASER DEPOSITION

LEAD-FREE FERROELECTRIC FILMS BY PULSED LASER DEPOSITION

CHUA NGEAH THENG

CHUA NGEAH THENG

SCHOOL OF MATERIALS SCIENCE AND ENGINEERING

2010

2010

LEAD-FREE FERROELECTRIC FILMS BY PULSED LASER DEPOSITION

CHUA NGEAH THENG

School of Materials Science and Engineering

A thesis submitted to the Nanyang Technological University
in partial fulfillment of the requirement for the degree of
Doctor of Philosophy

2010

Acknowledgements

I would like to extend my deepest thanks to my supervisors, Assistance Professor Wang Junling and Professor Ma Jan for their guidance and support. I deeply appreciate Assistance Professor Wang Junling for his effort and time in discussing my project. I am very lucky to have him as my advisor, guiding me patiently in experiments, writing skill and presentation skill as well. The same gratitude goes to Professor Ma Jan, who supports me throughout my Ph. D research at Nanyang Technological University.

I would like to thank my group members under Assistant Professor Wang Junling for their helps, discussions and the most importantly their company. I would always remember the joys we had. They are Dr. Yang Pan, Dr. Zhang Zheng, Dr. Lu Chenliang, You Lu, Steve Ong Hock Guan, Zouxi, Chen Weigang, Chen Zuhuang, Jason Cheah Jun Wei, Ding Hui, Guo Rui and Rami. I would like to give my special thanks to You Lu, who shares his priceless experience and knowledge in the characterization and the deposition of $BiFeO_3$ thin film. I also would like to give my special acknowledgement to Dr. Zhang Zheng as a collaborator. His sharing of ideas and contribution on the calculation part is greatly appreciated.

I would like to thank Dr. Lu Chenliang and Peng Haiyang for their helps in low temperature measurement.

I would like to specially acknowledge the efforts of Dr. Yao Kui for his help with uv-visible spectroscopy and the bulk piezoelectric coefficient measurement.

Last but not the least, I would like to extend special thanks to my family for their loves, concerns and supports.

Table of Contents

List of Figures

List of Tables

Abstract

Lead-based ferro/piezoelectric materials, such as $Pb(Zr_{0.52}Ti_{0.48})O_3$, are widely used because of their excellent ferroelectric and piezoelectric properties near the morphotropic phase boundary. However, due to the environmental concerns associated with lead, alternative lead-free ferro/piezoelectric systems are highly demanded. Extensive research has been conducted in this direction and several promising candidates have been identified. This dissertation details our efforts in this area.

The primary work described herein are the synthesis and characterizations, in thin film form, of two promising candidates, $[(K_{0.5}Na_{0.5})_{0.97}Li_{0.03}](Nb_{0.8}Ta_{0.2})O_3$ (KNN-KNT-$L_{0.03}$T) and $Bi_{(1-x)}La_xFeO_3$ (x=0, 0.05, 0.10, 0.15 and 0.20). The textured polycrystalline KNN-KNT-$L_{0.03}$T ceramic at morphotropic phase boundary composition exhibits piezoelectric coefficient larger than that of $Pb(Zr_{0.52}Ti_{0.48})O_3$ ceramic. However, from application point of view, it is desirable to study its properties in thin film form. Epitaxial films of KNN-KNT-$L_{0.03}$T are fabricated on (001), (110) and (111)-cut single crystal $SrTiO_3$ substrates by pulsed laser deposition, which allow us to study the intrinsic properties along different crystallographic directions. The crystal structure and electrical properties are investigated and the structure-property relationship is established. $BiFeO_3$ is another promising candidate as it possesses the largest switchable polarization observed so far in any perovskite ferroelectric material. It is also the only known single-phase multiferroic that simultaneously show both antiferromagnetic and ferroelectric orders at room temperature. $BiFeO_3$ holds great promise for novel non-volatile memories, spintronic devices and as a lead-free ferro/piezoelectric material. However, despite all the attractive properties, the large coercive field and high leakage current have limited its application, which we try to address in this work. More importantly, we hope to create a morphotropic phase

boundary and improve the piezoelectric coefficient and dielectric constant of $BiFeO_3$ through substitution. Based on literature research, we choose $LaFeO_3$ as the other end member of the solution. To investigate the effects of A-site La substitution on the crystal structure, electrical and optical properties of $BiFeO_3$, $Bi_{(1-x)}La_xFeO_3$ (x=0, 0.05, 0.10, 0.15 and 0.20) epitaxial thin films are deposited on (001)-cut single crystal $SrTiO_3$ by pulsed laser deposition. The out-of-plane lattice parameter, rhombohedral angle, coercive field, remanant polarization, piezoelectric coefficient, dielectric constant and optical bandgap of $BiFeO_3$ are studied as functions of La concentration. Ab initio calculations, conducted in collaboration with Dr. Zhang Zhen, are used to explain our results and direct future investigation. A model is proposed to understand the structure-property relationship of $Bi_{(1-x)}La_xFeO_3$ epitaxial thin films.

CHAPTER 1

Introduction

This chapter gives a brief introduction to the theories of piezoelectric and ferroelectric properties. The morphotropic phase boundary in solid solution $Pb(Zr,Ti)O_3$ is presented as a model system to established a basic understanding about the topic. Promising candidates of lead-free ferro/piezoelectric systems are reviewed. The issues associated with each of the candidates are discussed, which leads to the purpose of this research. Finally, this chapter ends with a brief summary of the organization of the dissertation.

1.1 Piezoelectricity and Ferroelectricity

Crystals can be classified into 32 point groups based on the symmetry elements they possess. Among these point groups, 11 of them are centrosymmetric (existence of a center of symmetry), thus do not possess any polar properties. Crystals that belong to the remaining 21 point groups do not have centers of symmetry, so all but one (group 432, which has other symmetry operations that prohibit the polarity) exhibit electrical polarity when subjected to a stress. They are said to be piezoelectric.

Piezoelectric response describes the coupling between electrical and mechanical forces. Mechanical energy can be converted into electricity and vice versa by using piezoelectric materials. The development of an electrical polarization under applied mechanical stress is called the direct piezoelectric effect, whereas the development of a geometric strain under applied electric field is called the converse piezoelectric effect.

Out of the 20 piezoelectric point groups, 10 possess a unique polar axis. Crystals that belong to these classes are called polar because they are spontaneously polarized below certain temperatures. The amplitude of the spontaneous polarization is temperature dependent. When temperature changes, a change in the polarization can be observed, this is called the pyroelectric effect and the crystals are said to be pyroelectric.

A crystal is called ferroelectric when it possesses at least two equivalent orientations of the spontaneous polarization vector in the absence of an external electric field, and the spontaneous polarization can be switched between those orientations by an electric field. The polar states should be absolutely stable in null field. Any two of the orientation states are identical in crystal structure and differ only in electric polarization at zero applied field. Ferroelectric crystals belong to the pyroelectric and piezoelectric family, they are those pyroelectric materials that the direction of the spontaneous polarization can be switched by external electric field before the crystals break down. Ferroelectric materials exhibit spontaneous polarization only below a characteristic temperature called the Curie temperature. Above Curie temperature, the materials become paraelectric.

Ferroelectric crystals usually possess regions with uniform polarization called domains. Within a domain, all the electric dipoles are aligned in the same direction. There may be many domains in a crystal separated by interfaces called domain walls. A single domain can be obtained by domain wall motion under the application of an external electric field. The reversal of polarization in the domain is known as domain switching. This process can be characterized by the polarization-electric field (P-E) hysteresis loop as shown in Figure 1.1. Important parameters, such as coercive field (E_c), remanant polarization (P_r) and saturation polarization (P_s) are indicated.

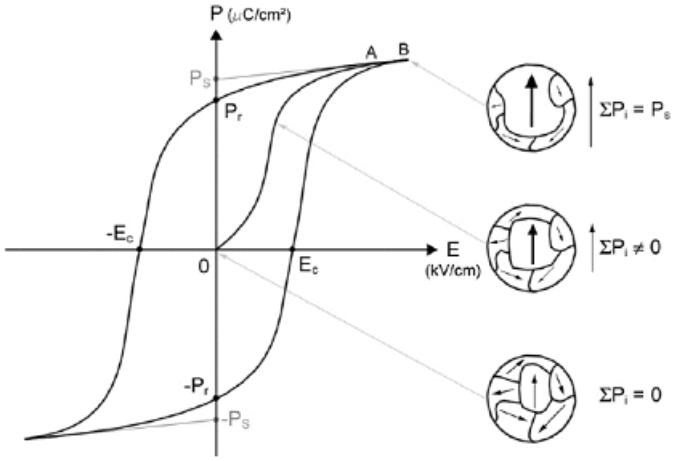

Figure 1.1. Ferroelectric hysteresis loop illustrating the polarization switching. Figure adapted from B. Reutte *et al*. [1]

Starting at the origin (zero polarization in a polydomain state), the electric field is increased, leading to domain wall motion. This will increase the size of the domains that are in the same direction as the domains can nucleate and grow. When all the domains are aligned along the field (point A), the ferroelectric loop is saturated and the polarization variation corresponds only to the linear dielectric response (non-ferroelectric). Upon decreasing of the external field, the domains remain in the same direction and the polarization decreases but remains nonzero at zero applied field. This polarization value is called the remanant polarization (Pr). Increasing towards negative field, there is a switching of the polarization direction at the coercive field of –Ec. Upon further increasing of the electric field, all the domains will be aligned in the opposite direction. Further increase in the field leads to the same linear dielectric response (non-ferroelectric). The full P-E hysteresis loop is obtained upon sweeping the external field back to the maximum value across the positive coercive field, +Ec. The spontaneous polarization +Ps is usually obtained through extrapolation to zero field of the polarization at high field. Ps is often higher larger than Pr in polycrystalline

samples but can be very close in single crystals and epitaxial thin films. The difference can be due to domain back switching after poling or the non-linear dielectric constant.

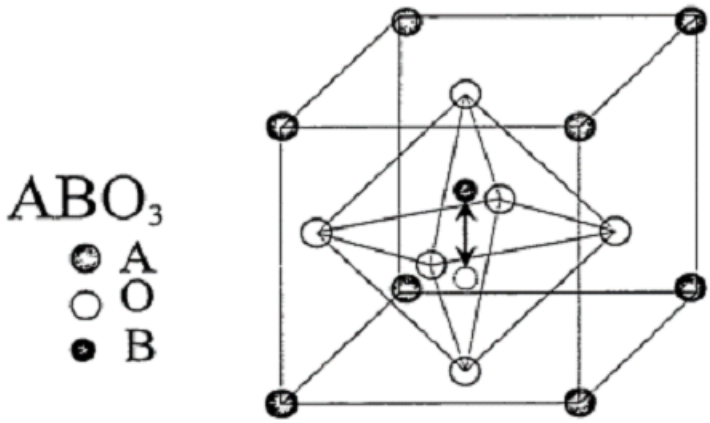

Figure 1.2. Schematic illustrating the unit cell of perovskite ferroelectric materials. Figure adapted from H. Li. [2]

Up to date, the most extensively studied and used ferro/piezoelectric materials all belong to the perovskite family. Materials in this group have the same general formula of ABO_3, where A represents a monovalent, divalent or trivalent cation, and B is typically a pentavalent, tetravalent or trivalent cation. Depending on the elements that are sitting on the A and B sites, the material can be an insulator, a conductor and/or a superconductor. Perovskite ferroelectrics usually have a cubic structure in the high symmetry paraelectric phase at high temperatures above Curie point. They undergo phase transitions, leading to a lower symmetry phases with ferroelectric characteristics. The unit cell of a well-known perovskite ferroelectric, $BaTiO_3$ is shown in Figure 1.2. The Ba^{2+} cations are located at the corners of the unit cell. A dipole moment occurs due to the relative displacements of the Ti^{4+} and O^{2-} ions from their symmetrical positions. Any lattice of oppositely signed point charges is unstable and relies on short-range interactions between adjacent electron clouds to stabilize the

structure. The hybridization of Ti 3d – O 2p orbitals in $BaTiO_3$ is one of the examples in stabilizing the ferroelectric distortion. Most perovskite ferroeletrics have B-site ions with d^0 in nature. As the lowest unoccupied energy levels are the d states, they tend to hybridize with the O 2p orbitals resulting in the double well potential.

1.2 Morphotropic Phase Boundary

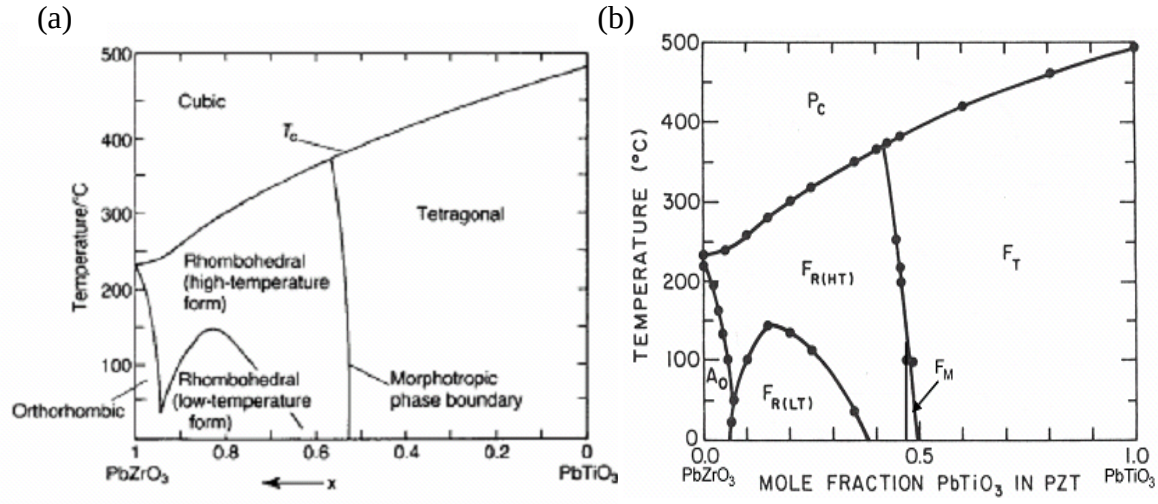

Figure 1.3. Phase diagrams illustrating (a) conventional and (b) new discovery of monoclinic phase of $Pb(Zr,Ti)O_3$ system. Figures adapted from B. Jaffe *et al.* and B. Noheda *et al.* [3, 4]

Pb-based ferroelectrics, such as $Pb(Zr,Ti)O_3$, have been extensively studied and widely used because of their excellent properties at compositions near the morphotropic phase boundary (MPB). $Pb(Zr,Ti)O_3$ is a solid solution of $PbTiO_3$ and $PbZrO_3$ with a perovskite structure. The properties of $Pb(Zr,Ti)O_3$ are composition dependent, going from the ferroelectric property of $PbTiO_3$ to the antiferroelectric property of $PbZrO_3$. The temperature-composition phase diagram of $Pb(Zr,Ti)O_3$ is shown in Figure 1.3. Except for the narrow region close to $PbZrO_3$, the ferroelectric phase diagram is divided into two regions of different symmetry, rhombohedral (space group R3m) for Zr-rich compositions and tetragonal (space group P4mm) for Ti-rich compositions. The highest piezoelectric and dielectric responses are found at the boundary between these two phases with the composition of $Pb(Zr_{0.52}Ti_{0.48})O_3$. This boundary was proposed as MPB by Jaffe *et al*, in which "morphotropic" means the boundary between two forms. The phase boundary is almost a vertical straight line, which means the transition is nearly temperature independent.

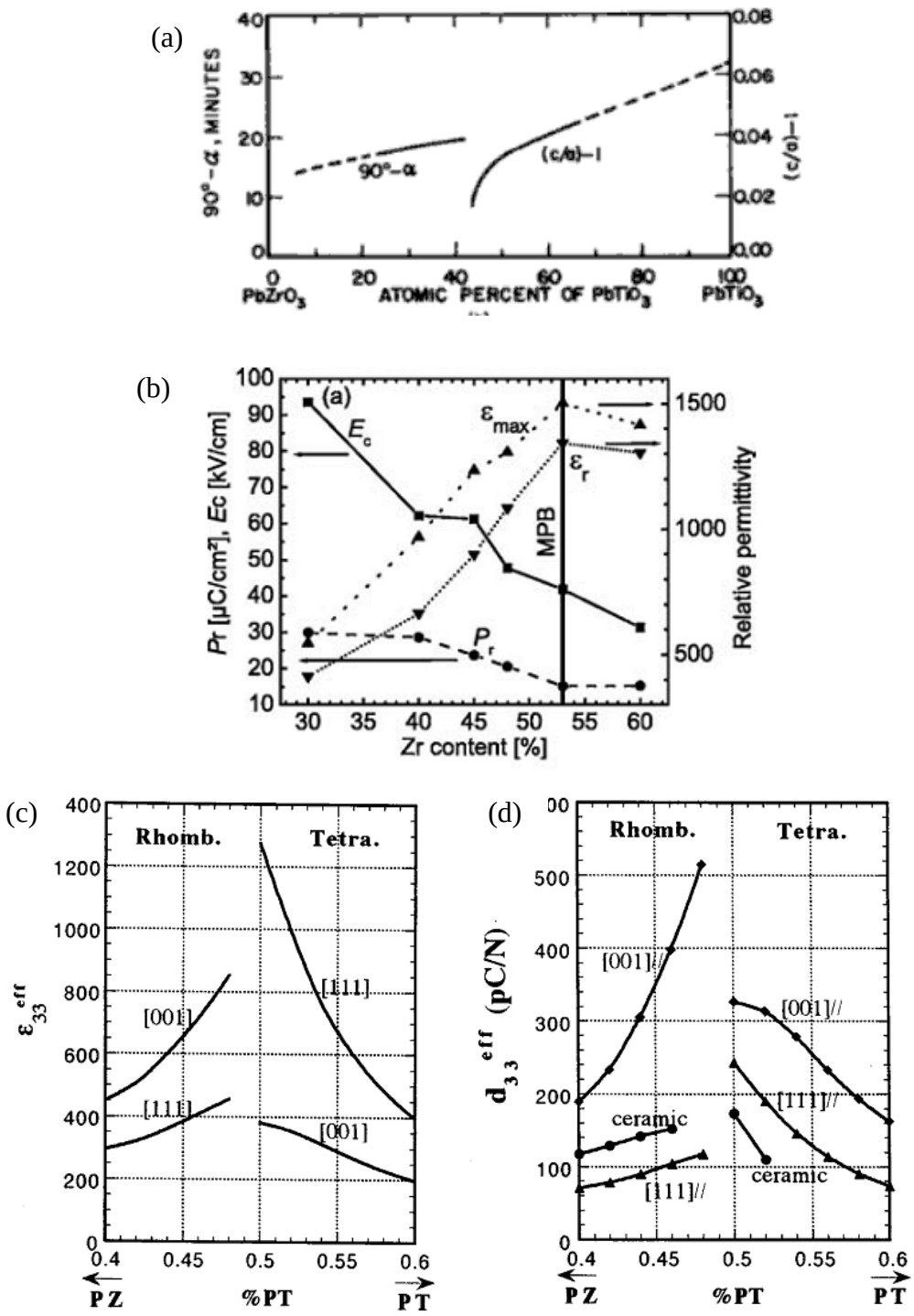

Figure 1.4 Schematics illustrating the (a) c/a, (b) remanant polarization and coercive field, (c) dielectric constants, and (d) piezoelectric coefficient, d_{33} of $Pb(Zr,Ti)O_3$ system. Figrures adapted from B. Jaffe *et al.*, P. Geber *et al.* and X. Du *et al*. [5-7]

When Zr is substituted into $PbTiO_3$, the c/a, coercive field and remanant polarization are reduced, indicating the softening of the unit cell. The excellent

properties of $Pb(Zr,Ti)O_3$ at the MPB (Figure 1.4) are believed to be associated with the softening of the unit cell and the coexistence of rhombohedral and tetragonal phases. In the tetragonal phase, there are six equivalent (100) polarization directions; whereas in the rhombohedral phase, there are eight equivalent (111) variants. At the MPB composition, the transition between the two phases implies that all these 14 directions have the same energy level. Under application of an external electric field, the large number of thermodynamically equivalent states allows a high degree of alignment of ferroelectric dipoles. The higher polarizability and the transition between the two phases induced by the external field result in enhancement of dielectric and piezoelectric responses.

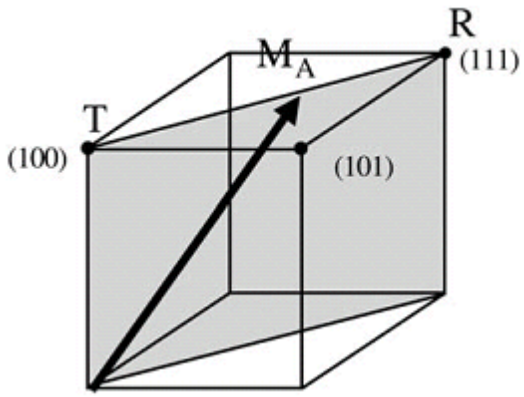

Figure 1.5. Perovskite unit cell with the polarization vector (solid arrow) in the monoclinic phase (MA) rotating between the rhombohedral (R) and the tetragonal (T) phases in the shaded region. Figure adapted from B. Noheda *et al.* [8]

Recently, the discovery of a monoclinic phase near the morphotropic phase boundary is also reported (Figure 1.3 (b)). The monoclinic region forms a narrow triangle in between the tetragonal and rhombohedral phases, with a vertical rhombohedral-monoclinic boundary and a slightly slanted tetragonal-monoclinic boundary, which agrees well with the previous phase diagram. The advantage of this structure is that the polarization vector is no longer constrained to lie along a symmetry

axis, as in the rhombohedral or tetragonal structure, but instead can rotate within the monoclinic plane (Figure 1.5). This easy rotation is believed to be responsible for the high values of the piezoelectric coefficients. Note that for $Pb(Zr,Ti)O_3$ films, the monoclinic phase is not confined to the composition of bulk MPB. It exists within a range, depends on the misfit strain.

1.3 Alternative Lead-free Ferro/piezoelectric Systems

For several decades, the field of ferro/piezoelectric materials has been dominated by lead-based perovskites, such as $Pb(Zr,Ti)O_3$, because of their high dielectric constant, large remanent polarizations and high piezoelectric coefficients. They are widely used in electromechanical devices (actuators, sensors and transducers) and extensively investigated for nonvolatile memory. [9, 10] The market for sensors alone is estimated to be tens of billions of dollars worldwide. [11, 12] Unfortunately, there are two serious environmental problems arising from lead-containing materials: atmospheric pollution caused by PbO vapor during fabrication, and the difficulty in removing lead during component recycling. Tremendous efforts have been devoted to the development of lead-free systems.

As discussed above, the physics behind the superior property of $Pb(Zr,Ti)O_3$ is relatively well understood. The stereochemical activity of the $6s^2$ lone pair of the lead ion causes large structural distortion from the prototypical cubic phase, thus a strong coupling between the electrical and structural parameters. At the same time, high sensitivity (to both electric field and stress) is caused by the competition between the different structures of the end components $PbTiO_3$ and $PbZrO_3$ at the MPB in the solid solutions. [13, 14] Recently, two lead-free systems have emerged as promising candidates. They are both designed according to the knowledge we have learned from $Pb(Zr,Ti)O_3$. One of them is based on $(K,Na)NbO_3$, the other based on $BiFeO_3$.

1.3.1 $(K,Na)NbO_3$-based Ferro/piezoelectric System

$KNbO_3$ is a high Curie temperature (Tc~418ºC) ferroelectric with orthorhombic structure (a=5.6950Å, b=5.7213Å and c=3.9739Å). In contrast, $NaNbO_3$ is a room temperature antiferroelectric, which transforms to a metastable ferroelectric phase upon application of an electric field. $NaNbO_3$ also has orthorhombic structure with a=5.506Å, b=5.566Å and c=15.52Å.

Solid solution of $KNbO_3$ and $NaNbO_3$, $K_xNa_{1-x}NbO_3$, shows ferroelectricity when x<0.97 but its piezoelectric properties are not satisfactory in comparison with that of $Pb(Zr,Ti)O_3$. MPB was found at around x=0.50 separating two orthorhombic phases with different lattice parameters. $(K,Na)NbO_3$ ceramics sintered by conventional method show relatively low piezoelectric coefficient (d_{33}~80 pm/V) due to the difficulty in obtaining dense ceramics. [15, 16] The reasons for the poor sinterability are the low melting point of $KNbO_3$ and the fact that alkaline metal elements are easily evaporated at high temperatures. However, denser $(K,Na)NbO_3$ ceramics (~99% of the theoretical density) sintered by using hot press technique show higher piezoelectric coefficient (d_{33}~160 pm/V). But it is still not comparable to that of soft $Pb(Zr,Ti)O_3$, which has piezoelectric coefficient of over 200 pm/V. [15, 16] Such technique is also not appropriate for industrial use. In addition, it is not clear whether an MPB separating two orthorhombic phases can lead to a large piezoresponse. Thus, other perovskite compounds are added to form solid solutions with $(K,Na)NbO_3$. Dense $(K,Na)NbO_3$-$SrTiO_3$ and $(K,Na)NbO_3$-$BaTiO_3$ ceramics (~98% of the theoretical density) have been studied. They exhibit a crossover from typical ferroelectric to ferroelectric relaxor behavior at certain concentration of substitution. Unfortunately, the piezoresponse was decreased. [17, 18]

$LiNbO_3$ is another component that has been studied. Although both $(K,Na)NbO_3$ and $LiNbO_3$ have octahedral NbO_6 basic structure units, $(K,Na)NbO_3$ has the perovskite structure with space group Amm2 whereas $LiNbO_3$ has the heavily distorted perovskite structure with space group R3c. At low $LiNbO_3$ concentrations, Li replaces Na and K on the A sites of the ABO_3 perovskite structure and forms solid solution, leading to a linear shift of T_c to higher temperature. The structure of solid solution transforms from orthorhombic to tetragonal symmetry due to the large distortion caused by Li^+. An MPB between orthorhombic and tetragonal phases has been found at around 6% $LiNbO_3$. At high concentration of $LiNbO_3$, the incorporation of Li into A sites of $(K,Na)NbO_3$ becomes difficult. The piezoelectric coefficient is 200-235 pm/V at this composition, which is partially attributed to the increased density due to the $LiNbO_3$ content. However, the density decreases at high $LiNbO_3$ concentration due to the formation of $K_3Li_2Nb_5O_{15}$ which has lower density (theoretical density: 4.376 g/cm^3). [19]

Similarly, tantalum modified ceramics of composition $(K,Na)(Nb,Ta)O_3$ have also been shown to exhibit improved properties compared to that of $(K,Na)NbO_3$. A piezoelectric coefficient of 270 pm/V has been reported. [20] However, Ta substitution causes a decrease in the Curie temperature of $(K,Na)NbO_3$.

By incorporation both $LiNbO_3$ and $LiTaO_3$ in the $(K,Na)NbO_3$ system, it is expected that the piezoelectric response can be improved even more. $\{(K_{0.5}Na_{0.5})_{1-x}Li_x\}(Nb_{1-y}Ta_y)O_3$ (KNN-KNT-LT) displaces an MPB between $(K,Na)NbO_3$ and hexagonal pseudo-ilmenite-type $LiTaO_3$ (Tc = 615 ºC) at (x, y)=(0.03, 0.80) (KNN-KNT-$L_{0.03}$T, denoted as LF3 in Figure 1.6). The Curie temperature is tunable between 170 and 500 ºC where additions of Li and Ta elements shift the Curie temperature higher and lower, respectively. The piezoelectric coefficient of KNN-KNT-$L_{0.03}$T was

found to be 230 pm/V which is comparable to that of $Pb(Zr_{0.52}Ti_{0.48})O_3$ (200 pm/V). The textured KNN-KNT-$L_{0.03}$T ceramic (denoted as LF3T in Figure 1.6) shows piezoelectric coefficient up to 373 pm/V. However, a complicated topochemical microcrystal conversion (TMC) process is needed to create the template for the reactive-templated grain growth. [21, 22]

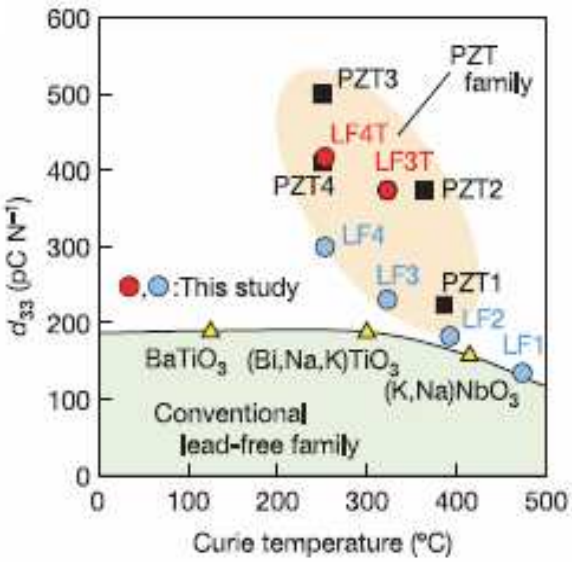

Figure 1.6. Comparison of piezoelectric coefficient,d_{33} among developed lead-free (LF) ceramics and conventional $Pb(Zr,Ti)O_3$ ceramics as a function of Curie temperature. LF1, LF2 and LF3 are (x,y) = (0.06,0), (x,y) = (0.04,0.10) and (x,y) = (0.03,0.20), respectively. LF4: $(K_{0.44}Na_{0.52}Li_{0.04})(Nb_{0.86}Ta_{0.10}Sb_{0.04})O_3$. LF3T and LF4T: textured ceramics with the same compositions as LF3 and LF4, respectively. PZT1: $Pb(Zr_{0.52}Ti_{0.48})O_3$. PZT2: $Pb_{0.988}(Zr_{0.48}Ti_{0.52})_{0.976}Nb_{0.024}O_3$. PZT3: commercially available PZT. PZT4: $\{(Pb_{0.85}Ba_{0.15})_{0.9925}La_{0.005}\}(Zr_{0.52}Ti_{0.48})O_3$. Figure adapted from Y. Saito *et al.*[21, 22]

The $(K,Na)NbO_3$-based ferro/piezoelectric system has been studied extensively in ceramic form. Thin film studies, which are very important from application point of view, are scarce.

1.3.2 $BiFeO_3$-based Ferro/piezoelectric System

I) $BiFeO_3$-based Ferro/piezoelectric System and the Challenges

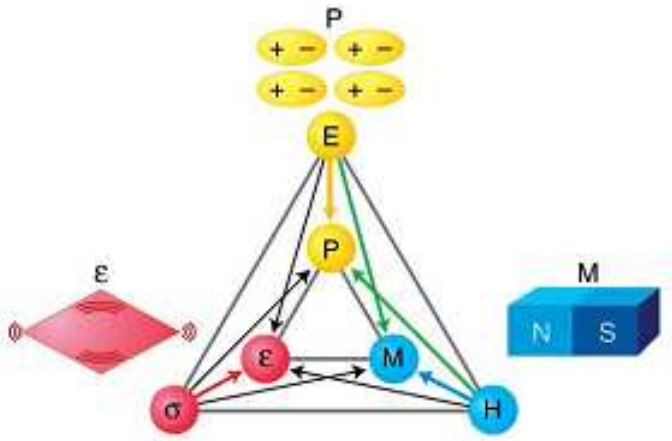

Figure 1.7. Schematic illustrating different types of coupling. (E is electric field, H is magnetic field, σ is mechanical stress, P is polarization, M is magnetization and ε is strain.) Figure adapted from N. A. Spaldin *et al.*[23]

Multiferroic materials possess at least two of the ferroic properties, i.e. ferroelectric, ferromagnetic and ferroelastic, simultaneously. In a broader context, it also includes the antiferroic orders. Interests in multiferroic materials arise because of the possible coupling effects (Figure 1.7) among the ferroic order parameters i.e. magnetoelectricity, piezoelectricity and piezomagnetism (magnetostriction). In a multiferroic materials that possesses both ferroelectricity and magnetism, besides the normal functionalities where the electric field reorients polarization or magnetic field reorients magnetization, there is also the possibility of controlling magnetization using electric field and vice versa. This additional functionality opens up tremendous possibilities for future electronic and spintronic devices. One example is the state-of-the-art magnetic storage system (magnetic random access memory, MRAM) in which an antiferromagnet is used to pin a preferred magnetization direction in the ferromagnetic layer. Although MRAM is under intensive development, a critical issue is related to the fact that these are, in principle, current driven devices and therefore

pose a concern for power consumption. If magnetization can be controlled by electric field, power consumption will be dramatically decreased. Similarly, the coupling between magnetic and elastic orders is known as piezomagnetism (magnetostriction), which describes the phenomena that a change of strain can be induced by a magnetic field and vice versa. For the piezoelectricity coupling between the electric and elastic orders, strain can be change by an applied electric field and vice versa.

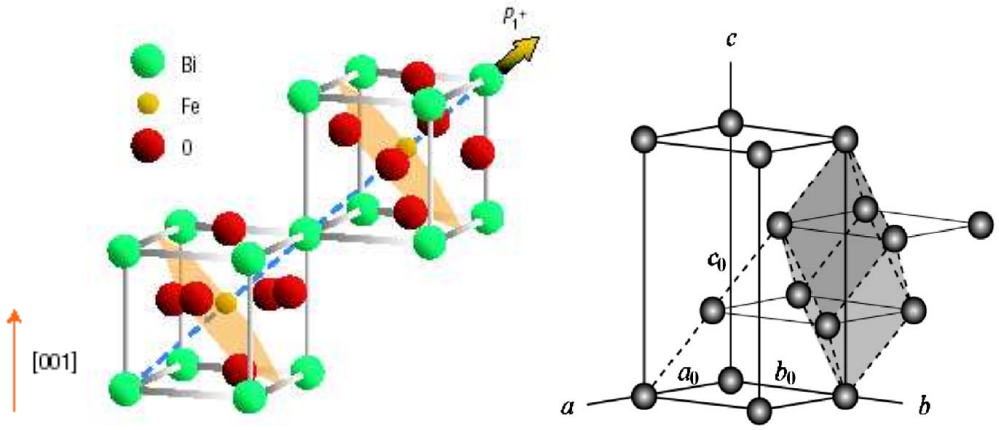

(a) (b)

Figure 1.8. Schematic structure of (a) $BiFeO_3$ and (b) atomic configuration of rhombohedral crystal system. Figures adapted from T. Zhao *et al.* and H. Uchida *et al.* [24, 25]

$BiFeO_3$ is the only known single phase multiferroic materials at room temperature. It has a high Curie temperature of 850^{o}C and shows G-type antiferromagnetism with Néel temperature of 370 ^{o}C. The structure is characterized by two distorted perovskite unit cell (a_r=3.96 Å, α_r=0.6 ^{o}) connected along body diagonal (Figure 1.8 (a)), denoted as pseudocubic <111>, to build the rhombohedral unit cell with space group R3c. [26] The hexagonal $[001]_H$ direction is equivalent to the pseudocubic $[111]_C$ direction (Figure 1.8 (b)), about which there is a threefold rotation symmetry, and along which the Bi^{3+} cations are displaced relative to the FeO_6 octahedra. [27] The large displacement is due to the stereochemically active lone-pair

orbital of Bi^{3+} ($6s^2$). Therefore, the ferroelectric polarization in $BiFeO_3$ can have directions along four cube diagonals <111>. The magnetic ordering in $BiFeO_3$ is rather complicated. Basically, $BiFeO_3$ has G-type antiferromagnetic configuration, where each Fe^{3+} is surrounded by six antiparallel nearest neighbors. [28] Within the pseudocubic (111)c surface, the magnetic moments of Fe ions are aligned in the same direction. Between the neighboring planes, they point in opposite directions. A small canting of the magnetic moments exists, which is expected to lead to weak ferromagnetic response of $BiFeO_3$. But this is usually not observed due to a cycloidal modulation with a long period of 620±20 Å. The spiral direction q lies in the hexagonal base plane and can vary its direction within the base plane. [29]

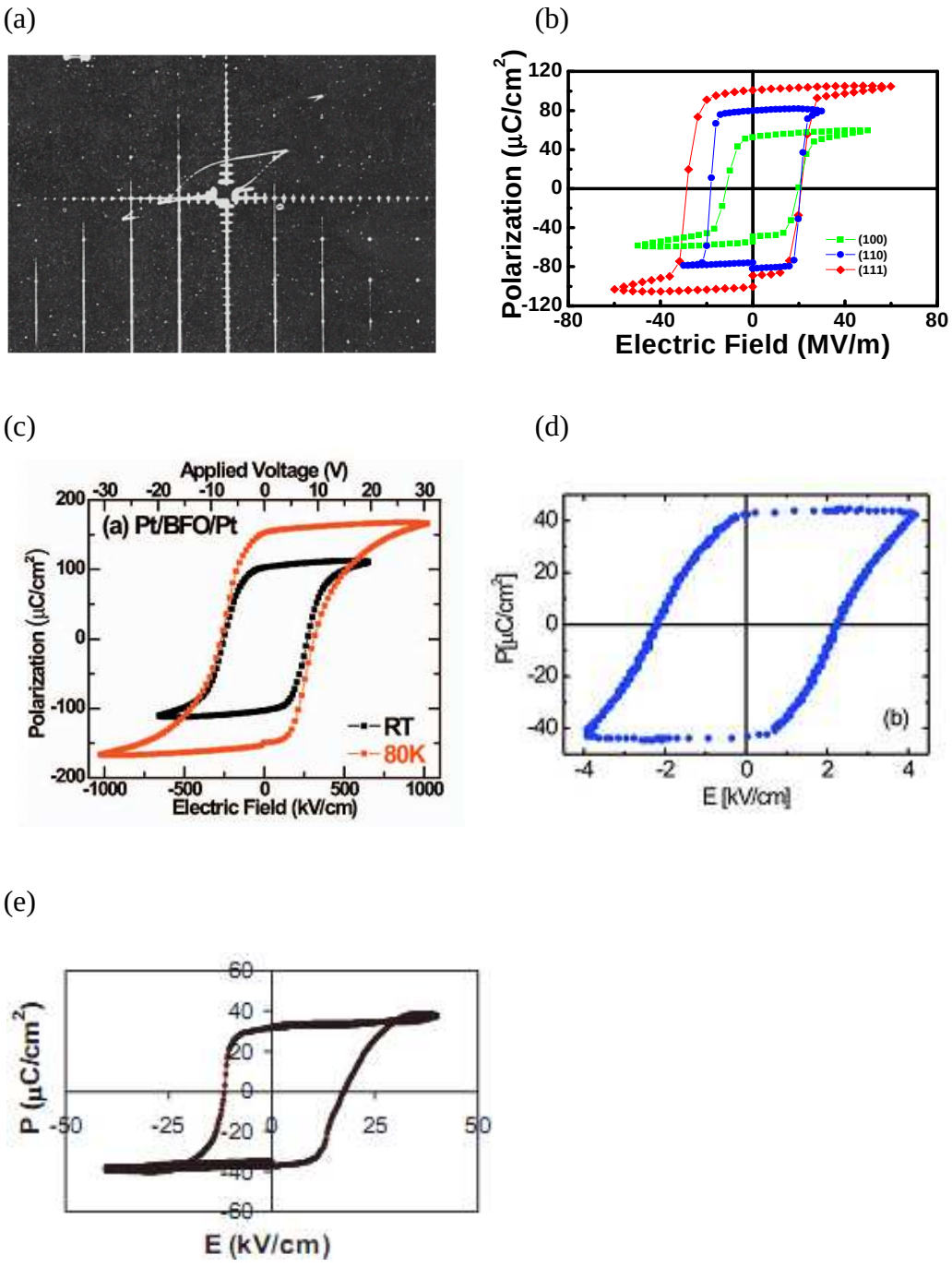

Figure 1.9. P-E hystresis loops of $BiFeO_3$ (a) single crystal in the early of 1960s, Teague *et al*. [30] (b) epitaxial thin film, Wang *et al*. [31], (c) polycrystalline film, Kwi *et al*.[32], (d) ceramic[33], Shvartsman *et al.* and (e) single crystal (polarization along (012) direction), Lebeugle *et al*.[34]

In the early 1960s, an unsaturated small polarization of $BiFeO_3$ single crystal was reported (Figure 1.9 (a)). The measured spontaneous polarization at liquid nitrogen temperature is just 3.5 $\mu C/cm^2$ along [100] direction and corresponds to 6.1 $\mu C/cm^2$ along [111] direction. The polarization is much smaller than expected as $BiFeO_3$ has high Curie temperature and large distortion. [30] In 2003, Wang *et al.* fabricated epitaxial $BiFeO_3$ films (Figure 1.9 (b)) and demonstrated remanant polarization of an order magnitude higher than the previously reported value, which is 55 $\mu C/cm^2$, 80 $\mu C/cm^2$ and 100 $\mu C/cm^2$ along (001), (110) and (111) directions, respectively. The values measured along (001)c and (110)c directions correspond well to the projections from (111)c and indicate that the spontaneous polarization lies close to (111). Initially, the large polarization in epitaxial thin films grown on single crystal substrate was thought to be due to strain enhancement. [31] However, later remanat polarization of 90 $\mu C/cm^2$ at 80 K was obtained for $BiFeO_3$ polycrystalline film prepared on $Pt/Ti/SiO_2/Si$ substrate via a chemical solution method. [35] Yun *et al.* reported well-saturated hysteresis loop and large remanant polarization (160 $\mu C/cm^2$ at 90 K; 110 $\mu C/cm^2$ at room temperature) in polycrystalline tetragonal $BiFeO_3$ thin film grown on $Pt/TiO_2/SiO_2/Si$ substrate by pulsed laser deposition. These observations suggest that heteroepitaxial strain may not be the origin of the observed large polarization. [32] Then, in 2007 Lebeugle et al reported large polarization of 60 $\mu C/cm^2$ along (001)c direction in a single crystal sample, indicating the polarization of bulk $BiFeO_3$ is intrinsically high. The representative P-E hysteresis loops of $BiFeO_3$ single crystal, polycrystalline film, epitaxial film and ceramic are shown in Figure 1.9.

Significant progress has been made recently in the research of $BiFeO_3$. The coupling between the antiferromagnetic and ferroelectic order parameters has been demonstrated in epitaxial $BiFeO_3$ films. [24] Moreover, direct evidence for a strong

exchange interaction between the ferromagnetic CoFe and the magnetoelectric/ multiferroic $BiFeO_3$ grown on $SrRuO_3/SrTiO_3$ (001) substrate has been achieved. [36] All these results clearly demonstrate the possibility of controlling magnetization with electric field. However, research on $BiFeO_3$-based lead-free ferro/piezoelectric systems has only begun recently. Generally, the goals in this aspect are to decrease the coercive field of $BiFeO_3$, to increase its resistivity, and to improve its dielectric and piezoelectric responses. In this project, we will only focus on tunning the ferro/piezoelectric properties of $BiFeO_3$ through chemical substitution. There are three main goals: (1) to increase the resistivity of $BiFeO_3$; (2) to decrease the coercive field of $BiFeO_3$; and (3) to create an MPB with improved dielectric and piezoelectric responses. High leakage current has always been a serious problem for the study and applications of $BiFeO_3$. It has been attributed to the presence of Fe^{2+} and oxygen vacancies. The evaporation of relatively volatile bismuth during the growth process and possible valence fluctuations of Fe ions (Fe^{3+} to Fe^{2+}) will create oxygen vacancy for charge compensation. [37, 38] The dominating defect chemistry in $BiFeO_3$ is still under debate. Depending on the relative vacancy concentrations, $BiFeO_3$ can be either p- or n-type. For example, oxygen vacancies are known to contribute electrons to the conduction band. Other contributors to leakage current are impurity phase, porosity, surface roughness, domain structure and interface effect. Such high leakage current would cause failure or reliability problem of the devices. It also has been shown that the magnetoelectric measurements are easily corrupted in the presence of large leakage current. [39] Therefore, it is necessary to search for a promising substitution that is capable in suppressing the charge defects.

The extremely large distortion in $BiFeO_3$ leads to large polarization, but rather small susceptibilities as compared with the widely used $Pb(Zr,Ti)O_3$. The remanant

out-of-plane piezoelectric coefficient for a (001) oriented epitaxial $Pb(Zr_{0.52}Ti_{0.48})O_3$ thin film with the thickness of 200 nm is 100 pm/V. [40] Thus, we aim to soften the $BiFeO_3$ unit cell by chemical substitution and hope to create an MPB with larger dielectric constant and piezoelectric coefficient.

II) Morphotropic Phase Boundary in $BiFeO_3$-based Ferroelectric System

The large spontaneous polarization of $BiFeO_3$ has triggered intensive research activities on using it as an end-member to create a lead-free high performance ferro/piezoelectric system. Several groups have attempted different methods to improve the ferroelectric properties of $BiFeO_3$. These methods include adopting double-layered structure [41, 42], forming solid solution with other perovskite ferroelectrics ($PbTiO_3$, $BaTiO_3$, $Pb(Zr,Ti)O_3$) [43-45], doping isovalent ions at A or B sites (La [46-61], Yb [62], Nd [25, 46, 50, 63, 64], Tb [65], Sm [66] at Bi sites and Mn [67], Cr [68-70] at Fe sites), doping diamagnetic elements on A site [71] (Ca, Sr, Pb, Ba), substituting higher valence ions (Ti [49, 72], Ni [72], Nb, Pr [73]) at Fe sites, co-doping (Ni and La [47]; Ti and La [49]; Nb and La [74]; Nd and Mo [64]), controlling annealing conditions [59] and depositing $BiFeO_3$ on different types of substrates and/or electrodes [58, 74-76]. Replacing Bi or Fe in $BiFeO_3$ remains to be the most effective method of tuning its properties.

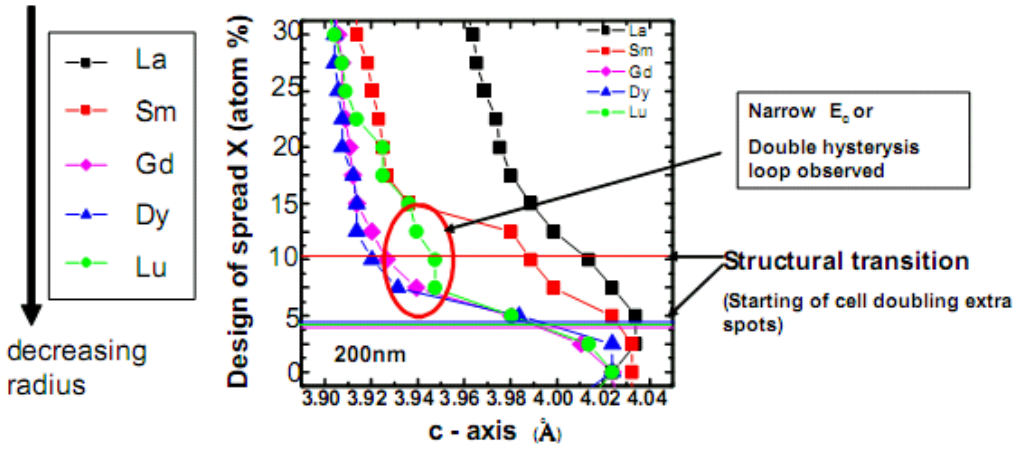

Figure 1.10. Out-of-plane lattice constant of rare earth-substituted $BiFeO_3$ thin films mapped by scanning X-ray microdiffraction. Figure adapted from S. Fujino *et al*. [77]

Shigehiro Fujino *et al*. have also studied the effect of rare earth dopants on the structure and electrical properties of $BiFeO_3$. The elements that have been tested are La, Sm, Gd, Dy and Lu with ionic radius decreasing from 1.36 Å for La^{3+} to 1.14 Å for Lu^{3+}. It is observed that the lattice constants decrease as the dopant concentration increases in every system as shown in Figure 1.10. For element with smaller ionic radius, it was found that a lower concentration was needed to induce phase transition.

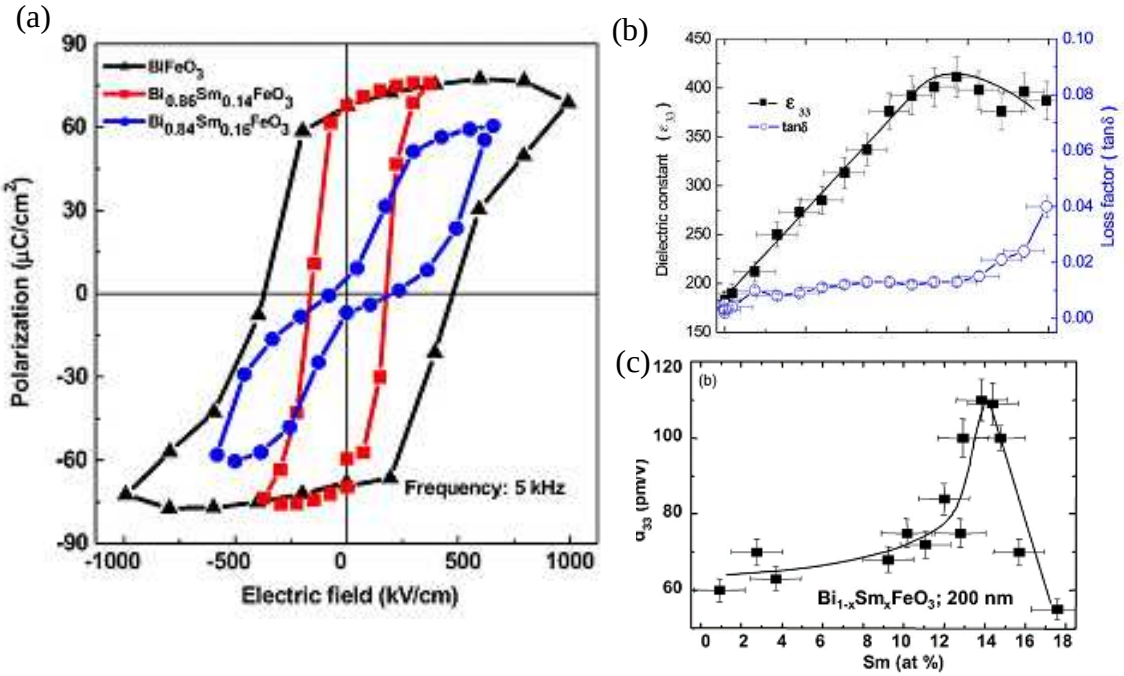

Figure 1.11. Schematics illustrating (a) P-E hysteresis loops, (b) dielectric constant and (c) piezoelectric coefficient, d_{33} of (Bi,Sm)FeO_3 thin films. Figures adapted from S. Fujino *et al.* [66]

Out of the systems that Fujino *et al*. have investigated, Sm-substituted $BiFeO_3$ was the first reported $BiFeO_3$-based system that possesses an MPB. The MPB composition was identified by using combinatorial thin film technique, where one single sample contains regions that have compositions ranging from one end member to the other. It is a fast way to test the composition dependent properties. [78] The (Bi,Sm)FeO_3 system exhibits dielectric constant and piezoelectric coefficient comparable to that of the (001) oriented $Pb(Zr_{0.52}Ti_{0.48})O_3$ epitaxial thin film at around

$(Bi_{0.86}Sm_{0.14})FeO_3$. (Figure 1.11) This composition is reported to be a boundary where rhombohedral (ferroelectric) transforms into pseudo-orthorhombic (antiferroelectric) structure. Note that the coercive field is reduced with Sm doping. The triclinic phase close to the MPB is believed to be responsible for the enhanced properties as the polarization vector is no longer constrained to a symmetry axis but instead can rotate within a plane. [8] Goldschmidt factor for Sm-doped $BiFeO_3$ is less than one as Sm^{3+} (1.24 Å) has smaller ionic size than Bi^{3+} (1.38 Å). Thus, a lower symmetry phase than both the end members (orthorhombic $SmFeO_3$ and rhombohedral $BiFeO_3$) i.e. triclinic is likely to form at the boundary. [66]

Motivated by this report, we have chosen to investigate the effect of La substitution on the properties of $BiFeO_3$. In fact, La^{3+} is probably the most studied isovalent substitute in BFO for Bi^{3+}. This is because the La doping was found effective in enhancing the ferroelectric properties of bismuth-based ferroelectrics, such as $SrBi_4Ti_4O_{15}$ [79], $Bi_4Ti_3O_{12}$ [80] and $SrBi_2Ta_2O_9$ [81]. The oxygen vacancy is reduced by the stabilized oxygen octahedron. Most La-doped $BiFeO_3$ thin films have been grown by pulsed laser deposition (PLD) [51, 54-56, 74], rf-magnetron sputtering [52, 53, 61] and chemical solution deposition methods [47-50, 57-60, 75, 82]. However, a wide range of structure and electrical properties of La-substituted $BiFeO_3$ films has been reported. Literatures on ceramics, epitaxial thin films and polycrystalline films are reviewed and summarized in the following paragraphs.

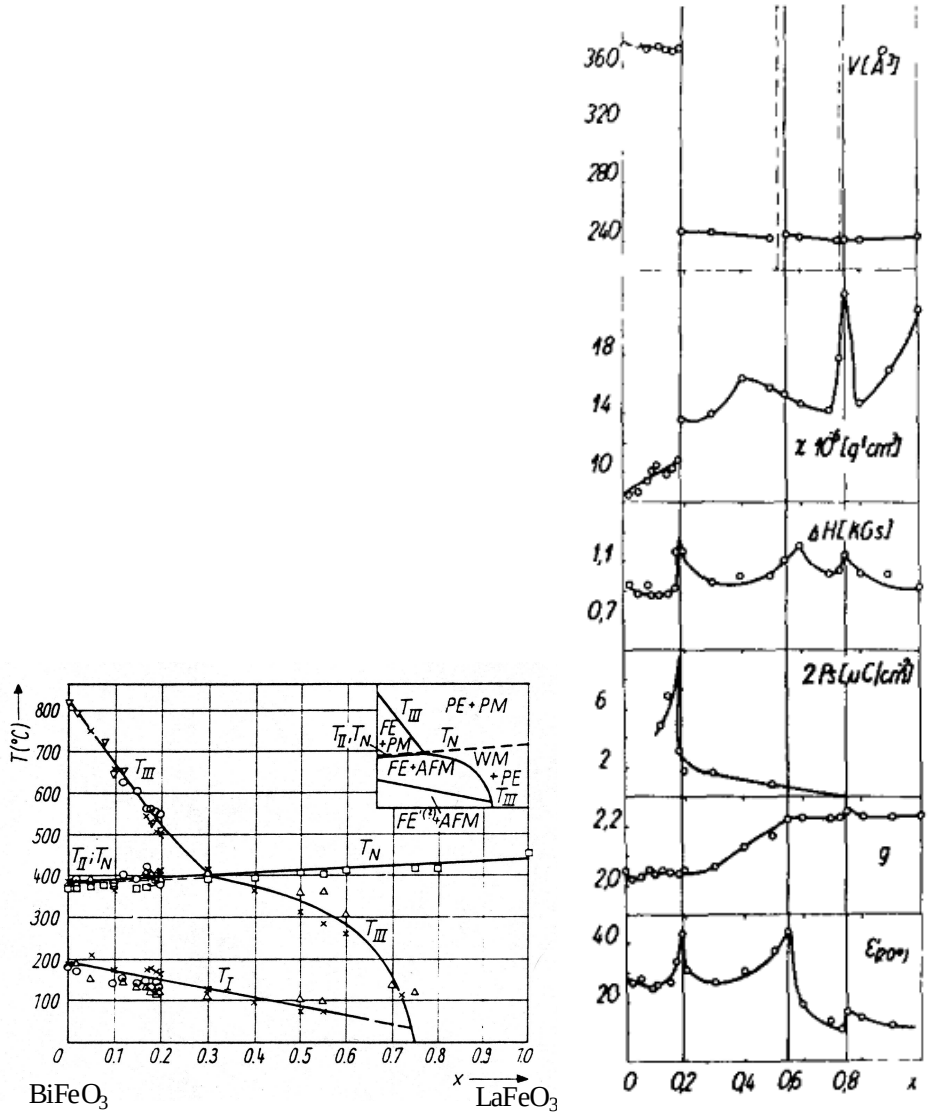

Figure 1.12 Phase diagram of $BiFeO_3$ and $LaFeO_3$ solid solution and its properties obtained from ceramic samples based on XRD analysis. Figure adapted from Polosmka *et al.*[83]

The first phase diagram of $Bi_{(1-x)}La_xFeO_3$ system was reported by Polomska *et al*, as shown in Figure 1.12. They studied the changes in dielectric constant and unit cell volume as a function of La concentration. The first phase transition with a sharp volume contraction was found at x=0.20, accompanied by a sudden drop in the spontaneous polarization and an increase in dielectric constant. Another phase transition leading to the orthorhombic Pnma (centric) phase of pure $LaFeO_3$ was found at x=0.75. [83] Of course, the quality of the ceramic samples may have limited the

accuracy of these observations. Later on, well-saturated P-E loops have been achieved in $Bi_{(1-x)}La_xFeO_3$ ceramics, but the crystal structures and phase transition points still vary from report to report. [84-86] Shan-Tao Zhang *et al*. observed phase transition from rhombohedral to orthorhombic at composition near to x=0.30, where the remnant polarization value was maximized. [84, 85] However, A.V.Zslesskii *et al* observed a transition point near to x=0.20 whereas Yuan-Hua Lin *et al*. [87, 88] observed the transition point at x=0.15. [89]According to Z. X. Cheng et al., the rhombohedral structure is maintained at x<0.10, but changes to orthorhombic at x=0.2 and tetragonal at x=0.3. These investigations have all been conducted using ceramic samples.

The effect of La doping on the structure and properties of $BiFeO_3$ thin films are even more complicated due to the effects of substrates. It is reported that for $Bi_{(1-x)}La_xFeO_3$ (x=0, 0.08 and 0.15) epitaxial thin films grown by pulsed laser deposition on $SrTiO_3$ substrates, the films undergo a transition from monoclinic to tetragonal owing to the presence of compressive strain. Better resistance to fatigue resistance is observed. [51] Using the same deposition method, Y. H. Chu *et al.* integrated La-doped $Bi_{(1-x)}La_xFeO_3$ (x=0, 10, 15 and 0.20) on Si substrate using $SrTiO_3$ template layer with $SrRuO_3$ bottom electrode. Consistent with the bulk data from A.V. Zslesskii *et al.*, Chu *et al.* reported that the La-substituted $BiFeO_3$ at x<0.15 is rhombohedral with changes in tilting angles but no structure distortions; and it transforms to orthorhombic structure at x=0.20. A significant reduction of the coercive field from 200 kV/cm for the pure $BiFeO_3$ film to 90 kV/cm is observed for the 15% La-doped $BiFeO_3$ film and this is attributed to the tuning of rhombohedral angles. They also pointed out that the lower coercive field is the result of smaller domain size, which will give rise to higher domain wall density. This result is consistent with that reported by Kalinin *et al.*, where the domain wall is responsible for low nucleation voltage. [90]

The large mismatch between the thermal expansion coefficient of $BiFeO_3$ and Si may be a reason behind the different domain structures. No ferroelectric behavior was observed at x=0.20 as a consequence of the structural change to the nonferroelectric, orthorhombic phase. The dielectric response increases with the La content and is in agreement with the bulk data from V. L. Mathe *et al*. However, no study is carried out to investigate the influence of La on piezoresponse. [56]

S. R. Das *et al.* deposited 400 nm $Bi_{(1-x)}La_xFeO_3$ (x=0, 0.05, 0.10, 0.15, 0.20) polycrystalline thin films on $Pt/TiO_2/SiO_2/Si$ substrates by pulsed laser deposition. They reported that secondary phases are eliminated, leakage currents were reduced and dielectric response was increased with substitution of La. However, they did not manage to get well-saturated hysteresis loops. [54] F. Gao *et al.* prepared 20% La-doped $BiFeO_3$ thin film using the same type of substrate and deposition technique. However, they introduced Fe^{2+} into the films to enhance the magnetization. Although higher leakage is observed in their La-doped $BiFeO_3$ thin films with bismuth oxide and Fe^{2+}, they are still able to get decent hysteresis loops, in drastic contrast to other reports. With La-doping, the coercive field, 2Ec, and remanent polarization, 2Pr, are increased from 440 kV/cm to 610 kV/cm and 10.7 $\mu C/cm^2$ to 49.6 $\mu C/cm^2$, respectively. It is reported that La doping has helped to improve the ferroelectric polarization through a structure transition from rhombohedral to monoclinic. The enhanced ferroelectric property was also claimed to be due to more Fe^{2+} ions introduced in La-doped $BiFeO_3$ and it was stated that the origin of Fe^{2+} was the presence of oxygen vacancy. [55]

Yi-Hsien Lee *et al.* reported enhancements of remnant polarization (60 $\mu C/cm^2$ to 80 $\mu C/cm^2$) and electric response as well as a smaller coercive field (450 kV/cm to 256 kV/cm) in 5% La-doped $BiFeO_3$ polycrystalline thin film on

$BaPbO_3$/Pt/TiO_x/SiO_2/Si substrate by rf-magnetron sputtering. No phase transition is reported and the enhancements are attributed to the increase of crystallinity and lattice volume. [52] They have also deposited epitaxial La-doped $BiFeO_3$ thin film on $LaFeO_3$-buffered MgO (001) substrates with $LaNiO_3$ as the bottom electrode. The improved properties with La doping are not convincing as their $BiFeO_3$ deposition is not optimized. [53] Using the same deposition method, Y. Wang *et al.* deposited La-doped $BiFeO_3$ polycrystalline thin films on platinized Si substrates with $SrRuO_3$ as the buffer layer. The lattice parameters and orientations are modified by doping La. Relatively small change in the remanant polarization at 20% La (Pr~128 to 111 $\mu C/cm^2$) is attributed to the preferred orientation along (111) direction. There is a remarkable decreased in 2Ec from 1080 kV/cm to 620 kV/cm. However, the reported coercive field of pure $BiFeO_3$ is very large in comparison with other reported value. The large Ec may be due to a higher concentration of charged defects, which serve as pinning centers that makes domain wall motion difficult. Dielectric response and fatigue resistance are also improved with La-doping. [61]

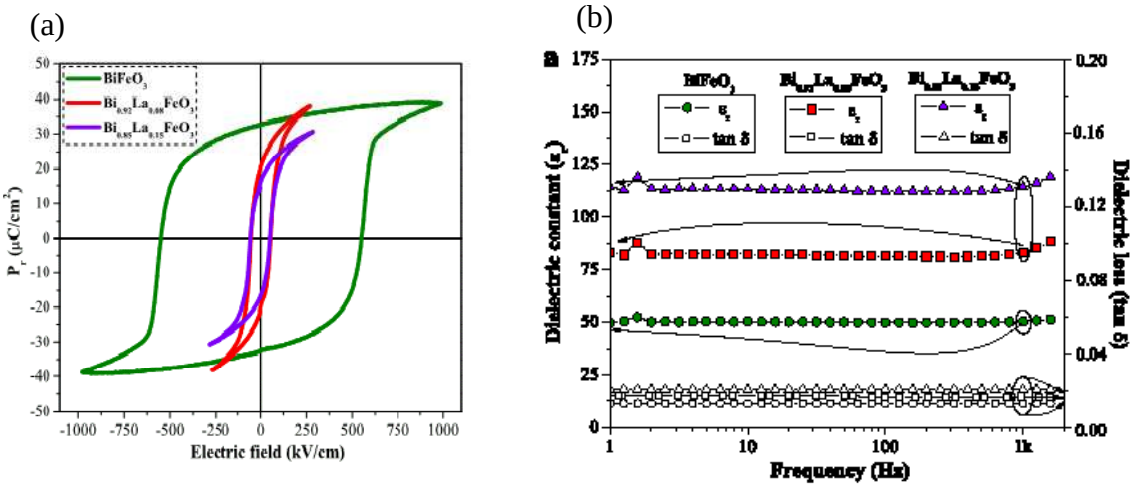

Figure 1.13. (a) P-E hysteresis loops and (b) dielectric constants as a function of frequency of La-substituted $BiFeO_3$ polycrystalline thin films using chemical solution deposition method. Figures adapted from A. Z. Simoes *et al.* [91]

Sushil K. Singh *et al.* have deposited 0%-20% La-doped $BiFeO_3$ thin films on Pt substrate and show continuously reduced remanant polarization and increased dielectric constants with increasing La content. No structural distortions or preferred orientations are observed though. [48] They also proposed that La might have no intrinsic effect on leakage based on the observation that the leakage current density of 5% La-doped thin film is higher in the low-electric field region than that of the pure $BiFeO_3$. But they showed reduced leakage current in higher La content of $BiFeO_3$ thin films. [48, 75] However, they managed to reduce the overall leakage current by co-doping La and Ni in $BiFeO_3$ thin film [47] Chia-Ching Lee *et al.* have reported that the leakage mechanism in La-doped $BiFeO_3$ thin film (Poole-Frenkel) deposited by chemical solution is different from that of pure $BiFeO_3$ (space-charge-limited conduction with deep traps) and La-doped $BiFeO_3$ thin film displayed smaller leakage current. Note that different thin film deposition methods may lead to different leakage mechanisms. [49] Similar to S. K. Singh *et al*., A. Z. Simoes *et al.* fabricated ~350nm $Bi_{1-x}La_xFeO_3$ (x=0.00, 0.08 and 0.15) polycrystalline thin films on Pt substrate by chemical solution deposition. Although they claimed no structural distortion and preferred orientation in their films, dramatic reduction in coercive field (from 550 kV/cm to 51 kV/cm) and remanent polarization (32.7 to 16.6 $\mu C/cm^2$) are observed upon La doping as shown in Figure 1.13 (a). Note that the remanant polarization of $BiFeO_3$ with rhombohedral structure reported here was much smaller than the widely accepted intrinsic value. The dielectric constant (Figure 1.13 (b)) and fatigue resistance improve with increasing La concentration. No effect on piezoelectric response is discussed. [57] In their earlier report on the influence of La doping in $BiFeO_3$ thin film, they could achieve d_{33} of 80 pm/V. But the doping concentration is not stated. [58] On

the contrary, V. R. Singh *et al.* prepared 0-30% of La-doped $BiFeO_3$ by the same deposition method on ITO coated glass substrate, and observed structural changes from rhombohedral to pseudocubic at 15% of La-substituted $BiFeO_3$. However, they couldn't obtain well-saturated P-E hysteresis loops. [82]

1.4 Purpose of Research

Lead-based ferro/piezoelectric materials, such as $Pb(Zr,Ti)O_3$, are widely used because of their excellent ferroelectric and piezoelectric properties at composition near the MPB. However, environmental concerns due to the toxicity associated with Pb and PbO have triggered intensive research activities looking for alternative lead-free ferro/piezoelectric systems. To obtain properties comparable to that of $Pb(Zr,Ti)O_3$, an MPB between different structures is necessary. Furthermore, applications in nanoscale devices require the materials to be in the form of films, which introduces mechanical constraint from substrates. It is desirable to study the process and properties of such material systems in thin films. In this project, we performed such investigations on two promising candidates: one is based on $(K,Na)NbO_3$, the other based on $BiFeO_3$.

1.4.1 $(K,Na)NbO_3$-based Ferro/piezoelectric System

Solid solution of $(K,Na)NbO_3$, $(K,Na)TaO_3$ and $LiTaO_3$ is one of the leading candidates, in which an MPB is found at the composition of $[(K_{0.5}Na_{0.5})_{0.97}Li_{0.03}](Nb_{0.8}Ta_{0.2})O_3$ (KNN-KNT-$L_{0.03}$T). The non-textured ceramic of this system exhibits a piezoelectric coefficient, d_{33} of 230 pm/V, and texturing the material leads to a d_{33} of 373 pm/V, which is comparable to that of the standard $Pb(Zr,Ti)O_3$. However, processing route leading to highly <001> textured polycrystal is complicated.

Ferroelectric films, like bulk materials, possess a set of properties that are attributed to their composition and microstructure. But, unlike the bulk, they also possess another set of properties derived from their proximity and interaction with the supporting substrate. Therefore, the physical properties of single crystals and polycrystalline ceramics can only be reproduced partially in thin films. The defects in

polycrystalline structure will lead to a degradation of ferroelectric properties, such as remanent polarization, piezoelectric coefficient, charge retention and time-dependent fatigue. Hence, epitaxial films usually possess superior properties over polycrystalline films.

For a complex system like the KNN-KNT-$L_{0.03}$T where no single crystal is available, epitaxial thin films also offers the opportunity to investigate its intrinsic properties along different crystallographic directions, which has not been studied. Thus, epitaxial thin films will be fabricated on single crystal $SrTiO_3$ substrates by using pulsed laser deposition. (001), (110) and (111)-cut substrates will be used to control the film orientation. Note that although the epitaxial thin films may have nearly single crystal quality, substrate clamping and film/substrate interface would affect their properties significantly. In summary, the purpose of this sub-project is to unravel the intrinsic properties of the (K,Na)NbO_3-based ferro/piezoelectric system and investigate its applicability in thin film applications. Investigation on the structure and electrical properties along different crystallographic directions will be carried out.

1.4.2 $BiFeO_3$-based Ferro/piezoelectric System

In many ways, $BiFeO_3$ is very similar to another prototypical ferroelectric material, $PbTiO_3$. They both possess large spontaneous polarizations induced by the stereochemical activity of the $6s^2$ lone pair of the Bi and Pb ions. So it is natural to think of using $BiFeO_3$ as a starting point to build a lead-free ferro/piezoelectric system with an MPB, just like the development of $Pb(Zr,Ti)O_3$ system. However, there are major differences between the two. $BiFeO_3$ has a rhombohedral structure and $PbTiO_3$ is tetragonal. In $BiFeO_3$, the large displacement of Bi^{3+} ions plays a major role in generating the structural distortion and spontaneous polarization. While in $PbTiO_3$, Ti^{4+} contributes significantly, more than Pb^{2+} in fact. These differences lead to the hypothesis that A-site doping in $BiFeO_3$ may be more effective in generating an MPB.

Other issues associated with $BiFeO_3$ include relatively high coercive field, leakage current, small dielectric constant and piezoelectric coefficient, all of which could be tuned by chemical substitution, theoretically. We follow the example of $Pb(Zr,Ti)O_3$, where Zr-substitution into B-site results in the formation of an MPB with superior properties. The reduction in coercive field, enhancement in susceptibilities and a decrease in remanant polarization are believed to be due to the softening of the unit cell and the multiple degenerated polar states at the MPB. Rare-earth substitutions at the Bi^{3+} site have been used to improve the properties of $BiFeO_3$. La^{3+}, which has almost the same ionic radius as Bi^{3+} (1.16 and 1.17 Å [92], respectively), is chosen as the substitute in this project. $LaFeO_3$ has an orthorhombic structure with lattice constants listed in Table 1.1. It is expected that La substitution at the A-site of $BiFeO_3$ will reduce the lattice distortion leading to a phase transition, and decrease the Curie temperature. Accompanying the changes in crystal structure, the electrical properties of $BiFeO_3$ could be manipulated too. Despite the large amount of

reports on this system, the results varied significantly from group to group. Indeed, the structural transition upon La substitution in $BiFeO_3$ is still an open question. We will conduct a systematic investigation and analyze the results using first principle calculations (in collaboration with Dr. Zhang Zhen, NTU).

In summary, we propose to investigate the effects of La substitution on the A-site of $BiFeO_3$ on its structure and electrical properties. The goal is to induce a phase transition, which may lead to decreased coercive field and improved dielectric constant and piezoelectric coefficient.

Table 1.1. Structure and properties of $BiFeO_3$ and $LaFeO_3$ in bulk form.

$BiFeO_3$	$LaFeO_3$
Rhombehedral	Orthorhombic
a=5.556 Å, c=13.867 Å	a=5.556 Å, b=5.565 Å, c=7.863 Å
Distorted Perovskite	Perovskite
Ferroelectric, Tc=850 °C	Not ferroelectric
Antiferromagnetic, TN=370 °C	Antiferromagnetic, TN=465 °C (weak G-type ferromagnetic)

1.4.3 Pulsed Laser Deposition

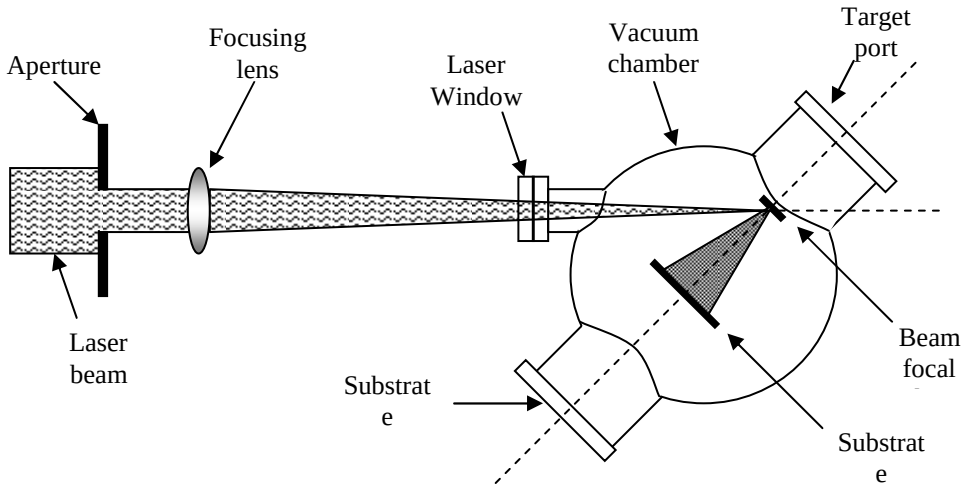

Figure 1.14. Schematic illustration of a Pulsed Laser Deposition system. Figure adapted from Wang *et al*. [93]

A schematic diagram of a basic pulsed laser deposition (PLD) system is shown in Figure 1.14. Both the target and substrate are placed in a vacuum chamber. A high energy pulsed laser beam (typically 25ns pulses with energy in the range of 0.1-1 J and frequency of 1-30Hz) is focused onto the target. Lasers that are commonly used include ArF, KrF excimer lasers, and Nd:YAG laser. [94] Because of the high laser energy, the target (bulk ceramic or crystal) material is evaporated instantaneously, forming a plasma plume. The plume is normal to the target surface and collected on a substrate that is heated to certain temperature. Important parameters that affect the quality of the films include substrate temperature, laser energy density and frequency, target-to-substrate distance, and deposition gas pressure, etc. During oxide deposition, oxygen must be introduced into the chamber to assist the formation of the desired phase and film composition.

Compared with other thin film deposition techniques, PLD has a number of advantages:

(i) Versatility. Almost any materials, including metals, oxides, semiconductors and even polymers, can be deposited by PLD. All that is required is a target of the desired composition. It is unlike Molecular Beam Epitaxy (MBE) and Chemical Vapor Deposition (CVD), where different sources of precursors are required for each element.

(ii) Relatively easy control of the film composition. Because of the very high energy of the laser pulse, all the elements in the target are evaporated instantly and fly towards the substrate. This makes optimization of the deposition process much easier.

(iii) The energy associated with the high ionic content in the plumes produced by laser ablation (typically of the order of 10% and rising with increasing laser power density) and the high particle velocities (of the order of 10^6 $cm.s^{-1}$) appear to aid crystal growth and lower the substrate temperature required for epitaxy.

(iv) The process is clean, low cost, and is capable of producing heterostructures simply by switching between different targets.

The disadvantages of PLD technique is related to the small cross sectional area and forward directing of the plume, which lead to the limited sample size and poor conformal step coverage. There is also an intrinsic “splashing” associated with laser ablation itself, which produces droplets or big particles of the target material on the substrate surface. From an industrial perspective, this is particularly serious as it will result in device failure.

1.5 Organization of Dissertation

The remainder of this dissertation consists of 3 chapters followed by list of references.

Chapter 2 focuses on the deposition and characterization of (K,Na)NbO_3-based films by pulsed laser deposition. The structural and electrical properties of (K,Na)NbO_3-based films grown on different crystallographic directions are investigated. The chapter is ended with a summary of the challenges encountered and suggestions for future investigations.

Chapter 3 covers our study on the effect of La substitution in $BiFeO_3$ epitaxial thin films. The films are deposited by pulsed laser deposition. Detailed optimization of the deposition conditions has been conducted to control the second phases and growth mode of the films. Results of structural, electrical and optical characterizations and our attempt to explain the structure-property relation are then reported. This chapter also details the first principles calculation work conducted by our collaborator, Dr. Zhang Zheng, to explain the experiment observations.

Chapter 4 summarizes the important findings of this project and suggests possible directions for future investigation.

CHAPTER 2

Deposition and Characterization of $(K,Na)NbO_3$-based Ferro/piezoelectric System

To investigate the intrinsic properties of $(K,Na)NbO_3$-based lead-free ferro/piezoelectric system at the MPB composition, epitaxial KNN-KNT-$L_{0.03}$T films are deposited on (001), (110) and (111)-cut single crystal $SrTiO_3$ substrates by pulsed laser deposition. The crystal structure is characterized using X-ray diffractometer (XRD). The dielectric, piezoelectric and ferroelectric properties are studied and correlated with the structure of the samples.

2.1 Pulsed Laser Deposition of KNN-KNT-$L_{0.03}$T Films

The KNN-KNT-$L_{0.03}$T films are prepared by PLD according to the following steps:

(i) Substrate cleaning and target preparation

The epitaxial films are deposited on one side polished (100), (110) and (111)-cut $SrTiO_3$ substrates. To remove the organic and inorganic residuals on the surface left from the polishing process, the substrate is cleaned thoroughly with acetone and ethanol in ultrasonic bath for 15 minutes each. The commercially available 99.9% $SrRuO_3$ target is used to prepare the bottom electrode whereas the dense KNN-KNT-

$L_{0.03}T$ ceramic target is synthesized using conventional solid state reaction. The targets are 0.25 inch in thickness and 1 inch in diameter.

(ii) Setting up and pre-pump the chamber

Once the substrate and the target are ready, they are put into the deposition chamber, which will then be pumped to a base pressure of about 5.0×10^{-4} Pa.

(iii) Deposition conditions

The oxygen flow rate is adjusted to maintain a dynamic oxygen partial pressure. The substrate is heated to a desired temperature at 20 ºC/min. KrF excimer laser with 248nm wavelength and pulsed duration of 25ns is used. The laser energy and repetition rate are adjusted to the desired values. Details of the deposition parameters are listed in Table 1.

(iv) Post-deposition conditions

After the deposition, oxygen is introduced into the chamber until near ambient pressure (7.0×10^4 Pa) while the substrate is kept at the deposition temperature. It is then cooled down slowly to room temperature at 5 ºC/min to prevent cracking, which could be produced due to the different thermal expansion coefficients of the film and the substrate.

Table 2.2. Optimized deposition parameters.

Film	Substrate temperature	O_2 partial pressure	Energy density	Laser repetition rate
$SrRuO_3$	750 ºC	100 mTorr	1 J/cm^2	3 Hz
KNN-KNT-$L_{0.03}T$	725 ºC	20 mTorr	1 J/cm^2	10 Hz

2.2 Properties of the KNN-KNT-$L_{0.03}$T Films

The thickness of the KNN-KNT-$L_{0.03}$T and SRO layers are 1.5 µm and 20 nm, respectively. The phase purity and structures of the $(001)_{pc}$, $(110)_{pc}$ and $(111)_{pc}$ oriented films are characterized by x-ray diffraction (PANalytical X'pert PRO MRD). The dielectric, piezoelectric and ferroelectric properties are studied using LCR meter (Agilent, E4980A), piezoelectric force microscopy (Asylum Research, MFP-3D-SA) and ferroelectric tester (Radiant Technologies, Precision LC), respectively after the deposition of Pt top electrodes. The Pt is sputtered following standard photolithography process and has an area of 2500 μm^2. For the local piezoelectric hysteresis studies, Pt-coated Si tip with force constant of ~42 N/m and resonance frequency of ~320 kHz is used.

2.2.1 Structural Analysis

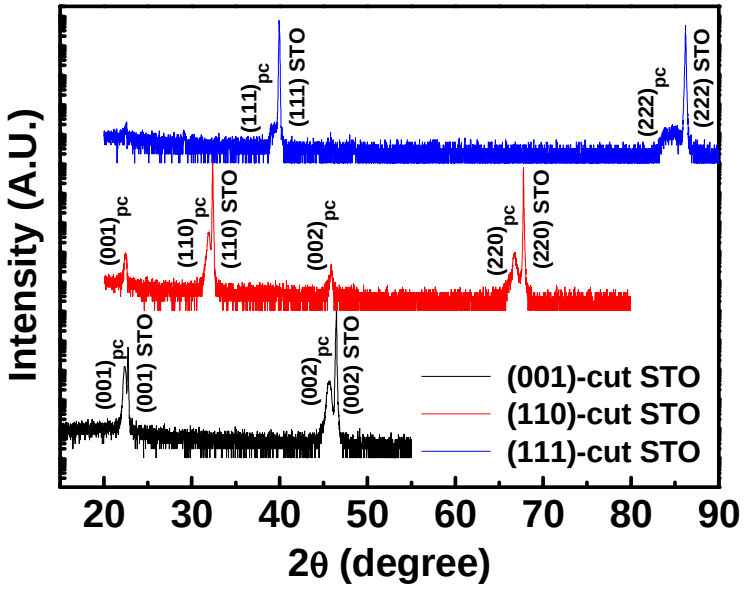

Figure 2.1. XRD θ-2θ scans of $(001)_{pc}$, $(110)_{pc}$ and $(111)_{pc}$ oriented $(K,Na)NbO_3$-based films.

Typical X-ray diffraction (XRD) θ-2θ scans of the KNN-KNT-$L_{0.03}$T films are shown in Figure 2.1. Only $(001)_{pc}$ and $(111)_{pc}$ type diffraction peaks are observed for

films grown on $(001)_{pc}$ and $(111)_{pc}$ oriented $SrTiO_3$ substrates, respectively, in addition to the peaks from the substrate. The $SrRuO_3$ peaks overlap with that of the KNN-KNT-$L_{0.03}$T films. No second phase is observed. However, small $(00l)_{pc}$ peaks are observed for the films grown on (110) oriented substrates. The MPB is reported to occur between orthorhombic and tetragonal phases in bulk system. The as-deposited films with cubic structure could transform into orthorhombic and/or tetragonal phases at the Curie temperature of 323ºC when cooling down from the deposition temperature of 725ºC. However, no domain structures are observed in the films by using piezoforce microscopy.

2.2.2 Electrical Properties of the KNN-KNT-$L_{0.03}$T Films

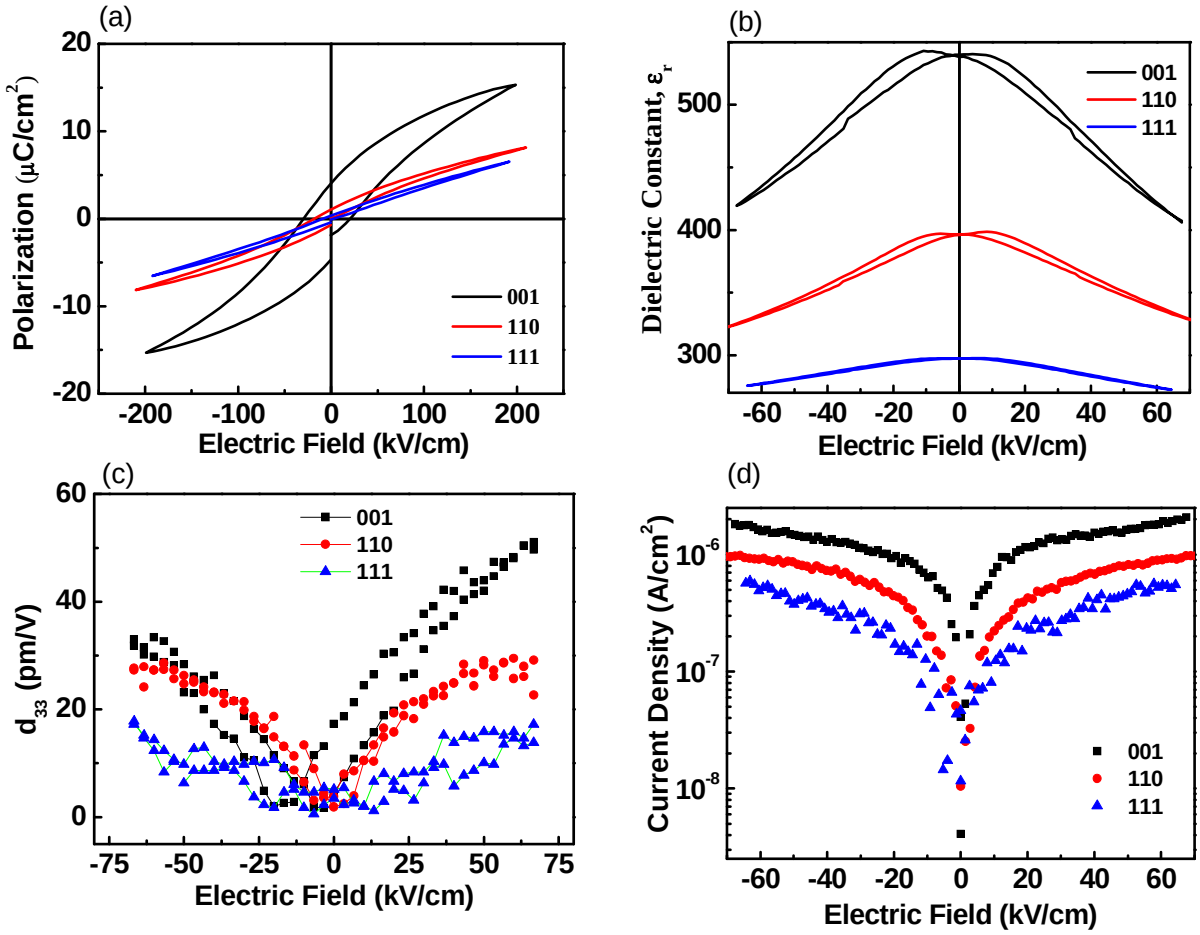

Figure 2.2. (a) P-E hysteresis loops, (b) ε_r-E hysteresis loops, (c) d_{33}-E hysteresis loops, and (d) current density of KNN-KNT-$L_{0.03}$T films grown on (110), (001) and (111) oriented STO substrates.

The P-E hysteresis loops along the three orientations are determined using a ferroelectric tester (Radiant Technology precision) at 1kHz. The results are shown in Figure 2.2 (a) for all three samples. The coercive fields (E_c) are 30 kV/cm, 18 kV/cm and 8 kV/cm and the remanent polarizations (P_rs) are 4, 1 and 0.3 μC/cm^2 for $(001)_{pc}$, $(110)_{pc}$ and $(111)_{pc}$ films, respectively. Comparing with the synthesized ceramic target, whose P_r and E_c are ~18 μC/cm^2 and 8.60kV/cm, the thin films show much smaller P_r and larger E_c. Furthermore, the P_r along $(110)_{pc}$ and $(111)_{pc}$ directions do not correspond to the projections from polarization along $(001)_{pc}$ direction, suggesting that

the films grown on different substrates may have different structures. Thus the spontaneous polarizations lie along different crystallographic directions.

To gain more insight into the properties of the KNN-KNT-$L_{0.03}$T films, we have also performed small signal dielectric and piezoelectric coefficient measurements. The variation of dielectric constant (ε_r) as a function of DC bias is measured by applying a small AC voltage of 200 mV (peak to peak) at 100 kHz. The very small AC voltage is used for the measurements so that the AC field does not alter the polarization state and minimizes the domain wall contribution. This could allow the comparison of the film with the bulk material. Figure 2.2 (b) shows the butterfly-type ε_r-E hysteresis loops with two maxima due to the ferroelectric polarization reversal. However, the peaks merge together for the $(111)_{pc}$ oriented film, consistent with the slim P-E hysteresis loop. The zero-field ε_r are 540, 390 and 300 for the $(001)_{pc}$, $(110)_{pc}$ and $(111)_{pc}$ oriented films, respectively. These values are smaller than that of the bulk ceramic (~1256).

The out-of-plane piezoelectric hysteresis loops (d_{33}-E) of KNN-KNT-$L_{0.03}$T films are shown in Figure 2.2 (c). The quantitative results is obtained by calibrating the PFM response using a sample with known d_{33} (X-cut quartz in this case, d_{11}=2.3 pm/V). The d_{33} of films are then calculated using $d_{33film} = (A/A_0)d_{11quartz}$, where A is the lock-in amplifier reading divided by the AC voltage used to excite sample vibration and A_0 is the corresponding value for quartz. This method has been used by other research groups and proven to be reliable. For details of the technique, please refer to appendix A. The d_{33}-E loops are consistent with the P-E hysteresis loops, where no distinct remanent d_{33} is observed for the $(110)_{pc}$ and $(111)_{pc}$ -oriented films. In perovskite ferroelectric systems, susceptibilities are usually larger along directions different from the spontaneous polarization direction. However, in this case, both ε_r

and d_{33} are the largest along $(001)_{pc}$ oriented film, which shows the largest The observed values are much smaller than that of the ceramics.

In ferroelectric ceramic, the dielectric and piezoelectric responses consist of intrinsic (averaged crystallographic response of the single domains) and extrinsic (motion of the domain walls and phase boundaries) components. The domain walls can be moved by electric field, stress, or combination of the two. The extrinsic contributions can be up to ~75% of the dielectric and piezoelectric responses observed.[95] However, due to the clamping effect of substrate and residual stresses in thin films, the mobility of domain wall and phase boundary would be different from that in bulk form. Relatively low leakage current is observed in our samples as shown in Figure 2.2 (d). Hence, the defect contributions to the polarization and dielectric constant should be small. The rather small susceptibilities of the epitaxial films suggest that the large piezoelectric response observed in bulk is likely due to the polymorphic phase transition, which consists of substantial extrinsic contribution from the 18-fold domain variants (12 variants from orthorhombic and 6 from tetragonal phases). In epitaxial thin films with less domain variants and the effect of substrate constraint, the extrinsic contribution will be less. Of course, effect of variation in the thin film composition cannot be excluded at the moment.

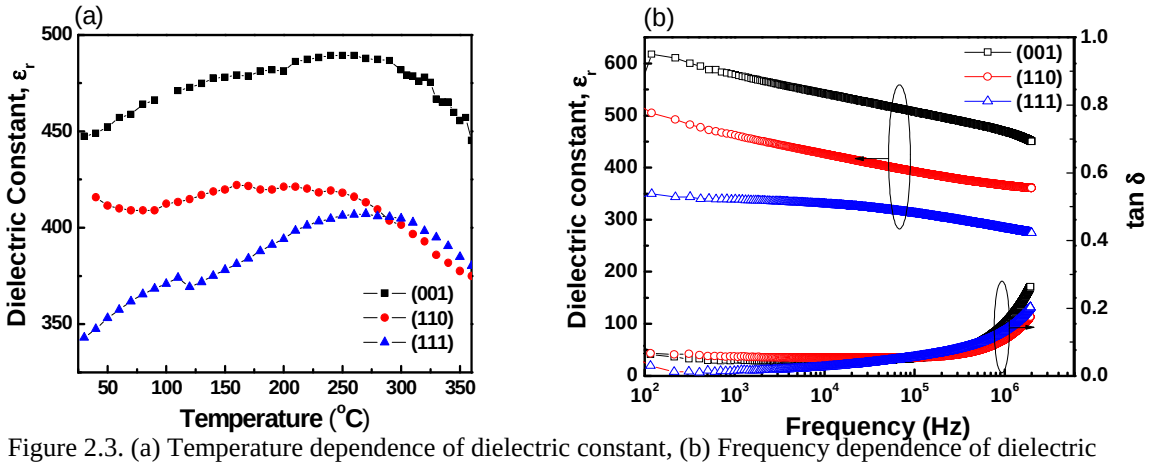

Figure 2.3. (a) Temperature dependence of dielectric constant, (b) Frequency dependence of dielectric constant and loss tangent for the KNN-KNT-$L_{0.03}$T films grown on (110), (001) and (111) oriented $SrTiO_3$ substrates.

We have also studied the dielectric constants of the epitaxial films (measured with AC voltage of 100mV at 100 kHz) at temperatures ranging from 25°C to 360°C. The results are shown in Figure 2.3 (a). From the literature, two dielectric anomalies were observed in the KNN-KNT-$L_{0.03}$T ceramics. The Curie temperature, at which the dielectric constant attains its maximum value, occurs at 323°C, while the other at ~70°C, corresponding to the phase transition of orthorhombic-tetragonal. The orthorhombic-tetragonal transition is a good indicator for the presence of MPB. However, for the KNN-KNT-$L_{0.03}$T films, only the paraelectric-ferroelectric transition temperatures are observed and the peaks are broadened. The Curie temperatures are ~260°C, 220°C and 270°C for $(001)_{pc}$, $(110)_{pc}$ and $(111)_{pc}$ -oriented films, respectively. These values are lower than that of the bulk. The difference could be due to composition variation of the films or the effect of the substrate. The fact that we did not observe the orthorhombic-tetragonal transition is consistent with the small susceptibilities of the films.

Figure 2.3 (b) shows the frequency dependence of dielectric constant and dielectric loss of the KNN-KNT-$L_{0.03}$T films along different crystallographic directions at room temperature. The relative values of the dielectric constant along $(001)_{pc}$, $(110)_{pc}$ and $(111)_{pc}$ -oriented films is consistent with the ε_r-E hysteresis loops. Frequency dispersion in dielectric constant increases from $(001)_{pc}$, $(110)_{pc}$ to $(111)_{pc}$ -oriented films. However, it is believed that space charge contribution is insignificant. The dielectric loss is quite constant up to 1MHz in all directions. At lower frequency, the dielectric loss of $(110)_{pc}$ -oriented film was higher than $(001)_{pc}$ -oriented film.

2.3 Summary

The epitaxial films of KNN-KNT-$L_{0.03}$T are deposited by PLD using single crystal $SrTiO_3$ as substrate. We are able to study the intrinsic properties of this system along different crystallographic directions. It is suggested that the superior properties of textured bulk ceramics are mainly due to extrinsic contributions.

The challenge of fabricating KNN-KNT-$L_{0.03}$T films is associated with the fact that alkaline elements are volatile. It is very difficult to control the film composition precisely. Furthermore, it is not possible to confirm the film composition accurately with current technologies. For a complex system such as KNN-KNT-$L_{0.03}$T, its properties would certainly be affected by variation in composition resulting from the high temperature growth process. Therefore, the structure of KNN-KNT-$L_{0.03}$T is not further investigated and it's desirable to have a simpler lead-free system which is easier to process and study. This has brought us to investigate the $BiFeO_3$-based system.

CHAPTER 3

Deposition and Characterization of $(Bi,La)FeO_3$ Thin Films

The second system that we have investigated is the solid solution of $BiFeO_3$ and $LaFeO_3$, $Bi_{(1-x)}La_xFeO_3$. We moved onto this system because it is much less complicated than KNN-KNT-$L_{0.03}$T in both the structure evolution and composition. Because of the large polarization of $BiFeO_3$, it is natural to think of creating a high performance lead-free ferro/piezoelectric system using it as one end member. However, to our knowledge, (Bi, Sm)FeO_3 is the first and the only found system that posses an MPB.[96] Incorporation of La at the A-site has been proven to be effective in improving properties of $BiFeO_3$. However, literature reports vary from group to group and a systematic investigation of the structure, electrical and optical properties of $BiFeO_3$ as a function of La concentration is necessary. We thus fabricate epitaxial La-substituted $BiFeO_3$ thin films on (001)-cut single crystal $SrTiO_3$ substrates by PLD. Deposition conditions are first optimized to control the impurity phases and domain structures of $BiFeO_3$ thin films. $Bi_{(1-x)}La_xFeO_3$ thin films are then deposited under optimized condition. The electrical and optical properties of $Bi_{(1-x)}La_xFeO_3$ epitaxial thin films with x ranging from 0 to 0.20 are characterized and correlated with their structures. First principles calculations are performed, in collaboration with Dr. Zhang Zhen, to understand the experimental observations. This chapter ends with a model that we propose to explain the observations.

3.1 Optimization of Thin Film Deposition Conditions

To conduct a meaningful study on the properties of $Bi_{(1-x)}La_xFeO_3$ as a function of La concentration, it is important to firstly obtain the optimal deposition conditions of pure $BiFeO_3$. Second phases and/or structural imperfections may lead to misjudgment in the analysis. Despite the intensive research conducted on $BiFeO_3$ during the last decade, it is widely recognized that the deposition window of phase pure $BiFeO_3$ is small and it is challenging to control the film structure and composition. The difficulty is likely due to the volatility of Bi.

3.1.1 Controlling the Thin Film Growth Mode

To obtain high quality defect free epitaxial thin films, it is necessary to control the growth mode. Island growth leads to rough surface and more defects. Layer by layer growth is preferred. During the first stage of the project, epitaxial $BiFeO_3$ thin films are grown on (001)-cut single crystal $SrTiO_3$ substrate by PLD. Stoichiometric $BiFeO_3$ target is ablated by using KrF excimer laser (λ=248nm) with an energy density of 1 J/cm^2 and a repetition rate of 5 Hz. The $BiFeO_3$ target is pre-ablated prior the deposition to remove any surface contaminations. The dynamic oxygen partial pressure is fixed at 100 mTorr during the deposition, while the deposition temperature is varied between 600 and 750 ºC. After deposition, oxygen is introduced into the chamber until near ambient pressure (7.0×10^4 Pa) while the substrate remains at its deposition temperature. The substrate is then cooled down slowly to room temperature at 5 ºC/min. To achieve a uniform temperature distribution across the substrate and a better thermal conductivity between the heater and the substrate, silver paste is used to fix the substrate on the holder. All films have a thickness of around 50nm (1 hour deposition) as determined using a step profiler.

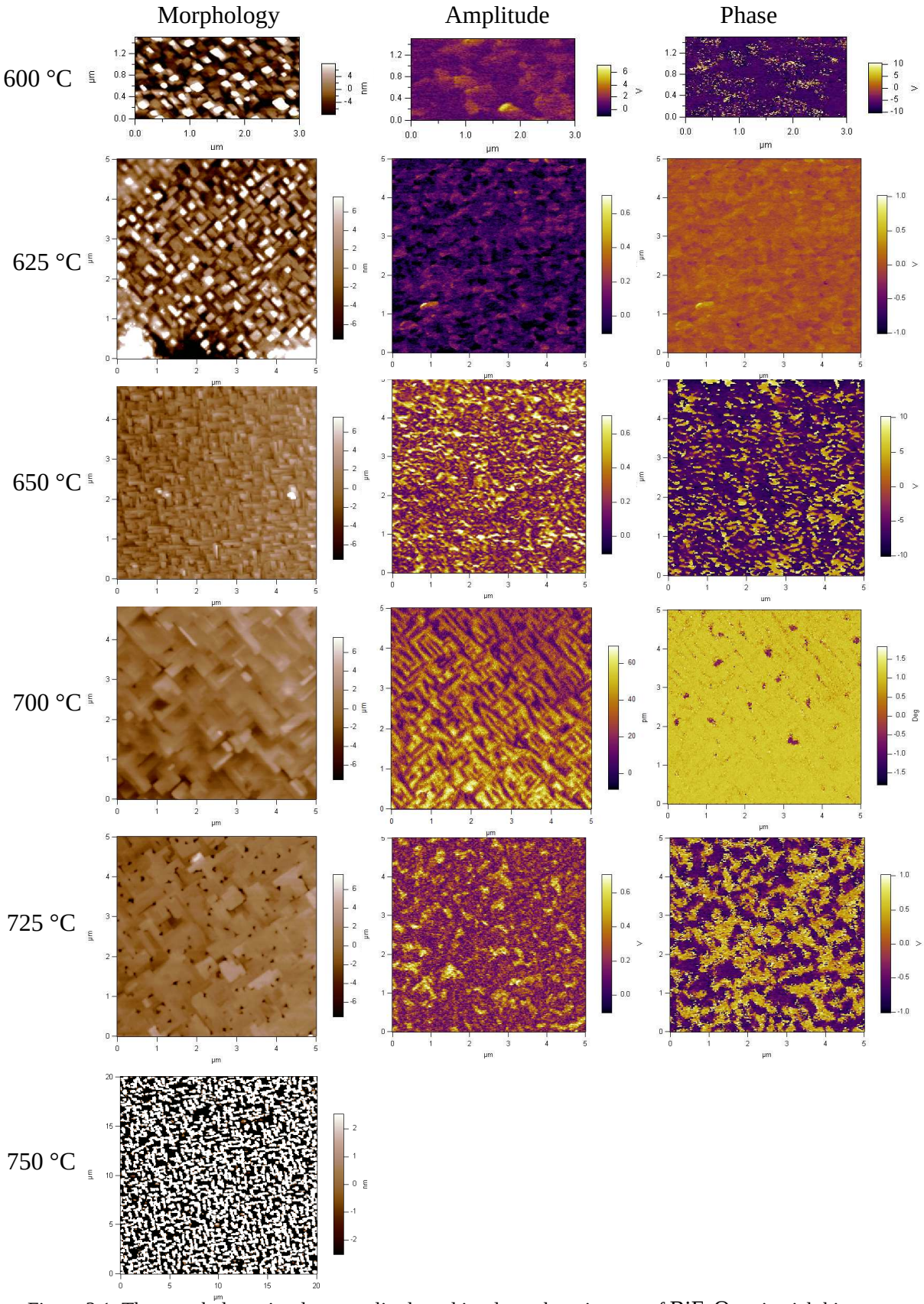

Figure 3.1. The morphology, in-plane amplitude and in-plane phase images of $BiFeO_3$ epitaxial thin films grown at 100 mTorr with different deposition temperatures.

The morphology and ferroelectric domain images of $BiFeO_3$ thin films grown at different temperatures (Figure 3.1) are investigated using atomic force microscopy (AFM, Asylum Research MFP-3D). By using an external lock-in amplifier, we can study the in-plane (IP) and out-of-plane (OP) domain structures of the as grown films. We use highly doped Si tips with Pt/Ir-coated (spring constant of 42 N/m, resonance frequency of 320 kHz and tip radius of 25 nm) for such measurements. The domain images were obtained at ambient condition by applying 10 kHz, 2V AC (peak-to-peak) voltage applied to the sample. For details of the technique, please refer to Appendix A. Looking at Figure 3.1, the most striking feature is the dramatic differences in the IP domain structures of the films grown at different temperatures. Most of the samples show random IP domain structures, while regular domain pattern was observed for film deposited at 700 ºC. The IP PFM images were taken with the cantilever scanning along the <110>c direction of the film. Two orthogonal sets of domains were observed. The three contrasts (purple, orange and yellow) seen in the IP amplitude PFM image indicates that the domains contain four polarization variants, this is schematically demonstrated in Figure 3.2. [97] The result indicates that the deposition temperature is important in controlling the domain structure of $BiFeO_3$.

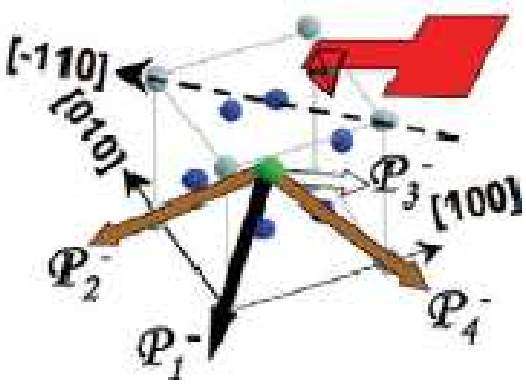

Figure 3.2. Schematics of polarization directions in (001)-oriented $BiFeO_3$ thin film. Figure adapted from Chu Y. H. *et al*. [97]

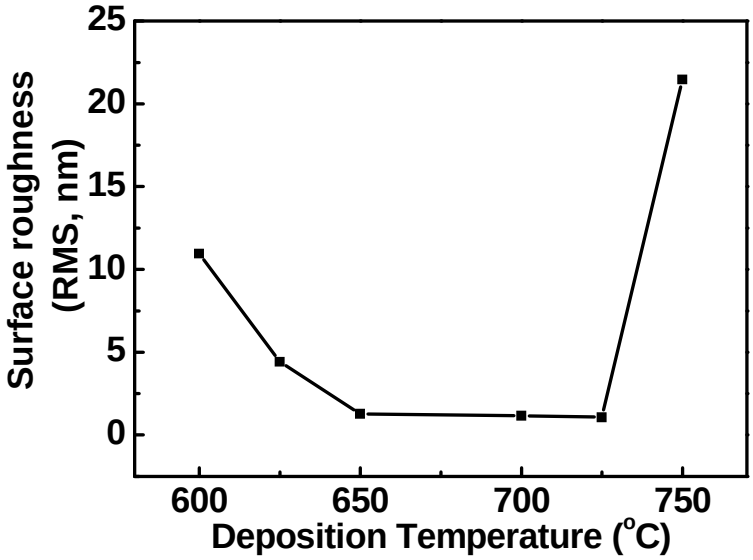

Figure 3.3. Surface roughness (RMS in nm) of $BiFeO_3$ epitaxial thin films as a function of deposition temperatures measured using atomic force microscopy. (All based on 5 μ m x 5 μ m scan size except the film grown at 600°C with scan size of 3 μ m x 1.5 μ m)

Comparing the morphology images of $BiFeO_3$ films grown at different temperatures, it is interesting to note that the domain patterns are related to the surface morphology and roughness. The surface roughness (obtained from a 5 μm x 5 μm area for all samples except 3 μm x 1.5 μm for 600 °C sample) decreases from 10.954 nm for sample grown at 600 °C to 1.067 nm for that grown at 725 °C, as shown in Figure 3.3. It is suggested that at low temperature, island growth is dominating due to the relatively low thermal energy of adatoms on the substrate. Island growth mode leads to relatively rough surface and more defects at the substrate/film interface. As temperature increases, higher thermal energy leads to longer diffusion length of the adatoms and layer by layer growth of the film. A more coherent interface can be achieved. The crisscross pattern is believed to be due to the small miscut angle of the substrate. Step flow growth of the film has been reported on single unit cell step TiO_2-terminated STO substrate.[98] Furthermore, cubes with diameters of 20-60 nm

protruding out of the film surface are observed for samples grown at 625 °C or lower. Similar features have been reported previously and are attributed to the nucleation of square-shaped bismuth oxide that outgrowths on the film surface. [99] At low temperature, excess bismuth cannot be re-evaporated when it reaches the substrate because of insufficient thermal energy, and thus, form bismuth oxide. For films grown at 750^{o}C, very rough surface is observed. It should be due to Bi-deficient in the film.

The above analysis is confirmed by XRD characterizations, as shown in Figure 3.4. The growth window of phase pure $BiFeO_3$ thin film is relatively small. Typical impurities i.e. Bi_2O_3, bismuth-rich oxide or Fe_2O_3 are easily formed. Bi_2O_3 or bismuth-rich oxide, which results in higher leakage in $BiFeO_3$ film are commonly observed in films deposited at higher oxygen pressure and lower temperature when excessive bismuth re-evaporation is limited. On the other hand, Fe_2O_3 is usually seen in films deposited under the opposite conditions.[99, 100]

To correlate the surface morphology and domain structure with the phase purity and crystallinity of $BiFeO_3$ deposited at various temperatures, XRD patterns are obtained and the out-of-plane lattice parameters are calculated. Figure 3.4 shows the θ-2θ scans obtained by using two systems, (a) the high intensity Shimadzu system and the high resolution PANalytical X'pert PRO MRD system. The high intensity of the Shimadzu system leads to a better capability in impurities detection. Second phase that can be attributed to $Bi_2O_3$are observed for all $BiFeO_3$ films except the one grown at 750 °C. However, the large surface roughness of this sample is undesirable. The out-of-plane lattice parameter increases from 4.05 Å to 4.07 Å when the deposition temperature increases from 600 °C to 650 °C (Figure 3.2 (c)), and remains unchanged up to 725 °C. This is consistent with the previous analysis that higher temperature enables layer by layer growth and a more coherent substrate/film interface. Since

$SrTiO_3$ has a smaller lattice constant than $BiFeO_3$, coherent interface leads to larger out-of-plane lattice constant. FWHM values obtained from rocking curves using high resolution XRD system shows consistent trend, which decreases from ~0.13 to about 0.10 as deposition temperatures increases. Small FWHM value indicates better crystallinity. The out-of-plane lattice parameter drops suddenly to 4.02 Å for films grown at 750^{o}C even though no impurity phases are observed. This could be due to a change in composition. The evaporation of Bi from the perovskite unit cell may lead to a decrease in the cell volume.

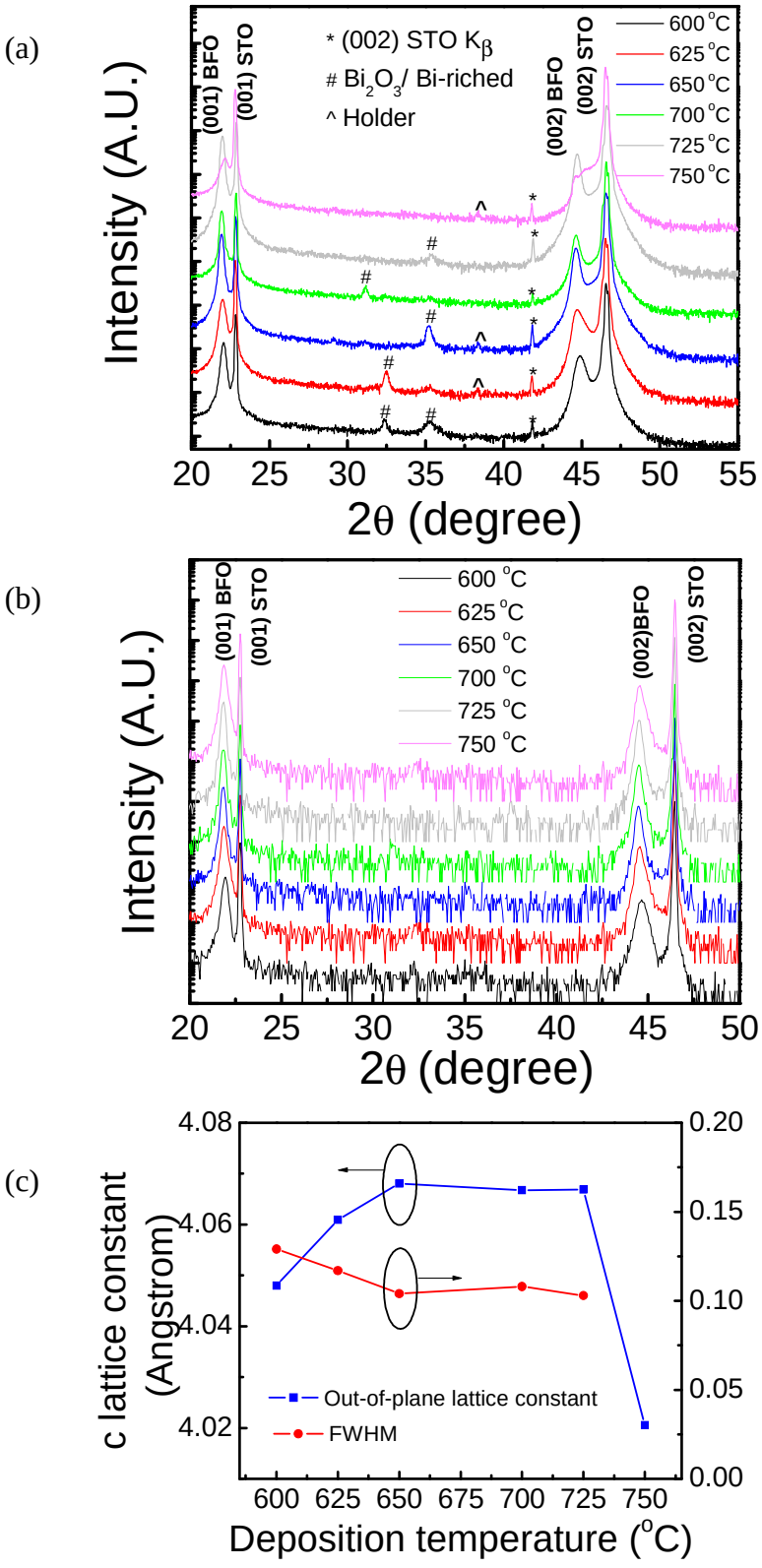

Figure 3.4 (a) XRD (Shimadzu), (b) high resolution XRD (PANalytical X'pert PRO MRD) θ-2θ scans and (c) the corresponding FWHM and out-of-plane lattice parameters of $BiFeO_3$ thin films grown at 100 mTorr with different deposition temperatures.

It is concluded that for an oxygen partial pressure of 100mTorr, the optimal deposition temperature is within the range of 650 °C to 725 °C. From controlling the ferroelectric domain point of view, the best deposition temperature is 700 °C. However, these films still contain Bi_2O_3 and/or Bi-rich second phases. Further optimization of the deposition condition is necessary. It has been reported that a phase pure $BiFeO_3$ could be achieved through controlling the deposition temperature. [101] We have observed similar trend in our experiment, but excess Bi still exist even at the highest desirable deposition temperature. We thus set off to tune other parameters, including oxygen partial pressure and deposition rate, to achieve the best thin film.

3.1.2 Controlling the Second Phase

Oxygen partial pressure is another factor that will affect the bismuth content in $BiFeO_3$ thin films deposited by PLD. Lower pressure leads to less bismuth in the film due to the easiness of the excessive bismuth evaporating from the heated substrate. Thus, we maintain the deposition temperature to be at 700^oC and lower the partial oxygen pressures to 80 and 50 mTorr. The laser repetition rate was kept unchanged.

The XRD patterns of $BiFeO_3$ grown on (001)-oriented STO substrate at 80 and 50 mTorr are shown in Figure 3.5. The results indicate that the films consist of epitaxial perovskite phase with no impurities. This is consistent with our expectation. Comparing the morphology of $BiFeO_3$ films grown at 80 and 50 mTorr with the one at 100 mTorr, the growth mode is changed, likely due to the increased growth rate at lower partial oxygen pressure. Note that even though impurities-free $BiFeO_3$ thin films can be obtained within certain oxygen pressure range, the properties may be affected significantly when the oxygen pressure is too low. You *et al.* discovered that the dielectric constant (ε_r), remanant polarization (P_r) and piezoelectric coefficient (d_{33})

were reduced upon decreasing oxygen pressure and attributed that to the decreasing Bi:Fe ratio. [100] This is consistent with the fact that displacement of Bi^{3+} is the main contribution to the ferroelectric response of $BiFeO_3$. Lower oxygen pressure leads to more Bi vacancies and deteriorated properties. Thus, 80 mTorr was determined to be the optimal value without generating second phases. Note that the regular domain structure could not be retained under this deposition condition due to the change in growth mode at higher growth rate.

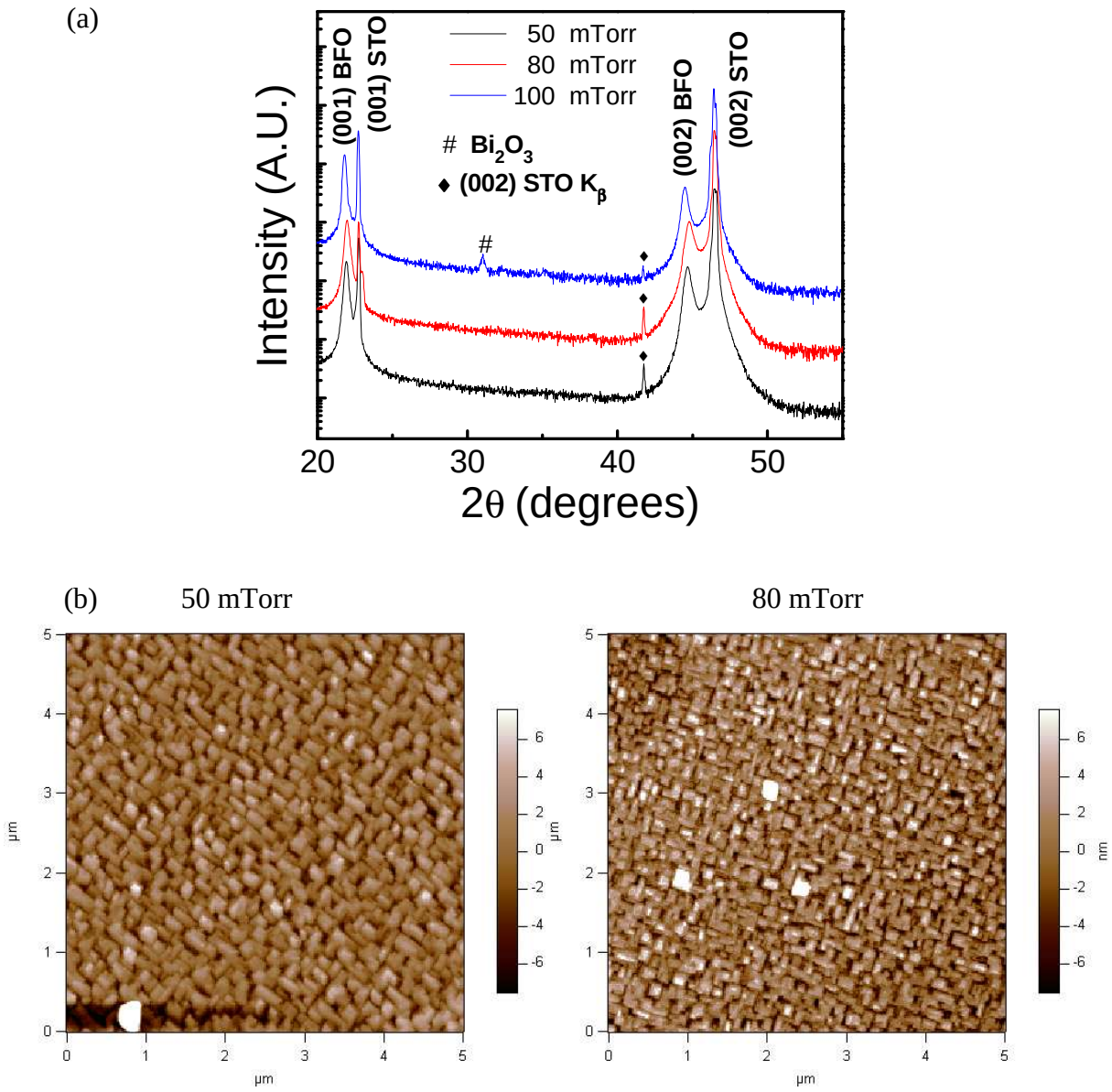

Figure 3.5 (a) XRD (Shimadzu) θ-2θ scans of $BiFeO_3$ thin films grown at 700 ºC under repetition of 5 Hz with different oxygen pressures of 50, 80 and 100 mTorr and (b) the corresponding morphology images.

(a) Repetition rate 10 Hz

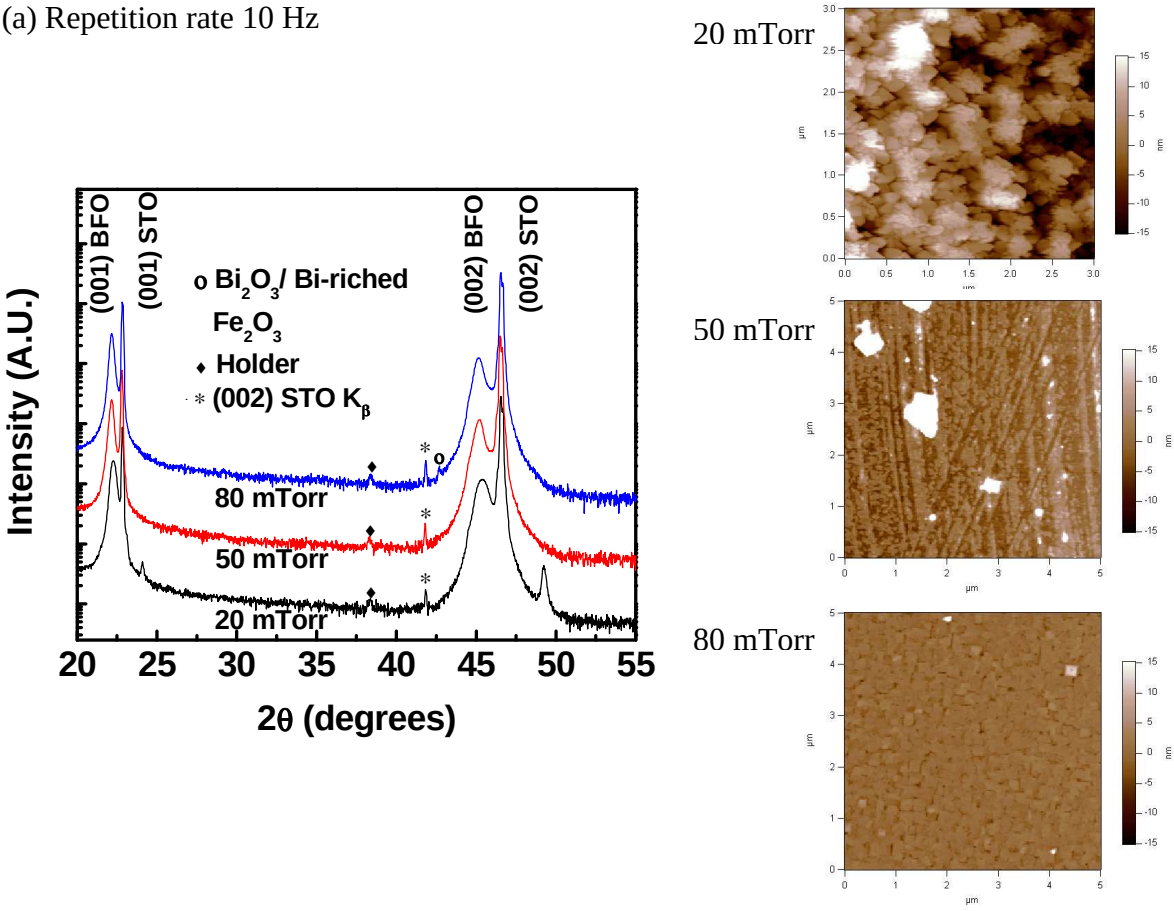

(b) Repetition rate 20 Hz

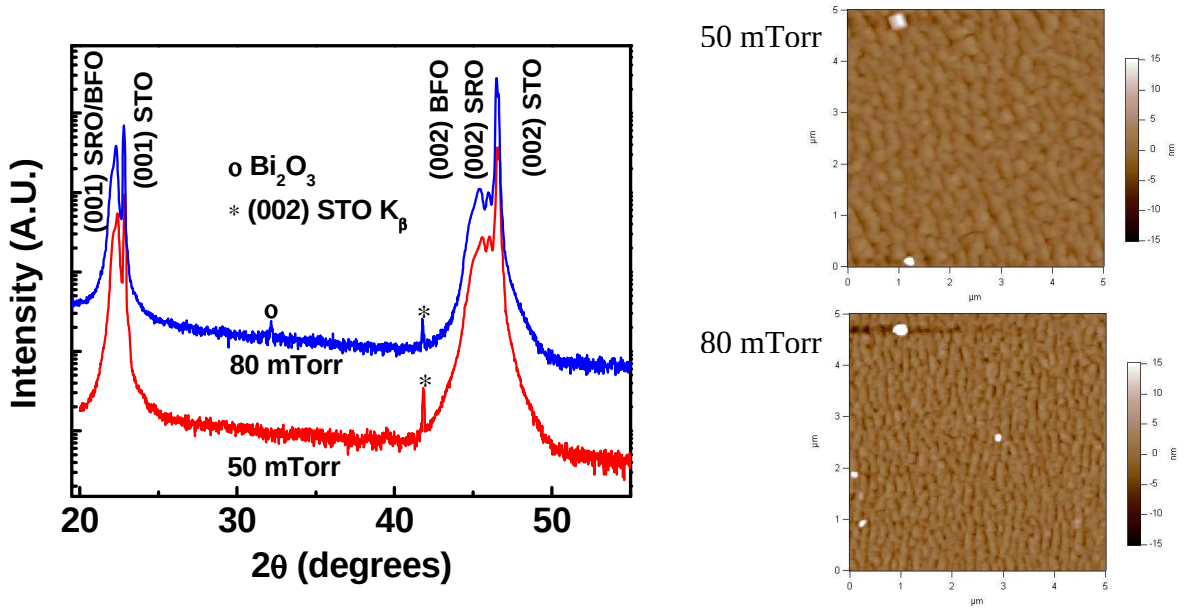

Figure 3.6 XRD (Shimadzu) θ-2θ scans of $BiFeO_3$ thin films grown at repetition rate of (a) 10 Hz and 20 Hz under different oxygen pressures and the corresponding morphology images.

To complete the deposition condition optimization, we have also studied the effect of growth rate by varying laser repetition frequency. Figure 3.6 (a) shows the XRD (Shimadzu) θ-2θ scans of $BiFeO_3$ thin films grown at 700 ºC under different oxygen pressures of 20, 50 and 80 mTorr with a laser repetition rate of 10Hz. Films deposited under 80mTorr oxygen pressure display relatively smoother morphology with the least big particles. Films grown under 20mTorr oxygen pressure show trace of Fe_2O_3 impurity. For laser repetition rate of 20Hz, impurity was observed for the samples deposited at 80mTorr oxygen pressure. Although no impurities were observed for films grown under 50 mTorr pressure, the growth mode has clearly become island growth.

The effects of different deposition parameters are summarized in Figure 3.7 (a) and (b). Deposition window of phase pure $BiFeO_3$ thin film is identified. However, we notice that it is not possible to achieve films with regular ferroelectric domain and single phase at the same time. We can choose a specific set of parameters for different experimental purpose. For example, relative thick samples (usually 100nm or above) are needed to conduct electrical characterization, we choose 700^{o}C, 80 mTorr and 5 Hz. To investigate effects of substrate and/or substitute on the ferroelectric domain structures, we can choose 700 ^{o}C, 100 mTorr and 5 Hz if regular domain structure is desired. Small amount of second phase does not affect domain analysis.

(a)

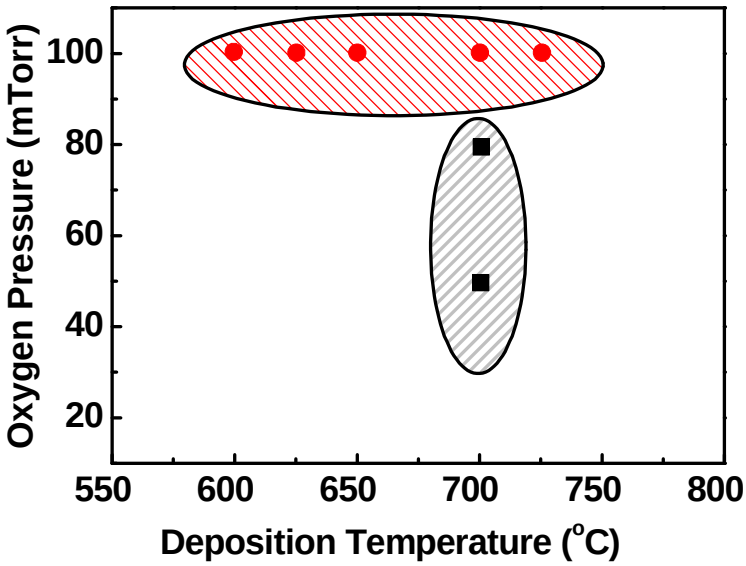

(b)

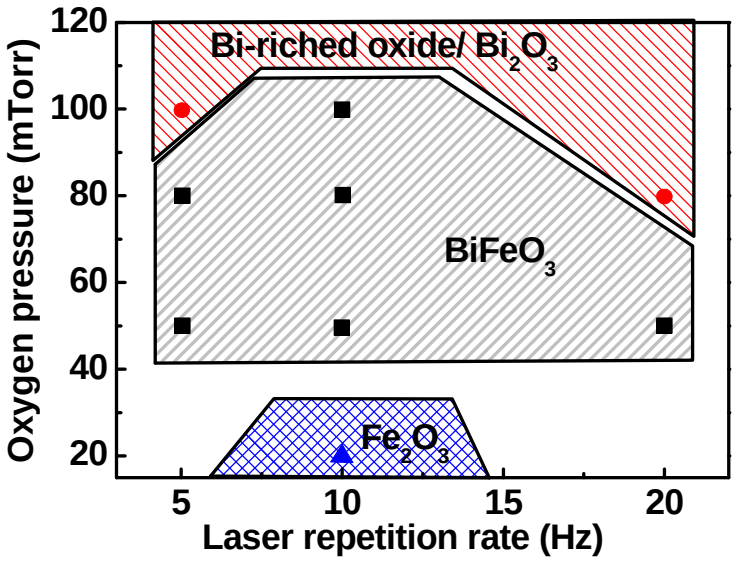

Figure 3.7. Schematics illustrating the phase diagrams of $BiFeO_3$ epitaxial thin films (a) Grown at fixed repetition rate at 5 Hz while varying oxygen pressures and deposition temperatures and (b) Grown at fixed temperature at 700 ^{o}C while varying oxygen pressures and laser repetition rates.

3.2 Growth and Structure of $Bi_{(1-x)}La_xFeO_3$ Thin Films

$Bi_{(1-x)}La_xFeO_3$ (x=0, 0.05, 0.10, 0.15 and 0.20) films are grown epitaxially on (001)-cut $SrTiO_3$ single crystal substrates using the optimal deposition condition as described in the previous section. For electrical characterizations, $SrRuO_3$ is deposited in-situ before the deposition of $Bi_{(1-x)}La_xFeO_3$. To track the changes of crystal structures as a function of La contents more accurately, $Bi_{(1-x)}La_xFeO_3$ epitaxial thin films are also grown on bare (001)-cut $SrTiO_3$ single substrates concurrently. Details of the deposition parameters are summarized in Table 3.1. The Pt top electrodes for electrical measurement are prepared following the standard photolithography technique and have areas of ~1600 μm^2. The phase purity, crystallanity and distorted rhombohedral angle of the $Bi_{(1-x)}La_xFeO_3$ epitaxial thin films are characterized by using high resolution X-ray diffraction (PANalytical X'pert PRO MRD).

Table 3.1. Deposition parameters.

Conditions \ Films	$SrRuO_3$	$Bi_{(1-x)}La_xFeO_3$
Substrate Temperature (°C)	750	700
O_2 partial Pressure (mTorr)	100	80
Laser repetition rate (Hz)	3	5
Energy Density (J/cm^2)	1	1
Film thickness (nm)	50	110-130
Deposition Rate (nm/min)	0.80	1.80-2.20

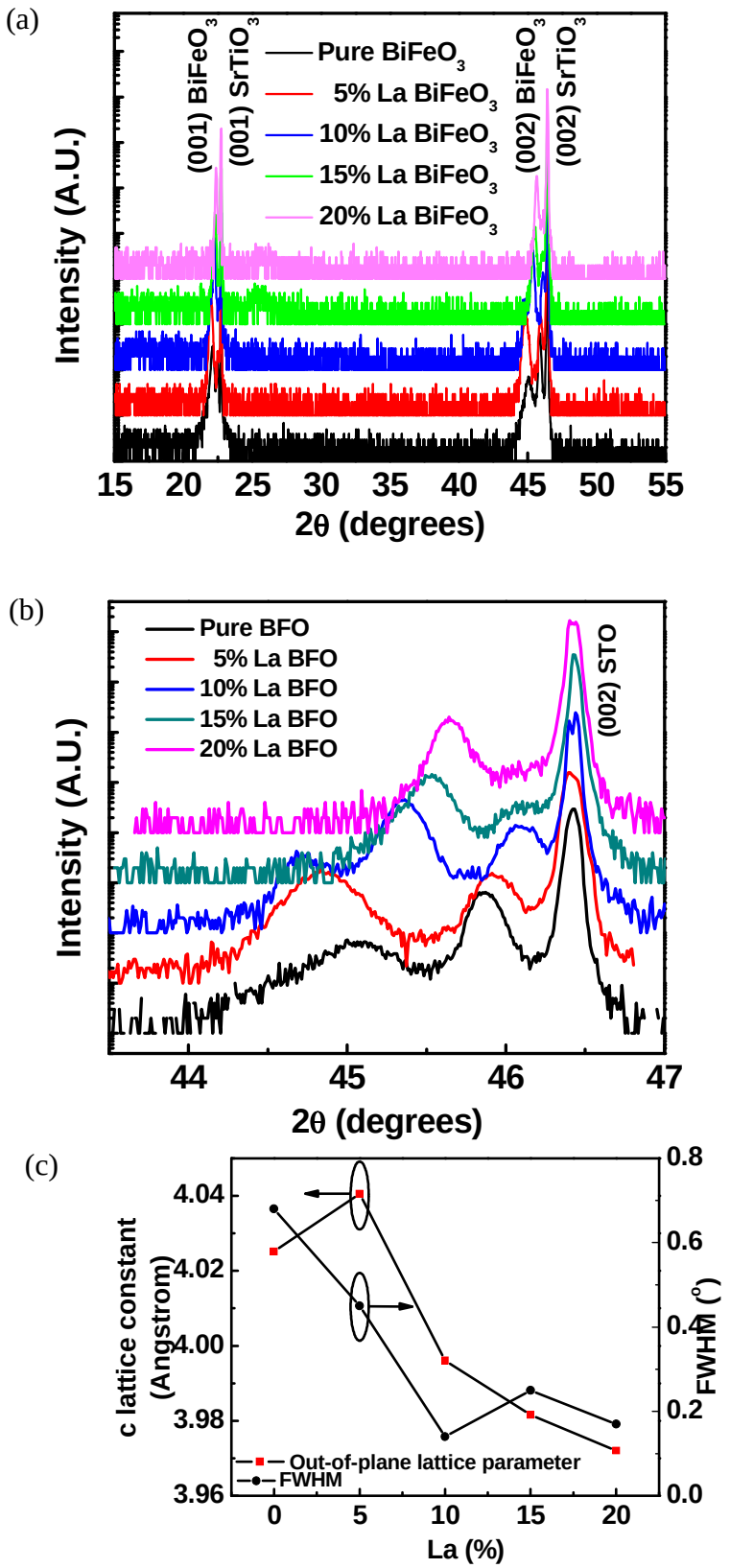

Figure 3.8. (a) High resolution XRD θ-2θ scans, (b) detailed high resolution XRD θ-2θ scans around (002) peaks of La-substituted epitaxial $BiFeO_3$ thin films grown on (001)-oriented $SrRuO_3/SrTiO_3$ substrates.

Typical θ-2θ scans of $Bi_{(1-x)}La_xFeO_3$ epitaxial thin films grown on (001)-cut $SrRuO_3/SrTiO_3$ single crystal substrates are shown in Figure 3.8 (a). Only (00l) type diffraction peaks were observed with no sign of second phase. Figure 3.8 (b) displays the enlarged scans around (002) peaks. It appears that the x=0.05 thin film shows the largest out-of-plane lattice constant, which decreases with increasing La concentration. The results are summarized in Figure 3.8 (c). A jump in the out-of-plane is clearly evident for x=0.05. The FWHM value decreases as x increases, indicating better crystallinity. However, the situation is complicated by the fact that the underlying $SrRuO_3$ layers relax to different stages, as indicated by the shift of the $SrRuO_3$ (002) peaks. For example, the $SrRuO_3$ layers, on with the x=0 and 0.5 films are grown, shows larger out-of-plane lattice parameters due to larger in-plane compressive strain. Even though this does not affect the above analysis qualitatively, a smaller in-plane strain of $SrRuO_3$ will lead to smaller out-of-plane constants for both the x=0, 0.05 samples. We still would like to eliminate this effect. Thus, a set of $Bi_{(1-x)}La_xFeO_3$ films are grown directly on $SrTiO_3$ substrate and characterized. This way, effect due to variations in the $SrRuO_3$ layer is eliminated.

Although absolute values of the out-of-plane lattice parameters for $Bi_{(1-x)}La_xFeO_3$ grown on bare $SrTiO_3$ substrate might be different from the ones grown on $SrRuO_3$, the trend should be the same and can be used to study the structure evolution. For the films grown directly on $SrTiO_3$ substrate (Figure 3.9 (a), (b)), again, no second phase was observed. The out-of-plane lattice constants are calculated and summarized in Figure 3.8 (c). It shows quite similar trend with that of $Bi_{(1-x)}La_xFeO_3$ films grown on $SrRuO_3/SrTiO_3$ substrates. However, instead of x=0.05, the sample with x=0.10 shows the largest lattice distortion. This could be due to the different lattice constant of $SrTiO_3$ and $SrRuO_3$, leading to variations in the mismatch strain of $Bi_{(1-x)}La_xFeO_3$

films. The FWHM of the (002) peaks for all samples are plotted in Figure 3.9 (c). The film with x=0.10 shows the best crystallinity among all the samples. It has been reported that the critical thickness for $BiFeO_3$ epitaxial thin film grown on $SrTiO_3$ is 20-40 nm, above which the strain relaxes progressively.[102] Overall, the FWHM values of films grown under this condition (700 ^oC, 80 mTorr, 5 Hz) are larger than that of the films grown at 700 ^oC, 100 mTorr and 5 Hz. Clearly, the growth rate affects the interface coherency significantly. This is consistent with the changes in the morphology of the films.

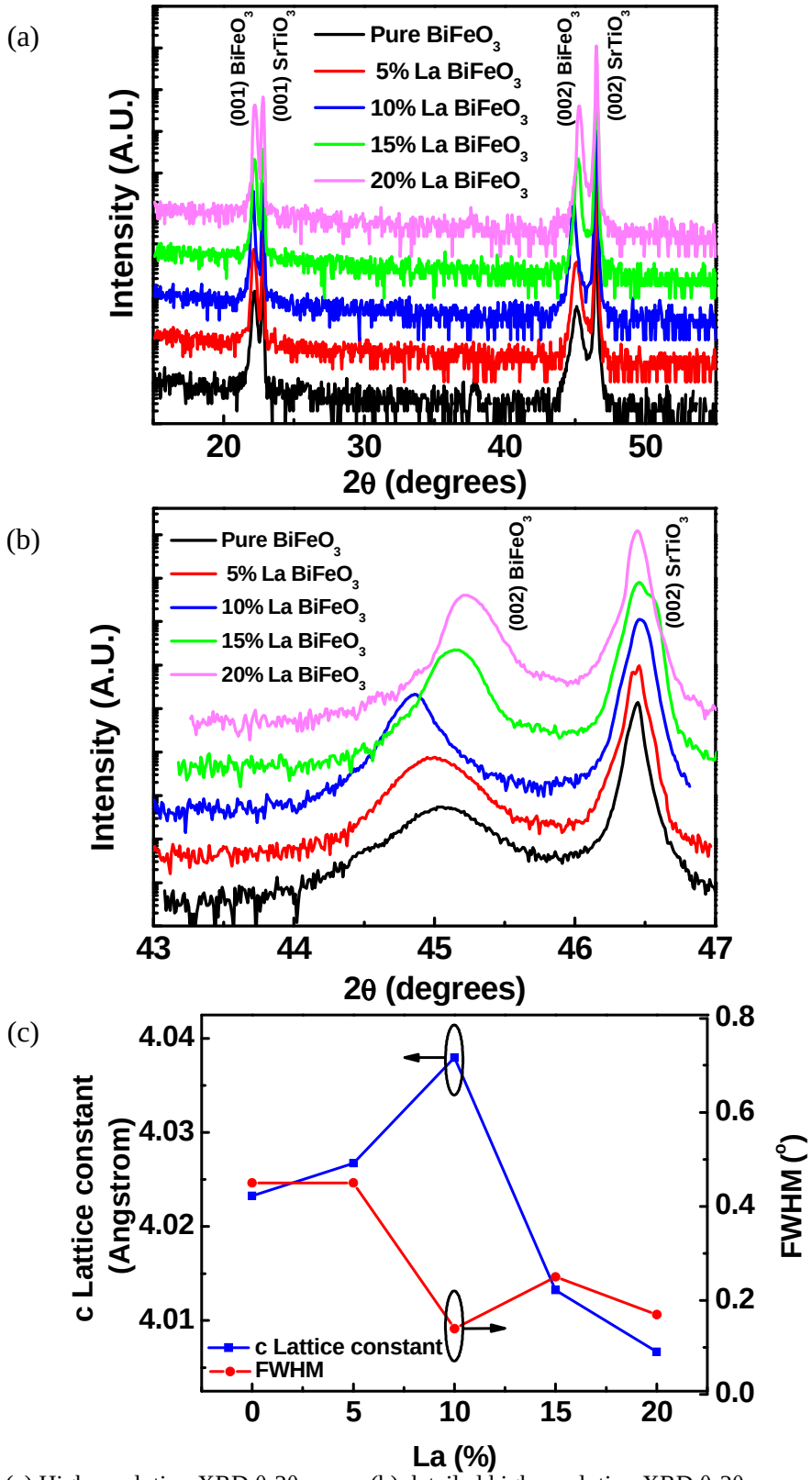

Figure 3.9. (a) High resolution XRD θ-2θ scans, (b) detailed high resolution XRD θ-2θ scans around (002) peaks and (c) change of c-lattice and full-width-half-maximum (FWHM) with respect to La content (%) of La-substituted epitaxial $BiFeO_3$ thin films grown on (001)-cut $SrTiO_3$ single crystal substrates.

3.3 Electrical Properties of $Bi_{(1-x)}La_xFeO_3$ Thin Films

3.3.1 Leakage Current Control

Figure 3.10 (a) and (b) show the leakage current density-electric field (J-E) curves and the polarization-electric field (P-E) hysteresis loops of $BiFeO_3$ epitaxial thin film measured at both room temperature and 200 K, respectively. To exclude the switching current during the J-E measurement, a pulsed DC voltage was first applied to pole the polarization into one direction. An opposite poling was applied when sweeping the electric field in the opposite direction. During the J-E measurement, the applied field was kept smaller than the coercive field (E_c) of the $BiFeO_3$ too. For the electrical measurements, the bottom electrode was always connected to ground.

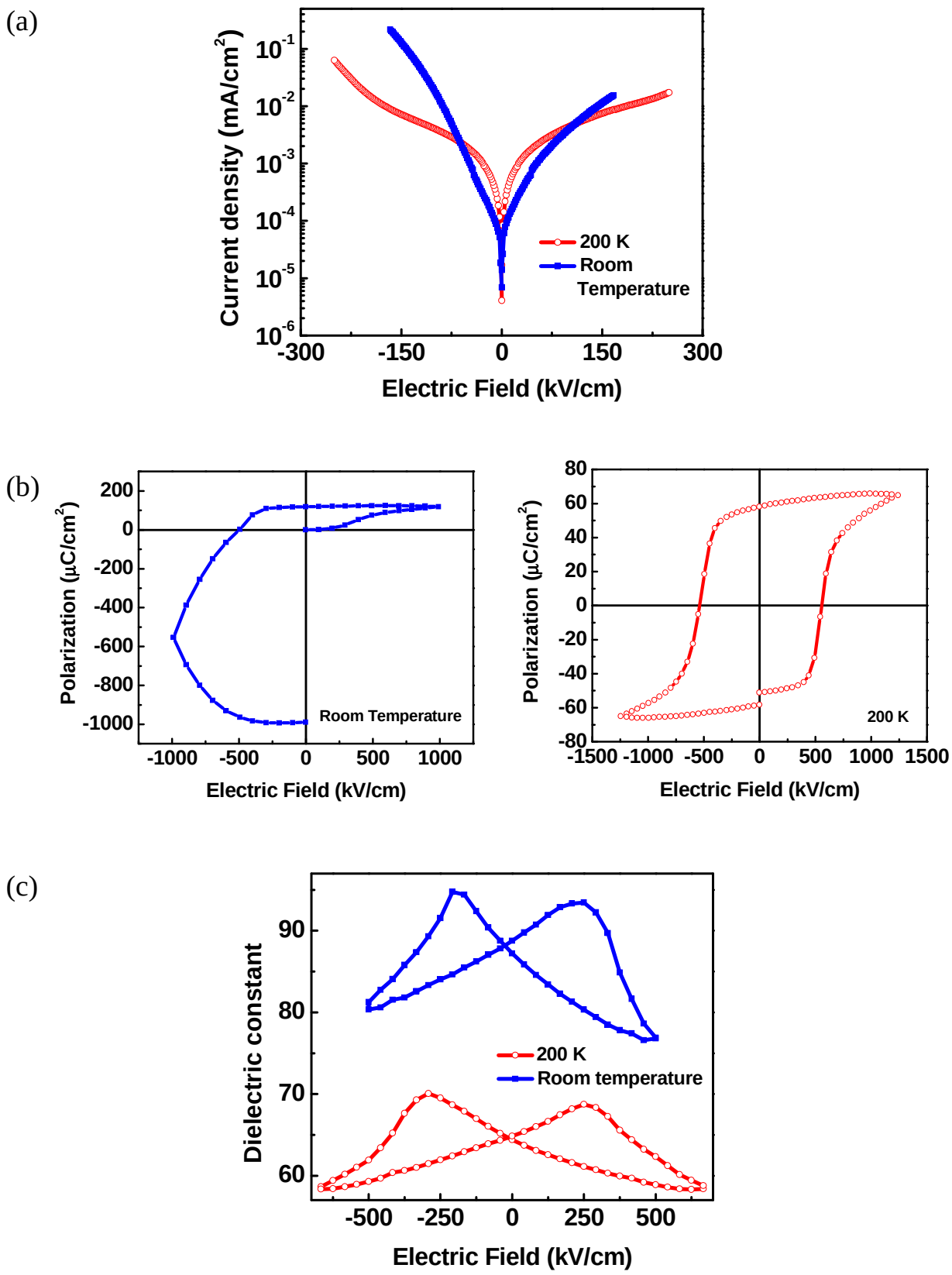

Figure 3.10. (a) I-E curves, (b) P-E hysteresis loops and (c) ε_r-E hysteresis loops of $BiFeO_3$ thin films measured at room temperature and 200K.

As shown in Figure 3.10 (a), the leakage current density of $BiFeO_3$ thin film decreases as the temperature drops to 200K. At room temperature, the $Pt/BiFeO_3/SrRuO_3$ structure shows asymmetric conduction behavior. The leakage current density is one order of magnitude higher under negative bias when the field exceeds 150 kV/cm. This is likely due to the imperfect interface between $BiFeO_3$ and Pt. The large leakage current under negative bias induces asymmetric P-E hysteresis loop measured with 2.5 kHz triangular waveform, as shown in Figure 3.10 (b). The large leakage contribution makes it difficult to assess the polarization value accurately, especially under negative bias. On the other hand, symmetric J-E curves are observed at 200 K, indicating that the interface-related leakage current is greatly suppressed. Well-saturated P-E hysteresis loop can be obtained using 1 (or 2.5) kHz triangular waveform. Both spontaneous polarization and coercive field can be obtained.

The leakage mechanism of $BiFeO_3$ thin films have been discussed intensively in the literatures. Different models have been proposed, including the bulk limited Poole-Frenkel model [103], the interface limited Space-Charge-Limited-Current model [49, 104], Schottky interface model [105] and FN model [106]. The higher leakage current observed in both the P-E and J-E measurements under negative bias is likely due to the interface between the top electrode, Pt and the $BiFeO_3$ film. One possible reason is that the higher concentration of oxygen vacancies next to the top surface of $BiFeO_3$ leads to a lower Schottky barrier. Further investigation is necessary to clarify this issue.

The $2P_r$ and E_c of the $BiFeO_3$ thin film are 110 $\mu C/cm^2$ and 390 kV/cm at room temperature, respectively. These values are measured using the PUND technique (data not shown), which eliminates the contribution from leakage current. Decreasing the temperature down to 200K allows us to obtain the symmetric P-E hysteresis loop of

$BiFeO_3$ thin film directly. The remanant polarization is close to that measured at room temperature using PUND. However, the E_c is about 550 kV/cm, larger than that measured at room temperature. This is expected as the low temperature would decrease domain wall mobility and increase domain nucleation energy. The remanant polarization of $BiFeO_3$ thin films is Bi/Fe ratio dependent, which is significantly affected by the deposition temperature and oxygen partial pressure. The measured Pr is very close to the intrinsic value reported in the literatures, indicating that the deposition conditions are fully optimized.

We have also examined the effect of measurement temperature on the dielectric behavior of $BiFeO_3$ using an LCR meter (Agilent, E4980A). For the relative dielectric constant (ε_r) measurement, a small AC signal of 100 mV (peak to peak) at 100 kHz is applied and the dc field is swept between positive bias and negative bias. Typical butterfly-type relative hysteresis loops (ε_r-E) were observed at both temperatures (Figure 3.10 (c)), where the two maximum points are due to the ferroelectric polarization reversal. The remanant dielectric constants are 87, 65 for the measurement done at room temperature and 200 K, respectively.

3.3.2 Electrical Properties

Due to the asymmetric conduction behavior of $Bi_{(1-x)}La_xFeO_3$ (x=0.00, 0.05, 0.10 and 0.20) epitaxial thin films measured at room temperature (with Pt and $SrRuO_3$ as top and bottom electrodes, respectively), we conducted electrical characterizations at 200 K except the local piezoelectric hysteresis loops. This way, the extrinsic contribution from interfaces can be eliminated.

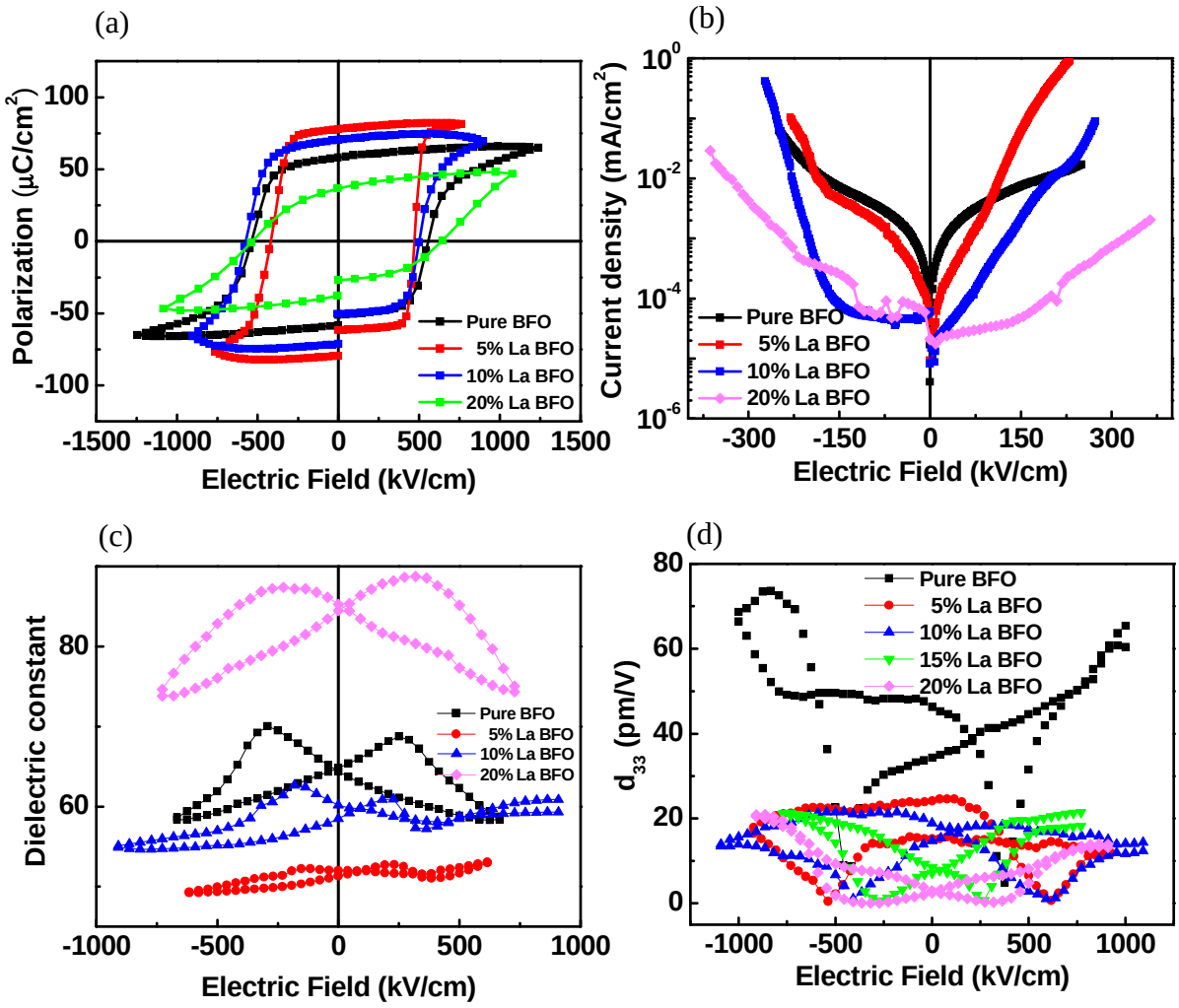

Figure 3.11. (a) P-E hysteresis loops, (b) I-E curves and (c) ε_r-E hysteresis loops and (d) d_{33}-E hysteresis loops of La-substituted $BiFeO_3$ thin films measured at room temperature and 200K.

The ferroelectric hysteresis loops of $Pt/Bi_{(1-x)}La_xFeO_3/SrRuO_3/SrTiO_3$ structure measured with 2.5 kHz triangular wave at 200K are shown in Figure 3.11 (a). Surprisingly, the remanant polarization increases first at x=0.05, then starts to drop as x continues to increase. A large $2P_r$ value of about 140 $\mu C/cm^2$ was observed for x=0.05 film. This is opposite to the results reported by Sushil K. Singh *et al.* and Hiroshida Uchida *et al.* They have measured remanant polarizations of $Bi_{(1-x)}La_xFeO_3$polycrystalline thin film grown on $Pt/Ti/SiO_2/Si(100)$ substrate by chemical solution deposition at 80 K and 10K, respectively. Decrease of the polarization is

observed for La concentration of 5%. [46, 50] More recently, Y. H. Chu *et al.* also have studied properties of $Bi_{(1-x)}La_xFeO_3$thin films and reported little change in the polarization at x=0.05. However, the films are deposited on Si substrate using $SrTiO_3$ as a buffer layer. The large mismatch between the thermal expansion coefficients of Si and perovskite oxides may be the reason for the different results. For our samples, as the La concentration increases to above 5%, the coercive field continues to increase while the remanant polarization continues to decrease. The hysteresis loop at x=0.05 is the most square and the loops become more canting as the La content increases. Surprisingly, ferroelectric property still exists in samples with x=0.20. The change in polarization of the $Bi_{(1-x)}La_xFeO_3$ thin films as a function of x is consistent with the change in the lattice parameters. However, we observe increase in the coercive field. This is different from literature reports and the reason is not clear. Y. H. Chu *et al*. reported smaller coercive field for $Bi_{(1-x)}La_xFeO_3$thin films grown on Si substrate and proposed that the reduction is due to the change in the rhombohedral angle and increment in domain wall density.[107] Y. Wang *et al.* also observed similar phenomena in $Bi_{(1-x)}La_xFeO_3$polycrystalline thin films and attributed it to the reduction in charged defects concentration. Such defects may serve as pinning centers that impede the domain wall motions. [108]

Figure 3.11 (b) compares the J-E characteristics of $Bi_{(1-x)}La_xFeO_3$ samples. Much smaller leakage current density at low field region is observed as compared with that of the pure $BiFeO_3$, especially for x=0.15, 0.20 samples. This could be due to the fact that Bi is very volatile and easily evaporates during thin film deposition, leading to Bi vacancies, V_{Bi}". When some of the Bi is replaced with La, less cation vacancies are generated. This is supported by the fact that the chemical bond strength of La-O bond (799±4 kJ/mol) is much larger than Bi-O bond (~337±16 kJ/mol). [109]

Typical butterfly-shape ε_r-E hysteresis loops are observed for all samples, where the two maximum points are due to the ferroelectric polarization reversal. This confirms the existence of ferroelectricity in films with 20% La content. The results were plotted in Figure 3.11 (c), showing opposite trend to the Pr as La content increases. Again, such transition suggests the possibility of a phase transition at x=0.5.

The piezoelectric responses of $Bi_{(1-x)}La_xFeO_3$ films are obtained by using PFM technique equipted with an external lock-in amplifier and DC voltage source. Pt/Ir-coated heavily doped Si tips with a force constant of ~42 N/m and resonance frequency of ~320 kHz are used in the piezoelectric hysteresis loop measurements. The tips are placed on the surface of the sample while the bottom $SrRuO_3$ electrode is grounded. The quantitative result is obtained by calibrating the PFM output using a sample with known d_{33} value (X-cut quartz in this case, d_{11}=2.3 pm/V). The d_{33} of the films are then calculated using $d_{33film}= (A/A_0)d_{11quartz}$, where A is the lock-in amplifier reading divided by the AC peak-to-peak voltage used to excite sample vibration and A_0 is the corresponding value for quartz. The d_{33}-E hysteresis loops of $Bi_{(1-x)}La_xFeO_3$ thin films are shown in Figure 3.11 (d). Note that the measured out-of-plane piezoelectric coefficients are effective values owing to the elastic constraint imposed by the substrate. The results show different trend from the ε_r-E hysteresis loops. Across the d_{33}-E hysteresis loops with increasing La contents, no abrupt increment was observed. The remanant out-of-plane piezoelectric coeffcient drops from 40.29 pm/V for pure $BiFeO_3$ to 2.44 pm/V for x=0.20. The dependence of d_{33} on the applied electric field due to intrinsic lattice contribution, with no contributions from ferroelastic domain motion or field-induced phase transition, along [001] is given by,

$$d_{33}(E) = 2\varepsilon_0 \varepsilon_{\text{int}}(E) Q_{eff} P(E),$$

where ε_0 is the free space permittivity, ε_r is the intrinsic relative permittivity, Q_{eff} is the effective electrostrictive coefficient that accounts for the clamping effect of the substrate and P is the polarization. Apparently, the field dependence of d_{33} is governed by the field dependence of both polarization and dielectric susceptibility. Since the trends of remanant polarization and relative dielectric constant curves as function of La concentration are opposite, the occurrence of phase transition cannot be concluded from the continuous decreasing trend of remanant $d_{33.}$ Compared with Y. H. Chu *et al.* results, they measured a higher remanant piezoelectric coefficient of 45 pm/V for the 10% La-doped BFO thin film. No systematic study as a function of La concentration was reported though. [107]

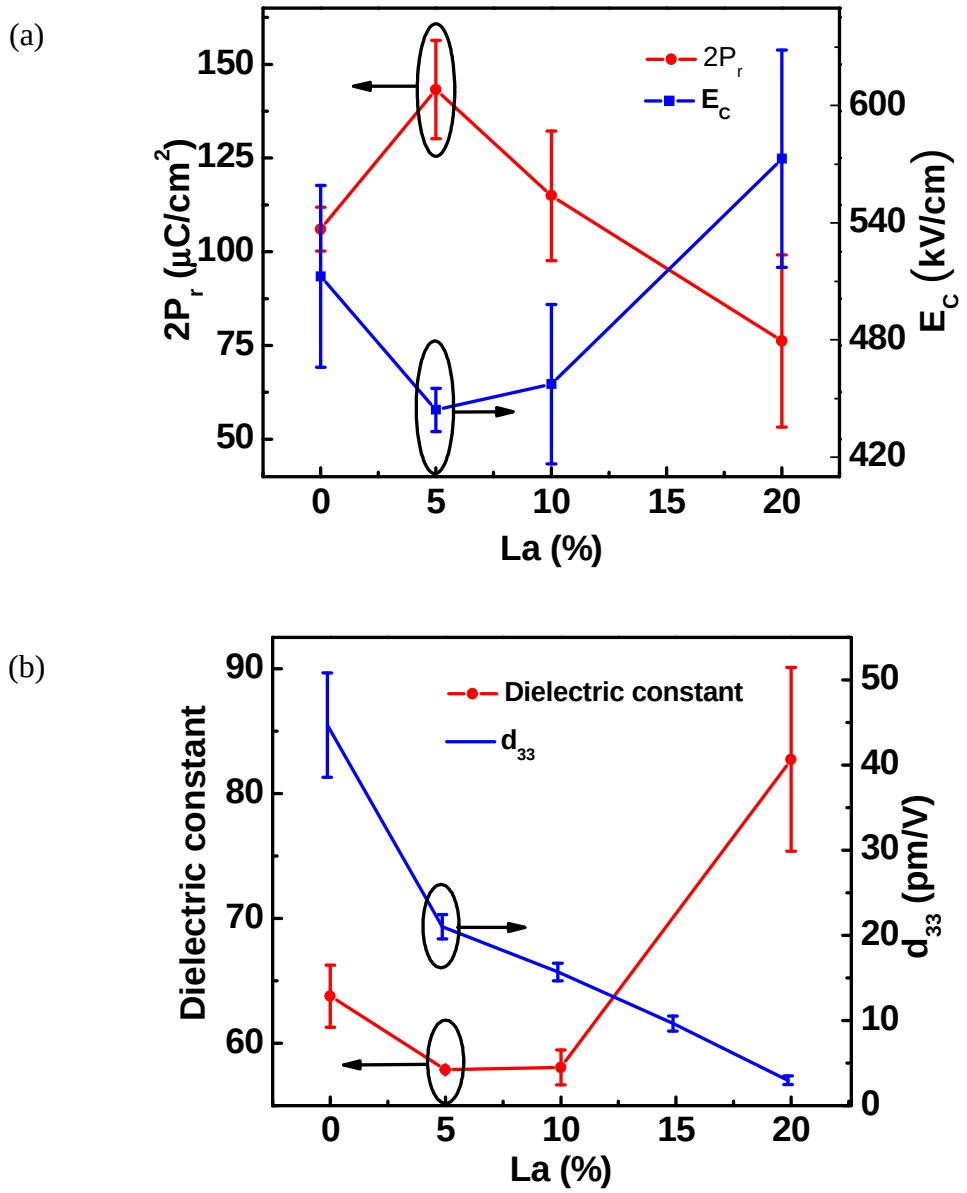

Figure 3.12. (a) Plot of remanant polarization, 2Pr and coercive field, Ec and (b) Plot of remanant out-of-plane dielectric constant and remanant out-of-plane piezoelectric coefficient, d_{33} as a function of increasing La content in $BiFeO_3$ epitaxial thin films. (All measurements were done at 200K except piezoelectric coefficient, d_{33} at room temperature.)

The changes in electrical properties as functions of La content are summarized in Figure 3.12. When analyzed together with the lattice constant evolution (Figure 3.8), the observations are rather consistent. There are two possible explanations, i) a phase transition from distorted rhombohedral to orthorhombic/tetragonal at around x=0.05-0.10 or ii) a larger rhombohedral angle as the result of La-substitution. In these two hypothesis, the spontaneous polarization rotates towards the (001)c direction, leading to the initial increase in the observed Pr for x=0.05. Further increase in the La content should decrease the spontaneous lattice distortion and polarization, due to the lack of s lone pair electrons.

In order to demonstrate the above phenomenon, we have conducted detailed crystal structure analysis using reciprocal space mapping (X'Pert PRO MPD). Figure 3.13 and 3.14 shows the reciprocal space mappings of $Bi_{1-x}La_xFeO_3/SrTiO_3$ and $Bi_{1-x}La_xFeO_3$/ $SrRuO_3/SrTiO_3$ epitaxial thin films, respectively, around (002) and (103) peaks. To analyse the film structure accurately, it is important to first check if the (002) plane of $Bi_{1-x}La_xFeO_3$ films are parallel to the substrate. In the (002) mapping of $Bi_{1-x}La_xFeO_3/SrTiO_3$ films, the strong reflection is identified as the (002) peak of the $SrTiO_3$ substrate whereas the second spot is the (002) peak of the $Bi_{1-x}La_xFeO_3$ film. For $Bi_{1-x}La_xFeO_3$/ $SrRuO_3/SrTiO_3$ films, a third spot between the $SrTiO_3$ and $Bi_{1-x}La_xFeO_3$ reflections is identified as from $SrRuO_3$. ω measures the relative angle between the (002) planes of the substrate and the $Bi_{1-x}La_xFeO_3$ film. The centers of both spots are at the same ω, indicating that the (002) planes of $Bi_{1-x}La_xFeO_3$ films are parallel to the substrate.

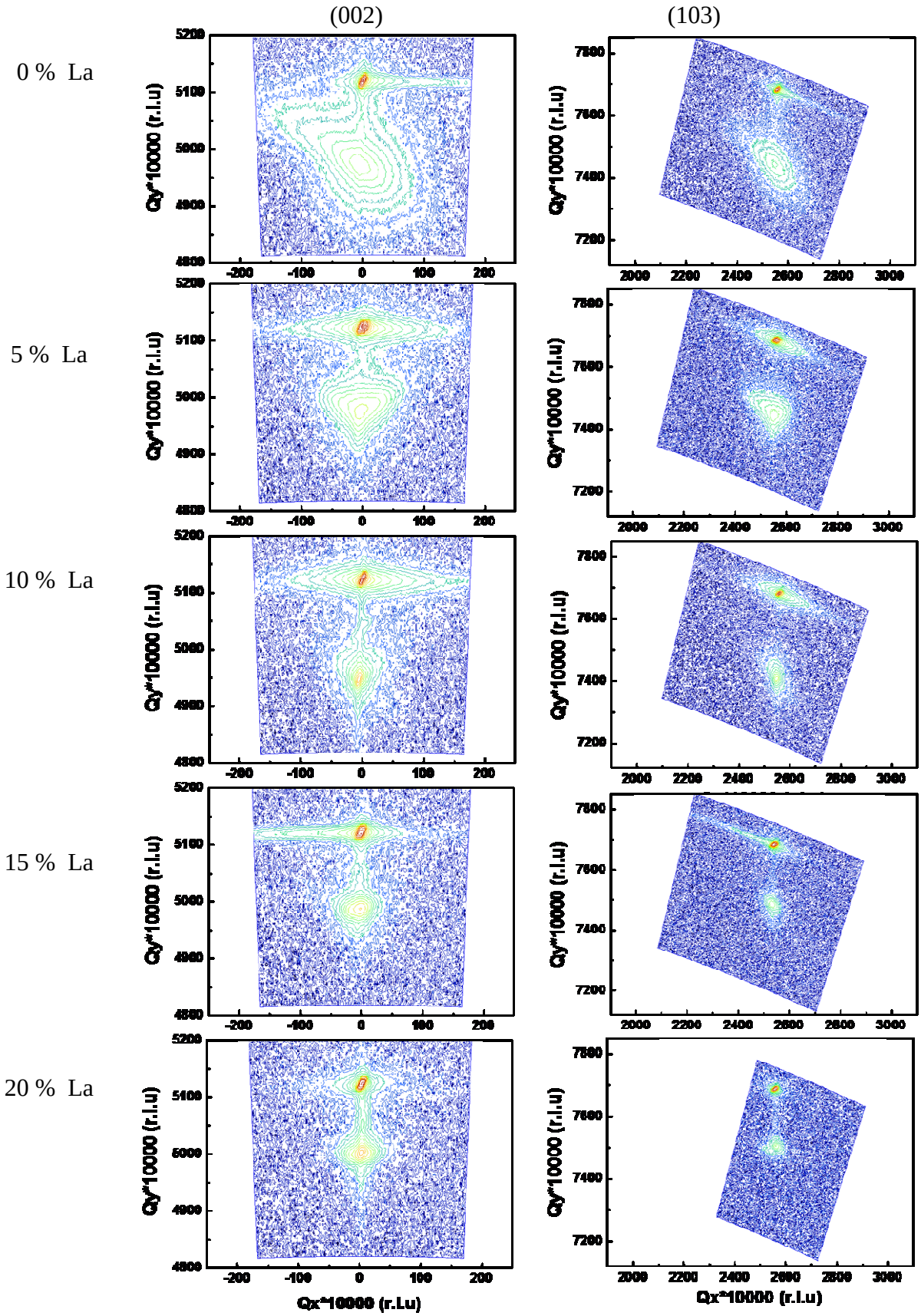

Figure 3.13. Reciprocal space mapping of 0%-20% La-substituted BiFeO3 epitaxial thin films deposited on (001)-cut SrTiO3 substrate at 700 oC, 5 Hz, 80 mTorr around the (002) and (103) peaks.

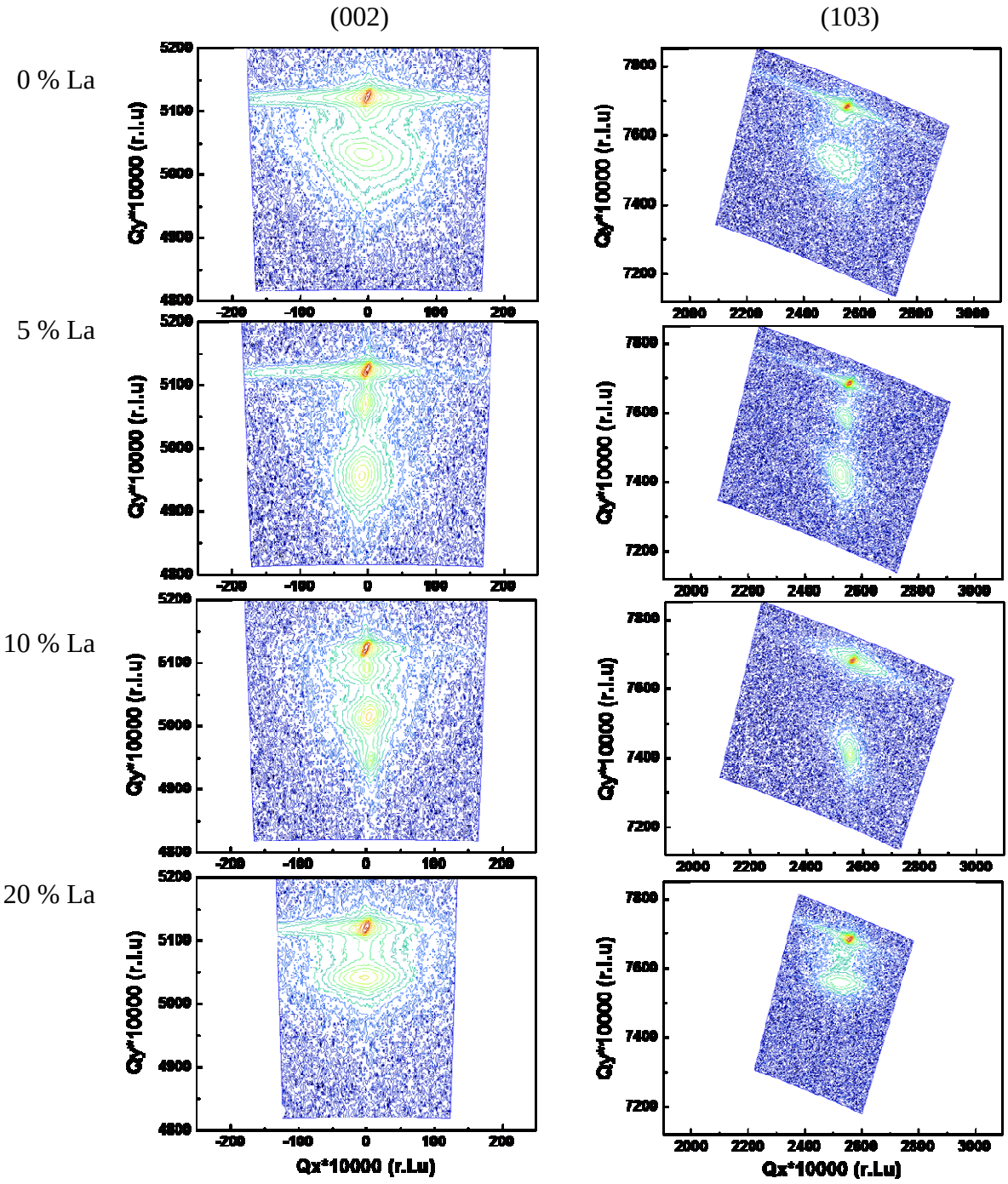

Figure 3.14. Reciprocal space mapping of 0%-20% La-substituted $BiFeO_3$ epitaxial thin films deposited on (001)-cut $SrRuO_3/SrTiO_3$ substrate at 700 ^oC, 5 Hz, 80 mTorr around the (002) and (103) peaks

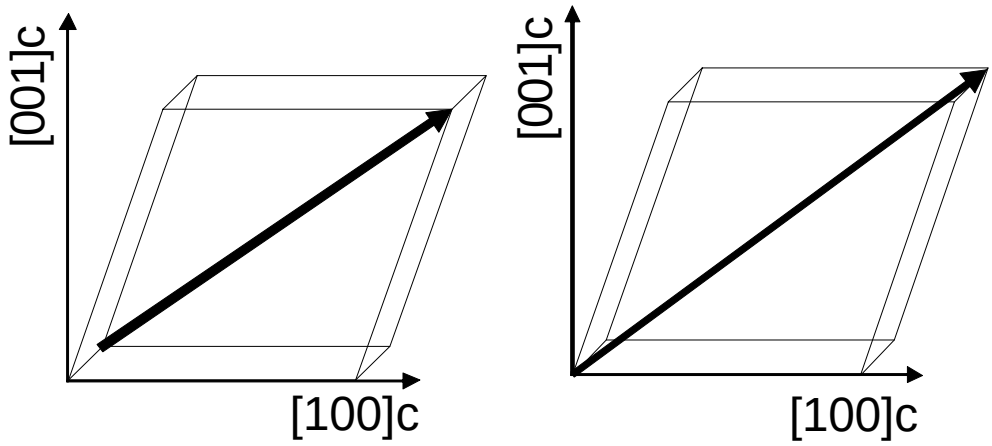

Figure 3.15. Schematics illustrating two structure variants with similar (103) d-spacing but different (013) d-spacings.

To further analyse the crystal structure, the $Bi_{1-x}La_xFeO_3$ films are mapped around the (103) peak. The strongest spot is the (103) diffraction of $SrTiO_3$ whereas the second and third spots are from $SrRuO_3$ and $Bi_{1-x}La_xFeO_3$ films, respectively. No peak splitting is observed in the (103) $Bi_{1-x}La_xFeO_3$ peaks. For the rhombohedral structure of $BiFeO_3$ with four structural variants, two spots corresponding to the $(\bar{1}03)$ and (103) peaks will appear at different angle ω to the (103) peak of the $SrTiO_3$ substrate. However, only one spot is observed. Similar results are observed for the rest of the films. This could be due to the existence of two structure variants with 71° domains and the scanning is along the direction with no difference in d-spacing as shown in Figure 3.15. This observation could be supported by the PFM images.

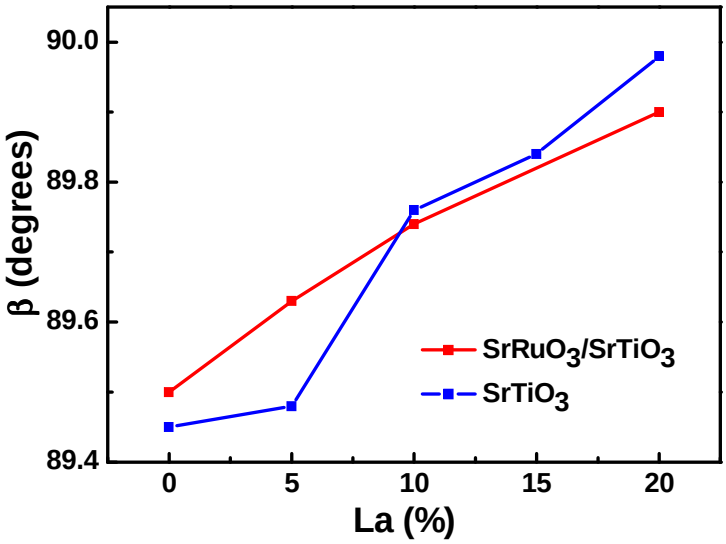

Figure 3.16. The change of rhombohedral angle, β of La-substituted $BiFeO_3$ epitaxial thin films grown with/without $SrRuO_3$ on $SrTiO_3$ substrate.

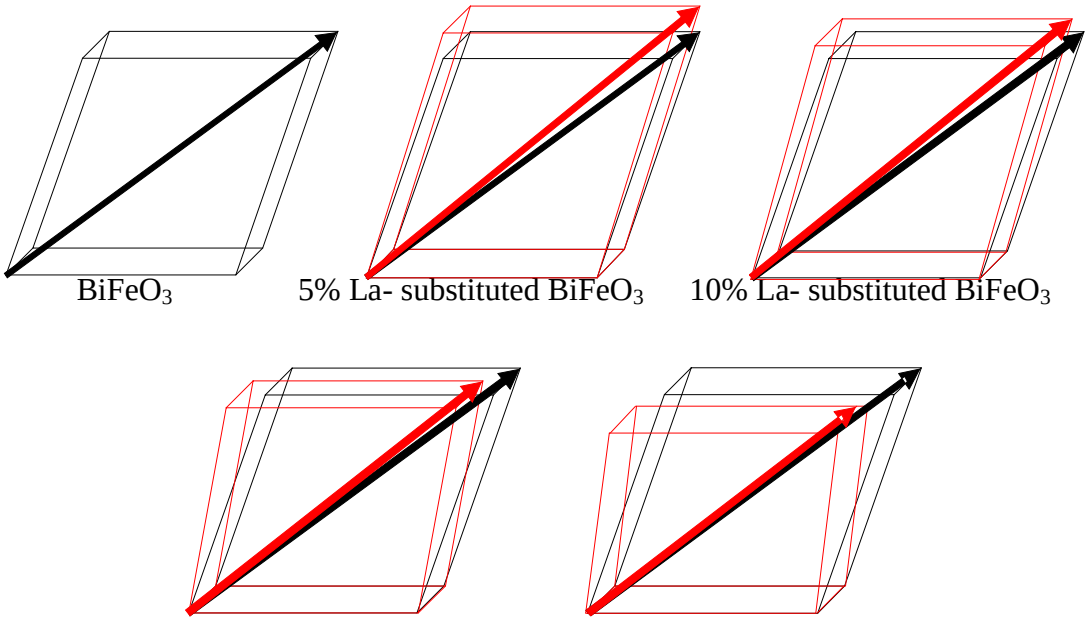

Figure 3.17. Schematics illustrating the change of rhombohedral angle due to the rotation of the spontaneous polarization as a function of La content.

To correlate the change of electrical properties with different La concentration with films structure, further analysis on the rhombohedral angle is conducted as shown in Figure 3.16. The rhombohedral angle, β increases continuously from pure $BiFeO_3$ to 20% La-substituted $BiFeO_3$. No clear phase transition is observed though. The spontaneous polarization rotates towards the (001)c direction, leading to the initial increase in the observed lattice distortion and remanant polarization. Upon further increase of La concentration, the spontaneous polarization decreases due to the lack of s lone pair electrons in La. This new model is shown in Figure 3.17. However, it is apparent that the larger tilting of rhombohedral angle alone is not enough to generate large dielectric and piezoelectric responses. Both end members have to be piezoelectric active, meaning they have to posses either ferroelectric or antiferroelectric orders. $LaFeO_3$, however, does not have ferroelectric order.

3.3.3 Ferroelectric Domain Structures

We have investigated the ferroelectric domain structures of the $Bi_{(1-x)}La_xFeO_3$ thin films as a function of La concentration. In ferroelectric films, elastic domains will form to release the substrate constrain. Thus it is expected that the domain size (domain density) will be affected by the coherency of the film/substrate interface.

Films deposited directly on (001) $SrTiO_3$ substrates with and without the $SrRuO_3$ layer are tested. For this study, two deposition conditions are used. One set of samples are deposited at 700 ^oC, 5 Hz, 100 mTorr and the other set at 700 ^oC, 5 Hz and 80 mTorr. As we have discussed previously, a small amount of second phase does not affect film domain structure significantly. Since $BiFeO_3$ films deposited at 100mTorr shows regular IP domain structures, it is interesting to see how this is affected by the La substitution.

Typical θ-2θ scans for the films grown under 100mTorr oxygen partial pressure are shown in Figure 3.18 (a) and (b). The out-of-plane lattice constants and FWHM values of the (002) peaks are calculated and shown in Figure 3.14 (c). Unlike samples grown under 80 mTorr, a monotonic decrease of the out-of-plane lattice parameter is observed with no sign of phase transition. Note that the lattice parameters of these films are all larger than their counterpart grown under 80 mTorr. For example, c=0.4068nm here for $BiFeO_3$ as compared to 0.4023nm for films grown under 80 mTorr. So it is possible that the films grown under 100 mTorr are all fully strained. If this is the case, then any lattice change due to phase transition may be overwhelmed by the large lattice mismatch strain between the $SrTiO_3$ and the $Bi_{(1-x)}La_xFeO_3$ films. One evidence for this hypothesis is the FWHM values. The FWHM of the (002) peaks are very small, in the range of 0.09-0.11, for all samples. Compared with the films grown under 80mTorr oxygen pressure, these values are considerably smaller, indicating

much better crystallinity. Lower growth rate at high pressure, leading to coherent film/substrate interface, is believed to be the reason. So the observations here do not preclude the possibility of a phase transition upon La substitution. It also suggests that strain affects the structure of $Bi_{(1-x)}La_xFeO_3$ significantly and offers a possible explanation for the difference between our results and that of Chu *et al*. For $Bi_{(1-x)}La_xFeO_3$ films deposited on $SrRuO_3/SrTiO_3(001)/Si(001)$ substrate, they reported no lattice change up to 15% La, except at 20% when a phase transition from rhombohedral to orthorhombic occurs. It is possible that the much smaller thermal expansion coefficient of Si leads to a tensile stress in the film, pushing the phase transition point from La content of ~5%-10% to 20%.

(a)

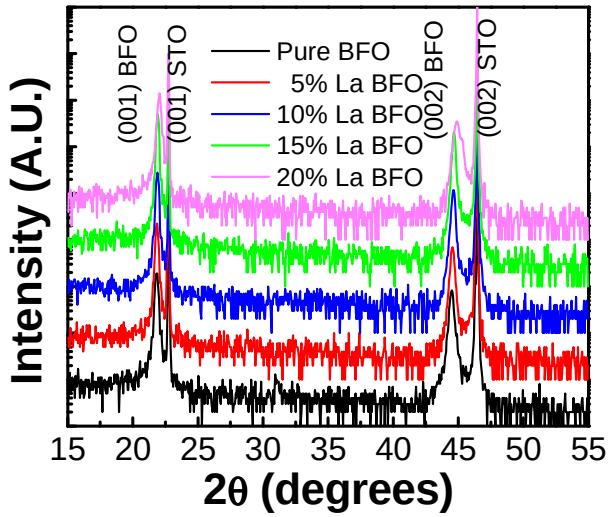

(b)

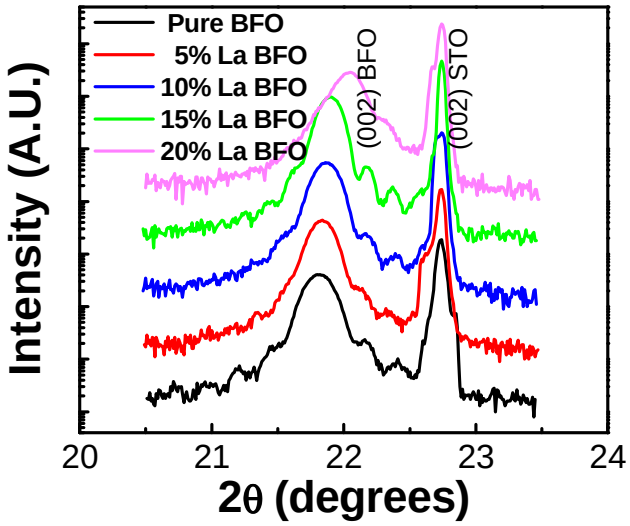

(c)

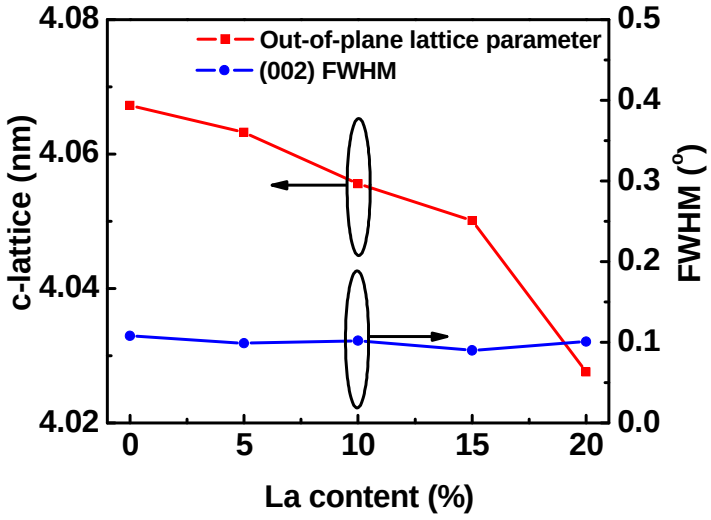

Figure 3.18. (a) XRD θ-2θ scans, (b) detailed XRD θ-2θ scans around (002) peaks and (c) change of c-lattice and FWHM with respect to La content (%) of 0%-20% La-substituted epitaxial $BiFeO_3$ thin films on (001) cut $SrTiO_3$ at 700 ^oC, 5 Hz, 100 mTorr.

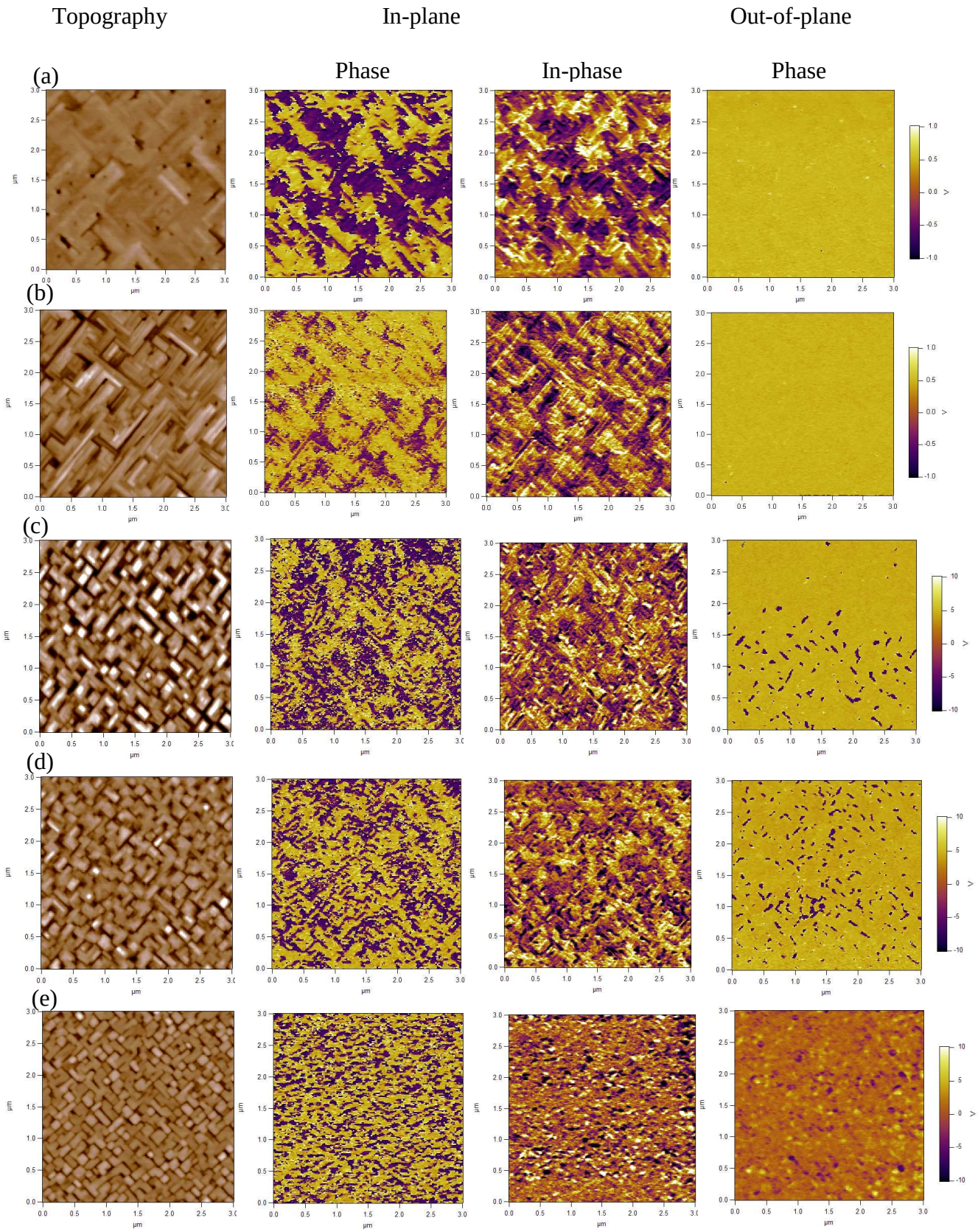

Figure 3.19. (a)-(e) The topography and domain structure images of 50nm 0%-20% La-substituted $BiFeO_3$ film grown on (001) $SrTiO_3$ substrate at 700 ^oC, 5 Hz, 100 mTorr.

As reported previously, $BiFeO_3$ films grown under 100 mTorr (700 ^oC, 5 Hz) shows regular IP domains. We have studied the influence of La on the domain structure of $BiFeO_3$ thin films grown under the same condition. Figure 3.19 (a)-(e) shows the topography, in-plane (phase and in-phase) and out-of-plane (phase) PFM images of $Bi_{(1-x)}La_xFeO_3$ thin films grown on bare (001)-cut $SrTiO_3$ single crystal substrates. The in-phase images contain all the information from both the in-plane amplitude and phase images. Regular IP domains are observed up to x=0.15.

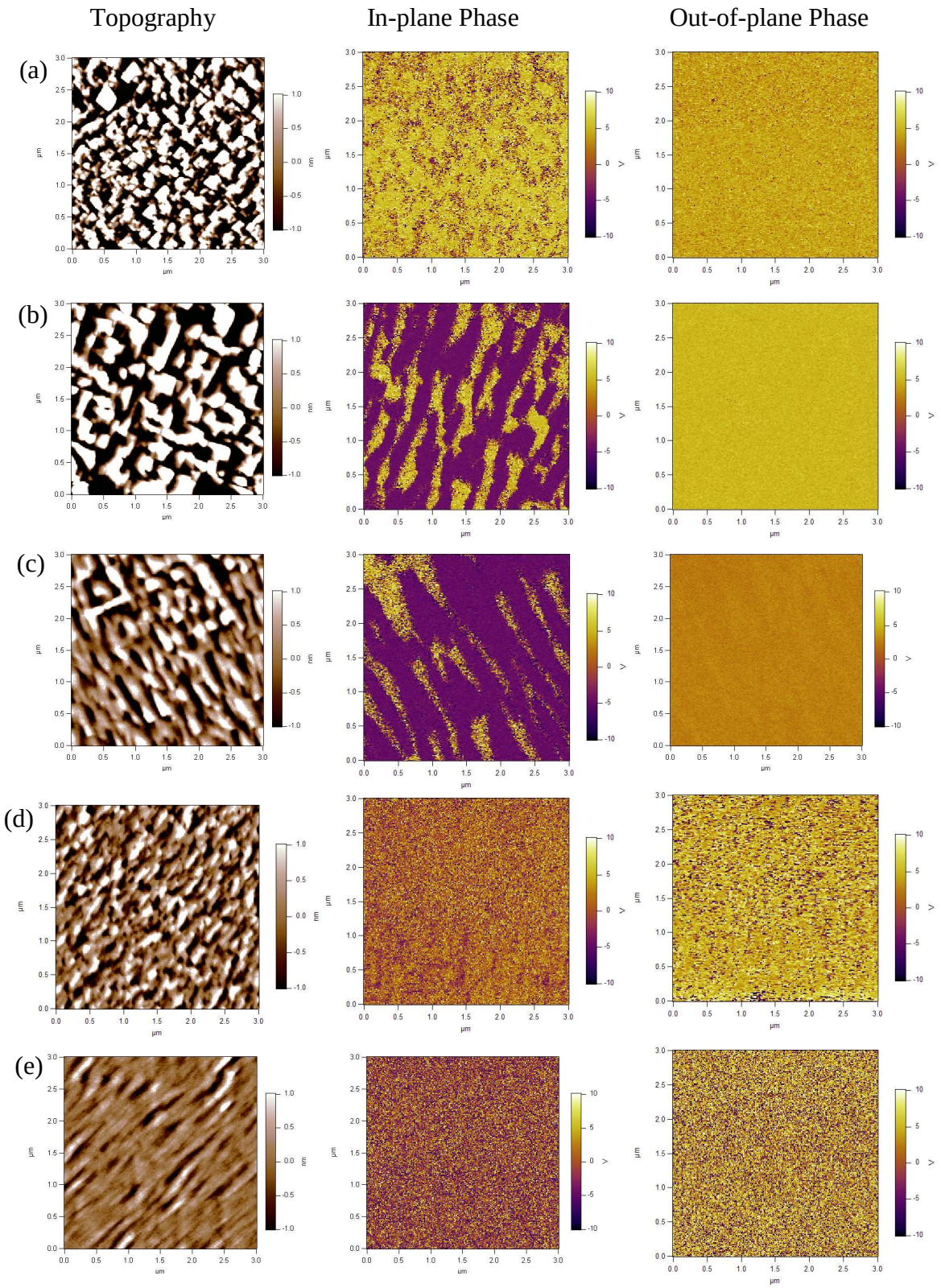

Figure 3.20 (a)-(e) Topography, in-plane phase and out-of-plane phase PFM images of 0%-20% La-substituted $BiFeO_3$ deposited directly on (001)-cut $SrTiO_3$ substrate at 700 ^oC, 5 Hz, 80 mTorr.

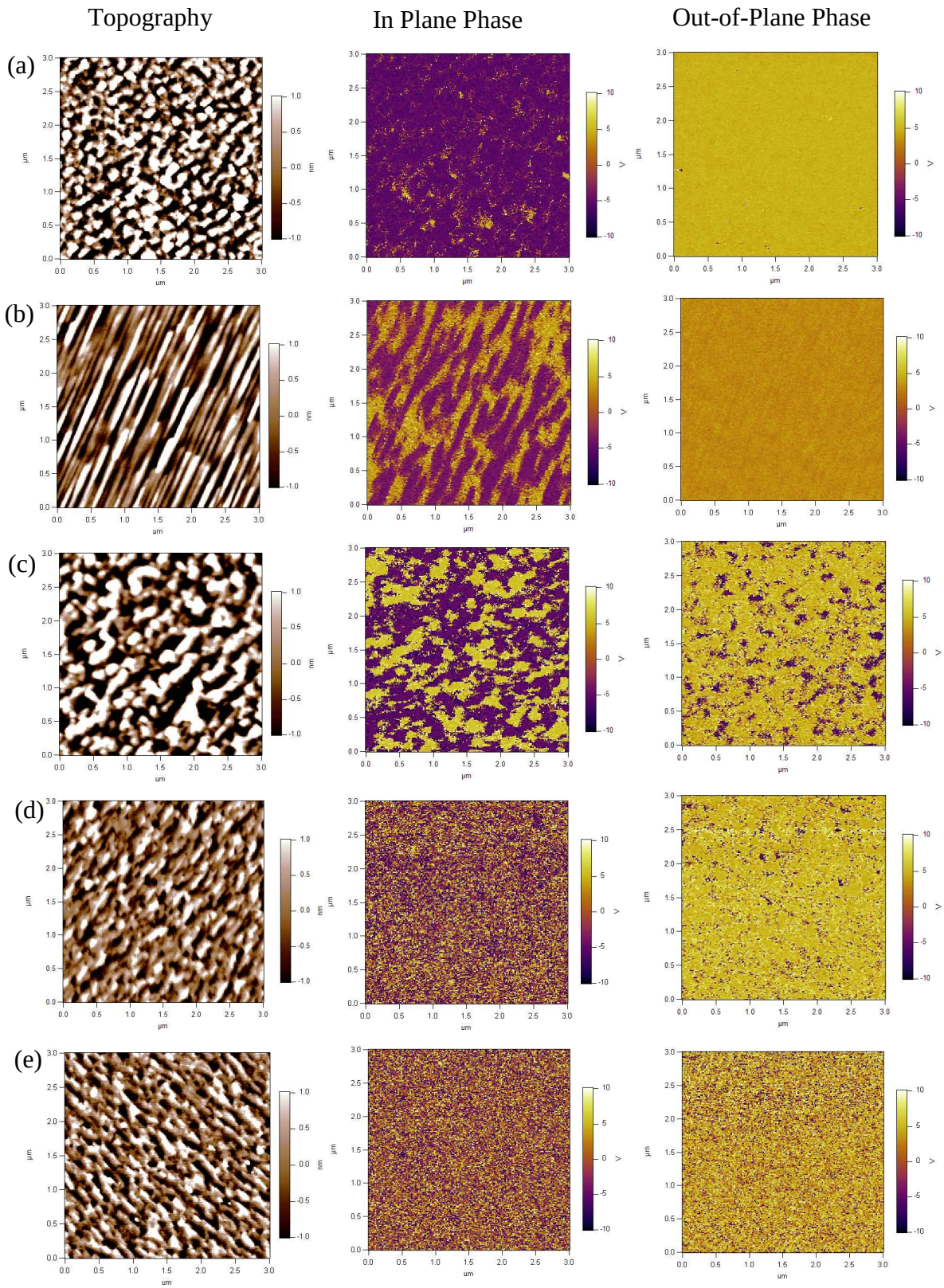

Figure 3.21. (a)-(e) Topography, in-plane phase and out-of-plane phase PFM images of 0%-20% La-substituted $BiFeO_3$ deposited on (001)-cut $SrRuO_3/SrTiO_3$ substrate at 700 ^oC, 5 Hz, 80 mTorr.

It is interesting to note that when the films are deposited under 80 mTorr oxygen partial pressure, the results are very different. The domain structure as a

function of La content for thin films deposited on (001)-cut $SrTiO_3$ substrate and (001) $SrRuO_3/SrTiO_3$ substrate are shown in Figure 3.20 (a)-(e) and Figure 3.21 (a)-(e), respectively. Under this deposition, $BiFeO_3$ films don't show regular IP domain structures. But regular domains are observed for x=0.05 and 0.10 on $SrTiO_3$ substrates and for x=0.05 on $SrRuO_3/SrTiO_3$ substrates. The IP domain structures of these three samples are similar to the stripe domains of pure $BiFeO_3$ deposited on $SrTiO_3$ substrate under 100 mTorr oxygen pressure. But the average domain size is much larger. The origin of such domain patterns is not clear. But note that the morphologies are rather different for films grown under 80 mTorr oxygen pressure, likely due to the higher growth rate. Previous analysis also shows less in-plane compressive strains in these samples, which means less domains are needed to release the elastic energy, thus the larger domain size. Comparing the samples with/without $SrRuO_3$, it is clear that the $SrRuO_3$ played a role in this case, consistent with the hypothesis that strain is a main factor in determining the domain structures.

Another possible cause is the variation of Curie temperature of $BiFeO_3$ upon La substitution. At certain concentration of La, the deposition temperature may be above the Curie temperature of the film. The stripe domains may be formed during the cooling from paraelectric phase.

3.3.4 Optical Properties of $Bi_{(1-x)}La_xFeO_3$

I) Tuning the Bandgap of $BiFeO_3$

Optical properties of $BiFeO_3$ have been investigated both experimentally and theoretically. Results from polycrystalline films, nanowires, bulk single crystals and epitaxial films lead to bandgap values ranging from 2.3 to 2.8 eV. [110-114] Some researchers report that the bandgap is direct. [110, 111] Others believe it is indirect. [115, 116] Several theoretical calculations have also been conducted and predicted that the bandgap of $BiFeO_3$ is within or near the visible range. Neaton *et al.* using LSDA + U method to study the spontaneous polarization in $BiFeO_3$ and obtained a bandgap value of about 1.9 eV. [117] According to S. J. Clark *et al.*, $BiFeO_3$ is a semiconductor with a room temperature bandgap of 2.8 eV. This value is obtained using screened-exchange density functional theory approximation. [118] Both calculations yielded a slightly indirect bandgap.

Tuning the bandgap of $BiFeO_3$ is of practical interest for both the leakage current control and electro-optical device applications. Experimental investigation of the electronic structure, especially the bandgap of $BiFeO_3$ film, is of particular importance for both scientific understanding and potential technological applications. In this section, we report the characterization of bandgap of epitaxial $Bi_{(1-x)}La_xFeO_3$ thin films. UV-visible absorption spectroscopy is used to probe the electronic structure of $Bi_{(1-x)}La_xFeO_3$ (x=0, 0.05, 0.10, 0.15 and 0.20) epitaxial thin films deposited on (001)-cut single crystal STO.

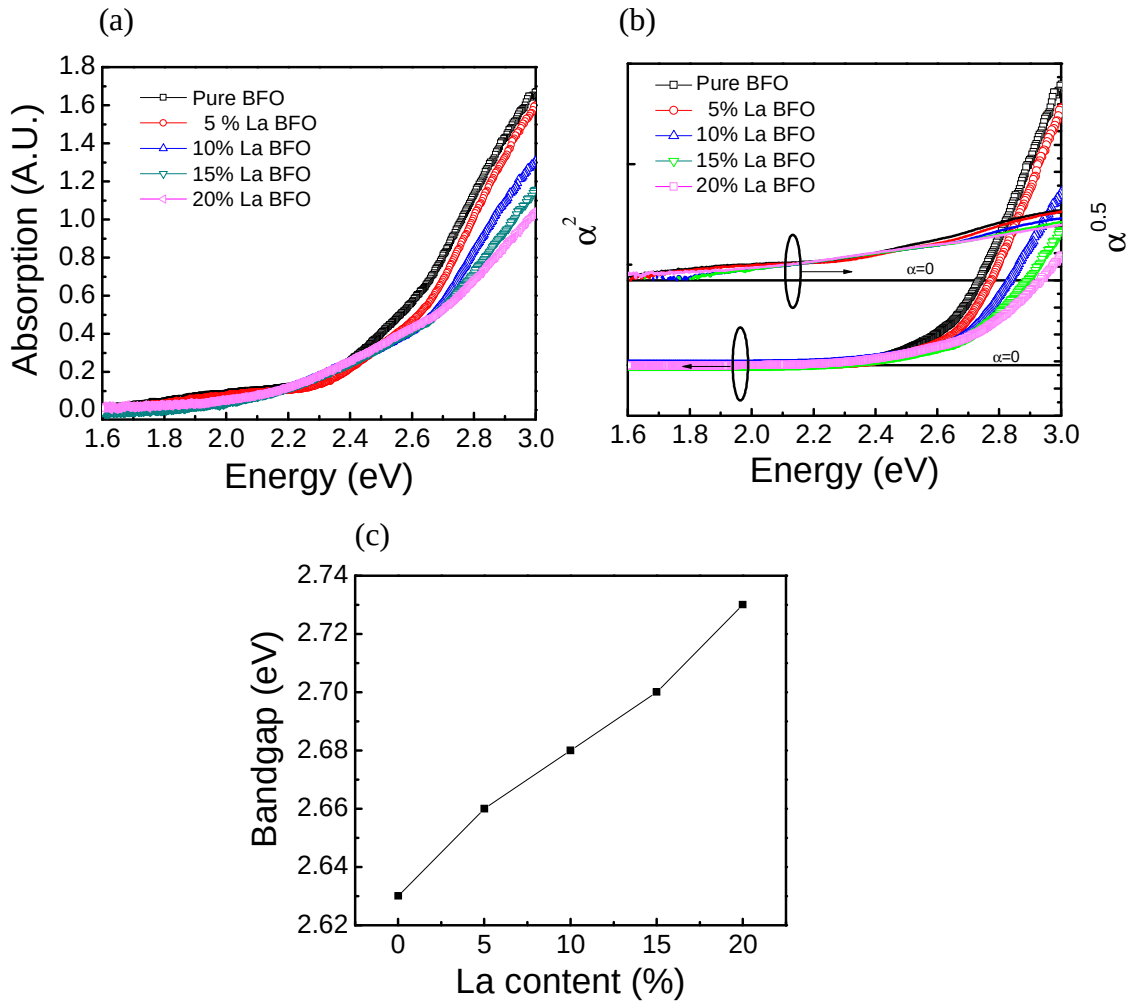

Figure 3.22. (a) Absorbance of UV-visible spectrums, (b) correlations between direct and indirect bandgaps and (c) plots of optical bandgap from direct bandgaps aspect for 0- 20% La-substituted epitaxial $BiFeO_3$ thin films on (001) oriented $SrTiO_3$.

The UV-visible absorption spectrums of $BiFeO_3$ at room temperature with different La concentration are shown in Figure 3.22(a). The absorption edge is shifted towards shorter wavelengths upon increase of La content. Simple linear extrapolation of the α-E plots is not the accurate way to determine bandgap. The nature of bandgap i.e. direct or indirect has to be determined first.

The absorption coefficient, α, in solids that may have contributions from both the direct and indirect bandgap transitions, is given by [119, 120]

$$\alpha = AA^{*}(h\nu - E_{g,dir})^{0.5} + B\frac{(h\nu - E_{g,ind} + E_p)^2}{\exp(\frac{E_p}{kT}) - 1} + B\frac{(h\nu - E_{g,ind} - E_p)^2}{1 - \exp(-\frac{E_p}{kT})}, \quad (4.11)$$

where $E_{g,dir}$ and $E_{g,ind}$ are the direct and indirect bandgaps, respectively. E_p is the emitted (absorbed) phonon energy that assists in the transition, A and B are constants, A* is a frequency-independent constant, k is Boltzmann's constant and T is temperature. Hence, it can be inferred that a direct bandgap would lead to a straight line when plot α^2 as a function of photon energy and it can be calculated by extrapolating the straight line to the α=0 point. For an indirect bandgap, a straight line would be observed when plotting $\alpha^{0.5}$ versus photon energy. Both plots are shown in Figure 3.22 (b) for the $Bi_{(1-x)}La_xFeO_3$ films and it is clear that the curves fit direct-bandgap relationship better . By extrapolating the lines to the α=0 points, it is obtained that the bandgap of $Bi_{(1-x)}La_xFeO_3$ increases from 2.63eV for pure $BiFeO_3$ to 2.73eV for x=0.20. The measured bandgaps are within the range of reported values. It is not clear whether the increase in bandgap value is intrinsic or due to elimination of shallow traps next to the band edges. Theoretical investigation has been carried out to clarify this issue (section 3.4). Either way, it is believed that the increase in bandgap leads to improvement in resistivity of the $Bi_{(1-x)}LaxFeO_3$ thin films at higher La content, as reported in section 3.3.3

II) Photovoltaic Effect in $Bi_{(1-x)}La_xFeO_3$ Thin Films

Because of the relative small bandgap of $BiFeO_3$, it is interesting to investigate its photovoltaic response. In fact, photovoltaic effect has been observed in ferroelectrics since 1970s. Different ferroelectric perovskite oxides has been studied, including $Pb(Zr,Ti)O_3$, $BaTiO_3$ and $LiNbO_3$. [121-126] Large open circuit voltage, much larger than the bandgap value, has been reported. [127] In some cases, the photovoltaic responses can be manipulated by the spontaneous polarization. [128, 129] These observations open the door to the application of ferroelectric semiconductors in microelectronic or photoelectric devices. However, the mechanism is not well understood. In the early years, it was suggested that photocurrent in ferroelectrics is due to delocalized band-to-band optical transition in polar crystals due to Franl-Condon relaxation of the excited state. [126] Asymmetric momentum distribution of photo-excited carriers in non-centrosymmetric crystals was also suggested as one of the mechanisms. [130] Another proposed mechanism was the nonlinear property of the dielectrics under UV radiation. [131]

The photovoltaic efficiency of above mentioned ferroelectrics are limited by large bandgap (~3.5 eV) and small current densities. $BiFeO_3$ would be a good candidate in ferroelectric photovoltaic study as it has the largest ferroelectric polarization among the perovksite ferroelectrics. In addition, from the previous bandgap measurement, $BiFeO_3$ has a much smaller bandgap (~2.6 eV). Photovoltaic effects in $BiFeO_3$ single crystal and epitaxial thin films have been reported. [128, 129] S. R. Basu *et al.* reported enhancement of photoresponse of $BiFeO_3$ by tuning the oxidation state of Fe ion with oxygen vacancy concentration. [111] Both contributions from the interface depletion layer and polarization have been observed.

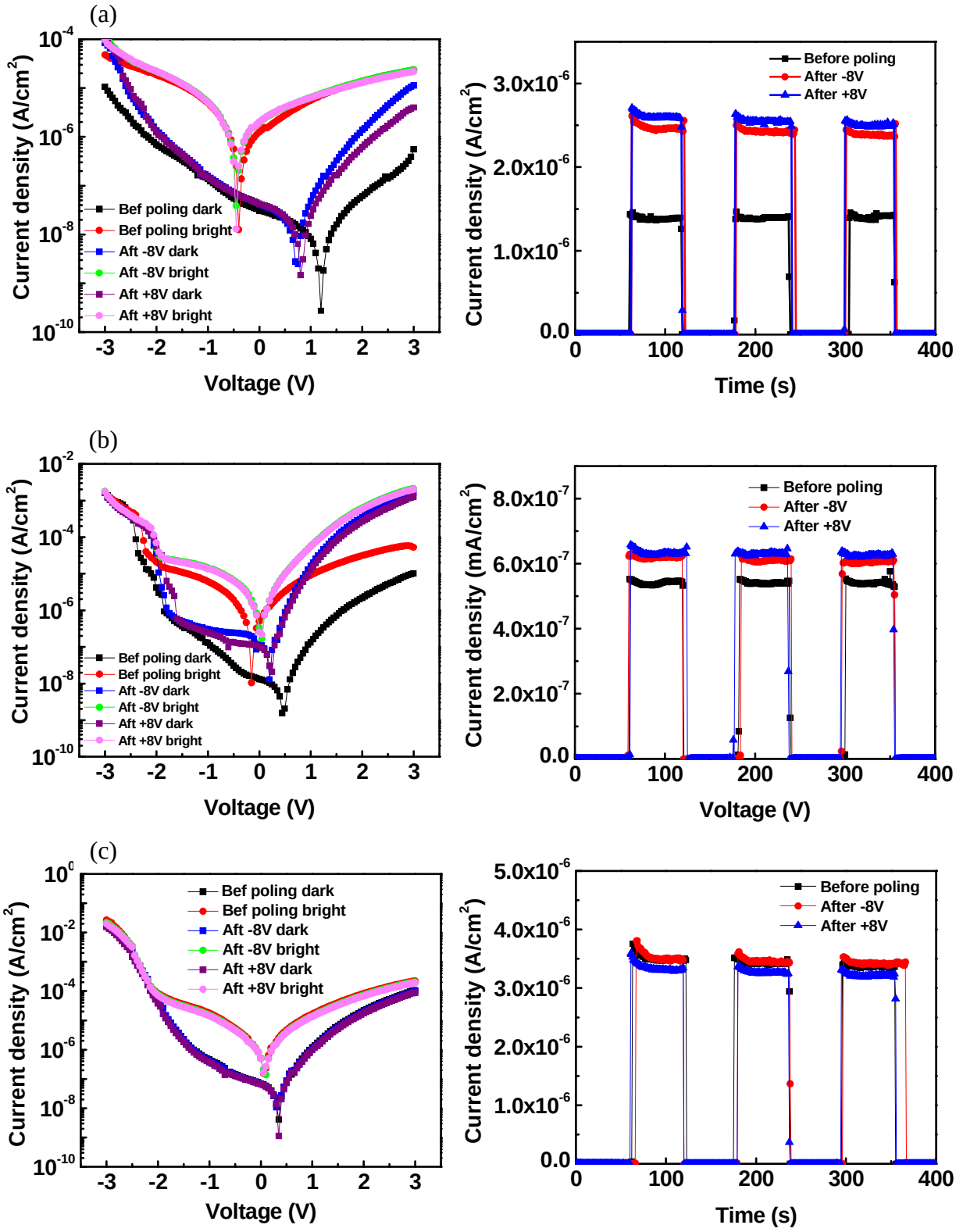

Figure 3.23 (a)-(c) Current density-voltage curves and current density-time of 0%, 5% and 10% La-substituted $BiFeO_3$ samples tested under dark and illuminated conditions.

To examine the photovoltaic effect in $Bi_{(1-x)}La_xFeO_3$ thin films, transparent top electrode, Sb-doped In_2O_3 is prepared using pulsed laser deposition and annealed under oxygen flow at 600 °C. A vertical Sb-doped $In_2O_3/Bi_{(1-x)}LaxFeO_3/SrRuO_3/SrTiO_3$ structure is used for the tests. J-V curves are obtained in dark and under illumination from a Halogen light source (21V, 150 W). We have also tested the change in short-circuit photocurrent densities upon turning on and off the light. Both are shown in Figure 3.23 (a)-(c). The fresh capacitor without poling is first tested and then the polarization is poled up and down followed by J-V measurements (in dark and under illumination). It is observed that polarizing the film leads to some changes in the photovoltaic effect, but subsequent switching of the polarization direction does not generate significant effects.

It has been reported that there are many factors can lead to depletions regions in a ferroelectric semiconductor, such as (i) depolarization field due to incomplete screening of the polarization charge; (ii) Schottky barriers at the electrode/ferroelectric interface due to different work functions; (iii) surface states of the semiconductor or other special factors.[123, 132-134] All of three factors give rise to photovoltaic response. Note that the response generated by depletion regions as the consequence of incomplete screening of the polarization charge can be reversed upon polarization switching. Hence, we can only observe spontaneous polarization dependent photovoltaic responses if the depolarization field is the dominator. The spontaneous polarization, band gap and doping concentration of the ferroelectric semiconductor can affect the width of such depletion regions. In the $Bi_{(1-x)}La_xFeO_3$ thin films that we have studied, it is suggested that the asymmetrical top and bottom interface dominates the photovoltaic response, thus no significant dependence on the polarization direction is observed.

3.4 Theoretical Calculations

First principles calculations are conducted in order to provide theoretical explanation to the experiment observations. This part of the work is done by Dr. Zhang Zhen in collaboration and below details his contribution.

It has been demonstrated that the electrical properties of $BiFeO_3$ are significantly affect by La substitution at the A-sites. Despite many experimental studies including ours, it is striking that no theoretical study has been conducted. In this work, the effects of La substitution on the structure and electronic properties of $BiFeO_3$ are investigated using first-principle density functional theory (DFT) calculations with local spin density approximation (LSDA+U). The structure distortion, chemical bonding and energy bandgap of $Bi_{(1-x)}La_xFeO_3$ are investigated and compared with pure $BiFeO_3$.

The DFT calculations within the projector augmented wave (PAW) method are implemented in the Vienna Ab initio Simulation Package (VASP). The pseudo-potential approach is adopted, where 15 valence electrons for Bi ($5d^{10}6s^26p^3$), 14 for Fe ($3p^63d^64s^2$), and 6 for O ($2s^22p^4$) are treated in the basis. All calculations are performed with an energy cutoff of 500 eV for the plane wave expansion of the PAW, a 3×3×3 Monkhorst Pack grid of k points centred at Γ point, and the Fermi-smearing for the Brillouin zone integrations. To take exchange and correlation effects into consideration, we use the semi-empirical LSDA+U method, where the strong Coulomb repulsion between localized *d* states is treated by adding a Hubbard-like term to the effective potential, leading to a better description of the correlation effect in transition-metal oxide. An effective Hubbard parameter U_{eff} = 3 eV has been determined to be the lower limit of what is required to ensure the insulating character of BFO. In this

study, we use a larger value of U_{eff} = 6 eV (U = 6 eV and J = 0 eV) in the framework of Dudarev's approach.

The 2×2×2 supercell is adopted for all the theoretical calculations in this study, where the unit cell consists of two formula units. The 10-atom unit cell data are taken from X-ray and neutron diffraction structural study on *R3c* $BiFeO_3$ (a = 5.630, α = 59.3°). Rock-salt (G-type) antiferromagetic order is assumed for all supercells. The Fe^{3+} magnetic moments are ferromagnetically coupled within the (111) planes and antiferromagnetically coupled between adjacent planes. The canting of antiferromagnetic sublattices due to the effects of nonlinearity and spin-orbit coupling, and the spiral spin structures with a incommensurate long wavelength of about 600 Å are not discussed in this study, but will be investigated in further research. All structures are relaxed while keeping the lattice parameters fixed until the Hellman-Feynman forces are less than 10^{-2} eV/Å. This value has been found to give good convergence of all quantities under consideration.

The electronic structures are also analyzed using electron localization function (ELF), which helps to visualize the bonding and the Bi^{3+} 6s lone pairs in real space. The ELF is defined as:

$$\mathrm{ELF} = [1 + (D / D_h)^2]^{-1},$$

where

$$D = \frac{1}{2}\sum_i |\nabla\phi_i|^2 - \frac{1}{8}\frac{|\nabla\rho|^2}{\rho} \quad \text{and} \quad D_h = \frac{3}{10}(3\pi^2)^{5/3}\rho^{5/3},$$

where ρ is the electron density, and ϕ_i are the Kohn-Sham wave functions. The ELF provides a measure of the local influence of Pauli repulsion on the behavior of electrons and permits the mapping in real space of core, bonding, and nonbonding regions in a crystal.

A close examination of the calculated local structures indicates that La^{3+} does not stabilize the ferroelectric distortion. Our calculations show that the Bi site is strongly distorted such that only 6 of the 12 oxygen ions surrounding Bi^{3+} can still be considered nearest neighbors in pure *R3c* $BiFeO_3$, similar to previous studies on pure $BiFeO_3$. Three coplanar oxygen ions lie above Bi along [111] at 2.29 Å, and three sit below at 2.50 Å. Two different cation-iron (Bi-Fe) distances (3.05 and 3.88 Å) are observed along the threefold axis, which are the origin of the ferroelectricity in $BiFeO_3$. Contrary to the Bi^{3+} ions, the La^{3+} ion shows a resistance to displacement from its centrosysmetric position along the [111] direction, resulting in a smaller A-Fe distance difference (3.23 Å, and 3.65 Å respectively,). Collectively, La-O bond is lengthened to 2.52 Å, compared to the Bi-O bond of 2.29 Å in pure $BiFeO_3$. Moreover, the difference in bond length between the three short (1.96 Å) and the three long (2.10 Å) Fe-O bonds in $BiFeO_3$ is reduced by La substitution (2.00 Å and 2.05 Å respectively). Therefore, La ion induces only a rather small distortion and the local lattice is more $R\bar{3}c$-like. Correspondingly, the ferroelectricity of $BiFeO_3$ should be weakened by the La doping due to its resistance to off-centre distortions.

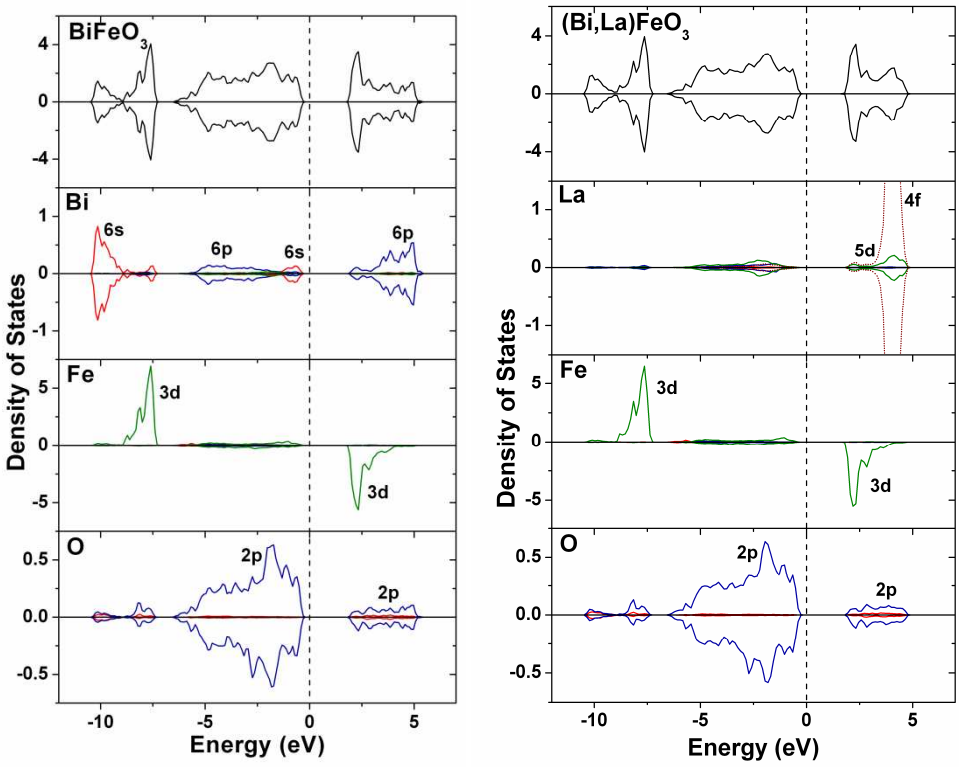

Figure 3.24 Calculated orbital resolved densities of states (DOSs) and partial densities of states (PDOSs) for both spin channels of *R3c* (a) $BiFeO_3$ and (b) La-substituted $BiFeO_3$, using a U_{eff} = 6 eV, where is Fermi level is set to zero.

To understand the resistance to off-center displacement of La^{3+} ion, the orbital resolved densities of states (DOSs) and partial densities of states (PDOSs) are calculated and shown in Figure 3.24. Firstly, covalent Fe-O bonds are identified in both $BiFeO_3$ and La-doped $BiFeO_3$, as our DOS results indicate hybridizations between the Fe *3d* and O *2p* electrons in the whole valence band and conduction band in these compounds. Compared with Fe^{3+} state ions, the Bi *6p* and La *5d/6s/4f* states contribute mainly to the conduction band, as Bi and La are in +3 states, implying the highly ionic nature of Bi and La ions. However, occupied Bi 6s states are present at 10 eV below the Fermi level, which are in the same energy range of O 2p states, indicating Bi-O hybridizations. In comparison, no occupied La^{3+} states are found near the Fermi level, which means that the covalency of La-O bond is weaker than Bi-O bond in bismuth

ferrite. This observation could also be supported if the relative electro-negativities of Bi/La to O are considered. The Δ_{EN} between O and Bi bond is 1.42, while that between O and La bond is 2.34, therefore La-O bond is more ionic than Bi-O bond.

The resistance of La^{3+} ions to off-centre distortion could also be understood by analysis of the ELF plots for $BiFeO_3$ and La-substituted $BiFeO_3$ (Figure 3.25). Consistent with previous calculations on $BiFeO_3$, the ELFs projected on the (111) plane shows maximum value at the oxygen sites and minimum at the Fe and Bi sites. The Bi $6s^2$ lone pair forms a space-filling localized lobe, typical when cation s lone pair electrons overlap with the anion s/p states. The anisotropic nature of the lone pair lobe results in a repulsive interaction with the nearby ions, and cause a movement of Bi^{3+} and Fe^{3+} ions in the [111] direction, which eventually stabilize the ferroelectric distortion in $BiFeO_3$. In contrast, La^{3+} is not ferroelectrically active as it does not have lone-pair lobes. ELF plot indicates that the electrons around the La^{3+} ion are nearly spherically distributed, which are mainly p electrons localized at -13.5 eV below Fermi level (not shown in Fig.1). Based on our DOS and ELF studies, it is concluded that the distortion of lattice along (111) direction could not happen to La^{3+} ions due to the lack of strong covalency bonding between La and O or lobe-like lone pairs localized at La^{3+} ions.

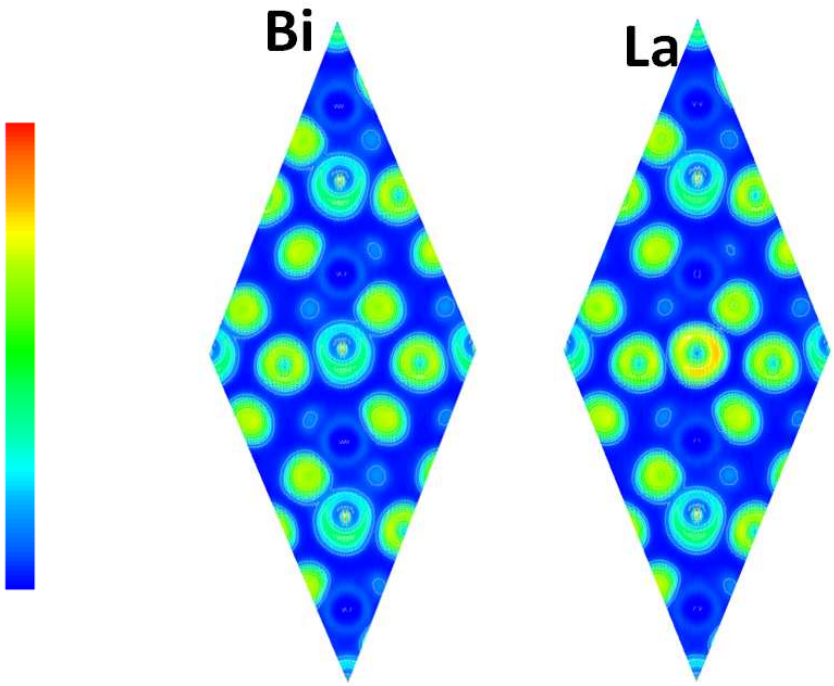

Figure 3.25. Valence ELF plots projected along the (111) direction in pure $BiFeO_3$ and La-substituted $BiFeO_3$. The blue end of the scale indicates no localization, and the red end corresponds to complete localization.

Like for any insulating transition metal oxide, the relation between the minimal energies of p-d and d-d charge-transfer (CT) transitions is of great importance for $BiFeO_3$. In this study, $BiFeO_3$ is calculated to be an CT insulator with a bandgap of 2.52 eV between occupied O *2p* states at the valence band maximum (VBM) and unoccupied Fe *3d* states at the conduction band minimum (CBM). This observation is well supported by the recent experimental and theoretical studies. La substitution narrows the bandgap by 0.03 eV in this calculation. (different from experimental observation) It has been understood that the variation of the transfer interaction of the 3d electron depends on the B-O-B tilting angle in most perovskite oxides, and a tilting angle closer to 180° will lead to broader band dispersion and a narrower band gap. La substitution slightly relieves the buckling of Fe-O-Fe bond angle from 155.1° to therefore a slightly narrower bandgap is identified.

Table 3.2. Calculated LSDA+U structural parameters (O-Fe-O bond angle, Fe-O-Fe bond angle, Fe-O bond length, and A-Fe distance), energetic gap, local magnetic moment of Fe, and the energy difference between AFM and FM ordering.

A-site Cation	$BiFeO_3$	$(Bi, La)FeO_3$
Energy Bandgap (eV)	2.45	2.42
$\Theta_{O\text{-}Fe\text{-}O}$ (deg)	166.4	171.1
$\Theta_{Fe\text{-}O\text{-}Fe}$ (deg)	155.1	155.8
$d_{Fe\text{-}O}$ (Å)	1.96 (2.10)	2.00 (2.05)
$d_{Bi\text{-}Fe}$ (Å)	3.05 (3.88)	3.23 (3.65)

In summary, we have studied the effect of La substitution on the structural and electronic properties of $BiFeO_3$ using DFT calculations. It is found that La^{3+} ions have strong resistance to the off-centre displacement, contrary to Bi^{3+} ions whose distortions along (111) direction result in the ferroelectricity of $BiFeO_3$. This behavior could be understood by density of state and electron localization function studies. It is observed that both the weak covalent bond between La^{3+} and O^{2-} and the absence of lobe-like lone pairs around La^{3+} ions contribute to the absence of displacement of La^{3+} ions.

Therefore, it is theoretically concluded that ferroelectricity is weakened by the La substitution, which is supported by many previous experiments and our own results. Furthermore, our calculations indicate that La substitution decreases the energetic gap in $BiFeO_3$, which is opposite to the experimental observations. There are two reasons that may have caused this discrepancy; (1) the unit cell structure and size are both fixed in the calculation; and (2) the experimentally observed increase in bandgap may be due to elimination of shallow trap states next to the band edges. Further study taking into consideration of the structural change upon La substitution is necessary to clarify this issue and is currently underway.

3.5 Summary

To summarize, we have deposited $Bi_{(1-x)}La_xFeO_3$ thin films using the optimization conditions and studied their structure, electrical and optical properties systematically. We had found that

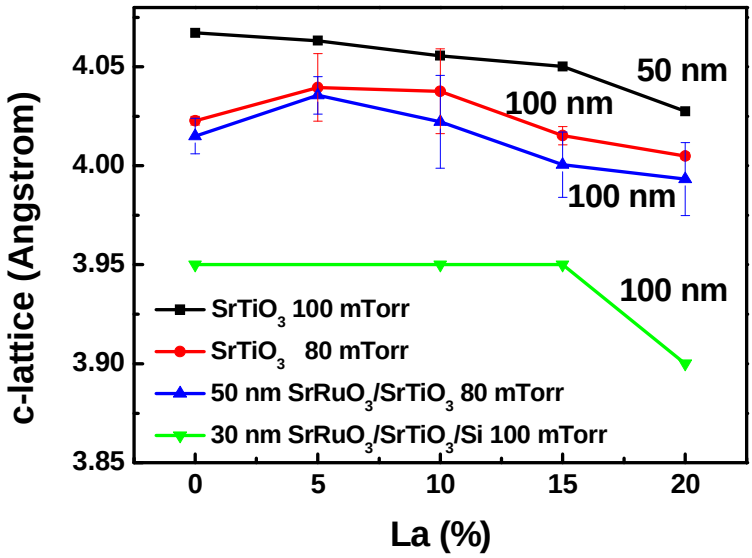

Figure 3.26. Changes of c-lattice as a function of La-substituted $BiFeO_3$ thin films grown on different substrates with different deposition conditions. Data for the La-substituted $BiFeO_3$ thin films grown on 30nm $SrRuO_3/SrTiO_3$/Si at 100 mTorr is adapted from Chu *et al.* [107]

(1) La-substitution induces a structure change in $BiFeO_3$ and the substrate constrain plays a significant role in this process. In Figure 3.26, we summarize the out-of-plane lattice constant of $Bi_{(1-x)}La_xFeO_3$ thin films grown on different substrates as function of La concentration. For films grown directly on $SrTiO_3$ substrates at 100mTorr, the out-of-plane lattices are the largest indicating better coherency at the film/substrate interface. No clear phase transition is observed, likely due to the overwhelming compressive constrain from the substrate. For films grown at 80 mTorr oxygen pressure with/without $SrRuO_3$ electrodes, we observed an increase in the out-of-plane lattice constants at x=0.05 to x=0.10. This observation is repeatable and the error bars, based on measurements from

multiple samples, are shown in Figure 3.26. Then for films grown on $SrRuO_3/SrTiO_3/Si$ at 100mTorr, the substrate compressive strain is the smallest because of the much smaller thermal coefficient of Si. A phase transition was reported to happen at x=0.20. [107] The concentration of La needed to induce the structure change is affected by the constrain from the substrate.

(2) The remanant polarization along (001)c is the largest at x=0.05, which then continuously decreases as x increases. Dielectric constant shows the opposite trend as remanant polarization. The coercive field of $Bi_{(1-x)}La_xFeO_3$ is successfully reduced at x=0.05 and the leakage current is decreased with La substitution. A structure change model as shown in Figure 3.17 is proposed to explain the observations. When La is introduced into $BiFeO_3$, no phase transition is observed but the rhombohedral angle is increased, which leads to the increase of remanant polarization and c-lattice. However, as La concentration increases, the polarization and lattice distortion decreases since La does not possess the stereochemically active $6s^2$ lone pair electrons. However, the piezoelectric coefficient is not improved.

(3) The optical bandgap of $Bi_{(1-x)}La_xFeO_3$ increases with La concentration, consistent with the increase in the resistivity of the films. The switching of ferroelectric polarization does not reverse the photovoltaic response, suggesting depolarization field induced depletion layer is not the main contributor.

(4) First principles calculations also conclude that ferroelectricity is weakened by the La substitution, consistent with our experimental observations. However, smaller bandgap is predicted upon La substitution, which is opposite to the experimental observations. Two possible reasons are suggested, (i) the unit cell structure and size are both fixed in the calculation, which is not the case in

experiments; and (ii) the experimentally observed increase in bandgap may be due to elimination of shallow trap states next to the band edges.

CHAPTER 4

Conclusions and Suggestions

In the course of this study, two promising lead-free ferro/piezoelectric systems, KNN-KNT-$L_{0.03}T$ and $Bi_{1-x}La_xFeO_3$ are studied in thin film form. High quality epitaxial films were deposited on $SrTiO_3$ substrates using PLD. Structure and electric properties of the films were investigated.

The main conclusions can be summarized as follows:

(1) Epitaxial films of KNN-KNT-$L_{0.03}T$ are deposited by PLD using single crystal $SrTiO_3$ as substrate. We were able to study the intrinsic properties of this system along different crystallographic directions. It is suggested that the superior properties of textured bulk ceramics are mainly due to extrinsic contributions.

(2) The challenge of fabricating KNN-KNT-$L_{0.03}T$ films is associated with the fact that alkaline elements are volatile. It is very difficult to control the film composition precisely. Furthermore, it is not possible to confirm the film composition accurately with current technologies. For a complex system such as KNN-KNT-$L_{0.03}T$, its properties would certainly be affected by variation in composition resulting from the high temperature growth process. Thus, it is desirable to have a simpler lead-free system which is easier process and study. Therefore, a simpler lead-free ferro/piezoelectric, $BiFeO_3$–based system is suggested.

(3) La-substitution induces a structure change in $BiFeO_3$ and the substrate constrain plays a significant role in this process. In Figure 3.22, we summarize

the out-of-plane lattice constant of $Bi_{(1-x)}La_xFeO_3$ thin films grown on different substrates as function of La concentration. For films grown directly on $SrTiO_3$ substrates at 100mTorr, the out-of-plane lattices are the largest indicating better coherency at the film/substrate interface. No clear phase transition is observed, likely due to the overwhelming compressive constrain from the substrate. For films grown at 80 mTorr oxygen pressure with/without $SrRuO_3$ electrodes, we observed an increase in the out-of-plane lattice constants at x=0.05 to x=0.10. This observation is repeatable and the error bars, based on measurements from multiple samples, are shown in Figure 3.26. Then for films grown on $SrRuO_3/SrTiO_3/Si$ at 100mTorr, the substrate compressive strain is the smallest because of the much smaller thermal coefficient of Si. A phase transition was reported to happen at x=0.20. [107] The concentration of La needed to induce the phase transition is affected by the constrain from the substrate.

(4) The remanant polarization along (001)c is the largest at x=0.05, which then continuously decreases as x increases. Dielectric constant shows the opposite trend as remanant polarization. The coercive field of $Bi_{(1-x)}La_xFeO_3$ is successfully reduced at x=0.05 and the leakage current is decreased with La substitution. A structure transition model as shown in Figure 3.17 is proposed to explain the observations. When La is introduced into $BiFeO_3$, the rhombohedral angle is increased, which leads to the increase of remanant polarization and c-lattice. However, as La concentration increases, the polarization and lattice distortion decreases since La does not possess the stereochemically active $6s^2$ lone pair electrons. However, the piezoelectric coefficient is not improved.

(5) The optical bandgap of $Bi_{(1-x)}La_xFeO_3$ increases with La concentration, consistent with the increase in the resistivity of the films. The switching of ferroelectric polarization does not reverse the photovoltaic response, suggesting depolarization field induced depletion layer is not the main contributor.

(6) First principles calculations also conclude that ferroelectricity is weakened by the La substitution, consistent with our experimental observations. However, smaller bandgap is predicted upon La substitution, which is opposite to the experimental observations. Two possible reasons are suggested, (i) the unit cell structure and size are both fixed in the calculation, which is not the case in experiments; and (ii) the experimentally observed increase in bandgap may be due to elimination of shallow trap states next to the band edges

For the future work, we suggest the following direction:

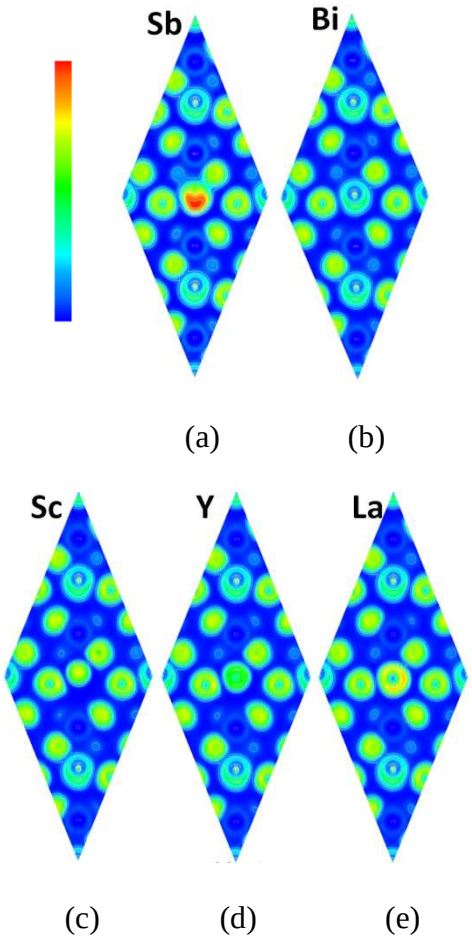

Figure 4.1. Valence ELF plots projected along the polar [111] axis ((1 1 -2) plane) in (a) pure $BiFeO_3$, (b) Sb, (c) Sc, (d) Y, and (e) La-substituted $BiFeO_3$. The vertical middle axis indicates the order of Bi-Fe-Bi-Fe-Sb(Bi)-Fe-Bi-Fe-Bi. The blue end of the scale indicates no localization, and the red end corresponds to complete localization. Figures adapted from Zhang *et al*. [135]

In order to obtain enhanced dielectric and piezoelectric responses in the $BiFeO_3$-based system, it is important to choose an end member that is (i) electrical active (antiferroelectric or ferroelectric) and (ii) can induce a phase transition in the solid solution system. According to Zhang *et al*., the Sc and Y elements, which have similar atomic configuration with La, could lead to more significant ferroelectric distortion than La based on first principles calculations. This off-centre displacement is attributable to the fact that Sc^{3+} and Y^{3+} have smaller ionic size and larger electro-

negativity than La^{3+} , leading to stronger Sc *3d*-O *2p* and Y *4d*-O *2p* hybridization. He also found that the A-site substitute, Sb^{3+} shows off-centre distortion and stabilized by s^2 electron lone pair. It is also calculated that the strong Sb-O hybridizations leads to a greater stereochemical activity of the Sb lone pair than that of Bi lone pair, giving rise to a larger ferroelectric distortion of Sb along the [111] direction. Therefore, such elements could be explored in the future.

Appendix A

Principles of Piezoelectric Force Microscopy

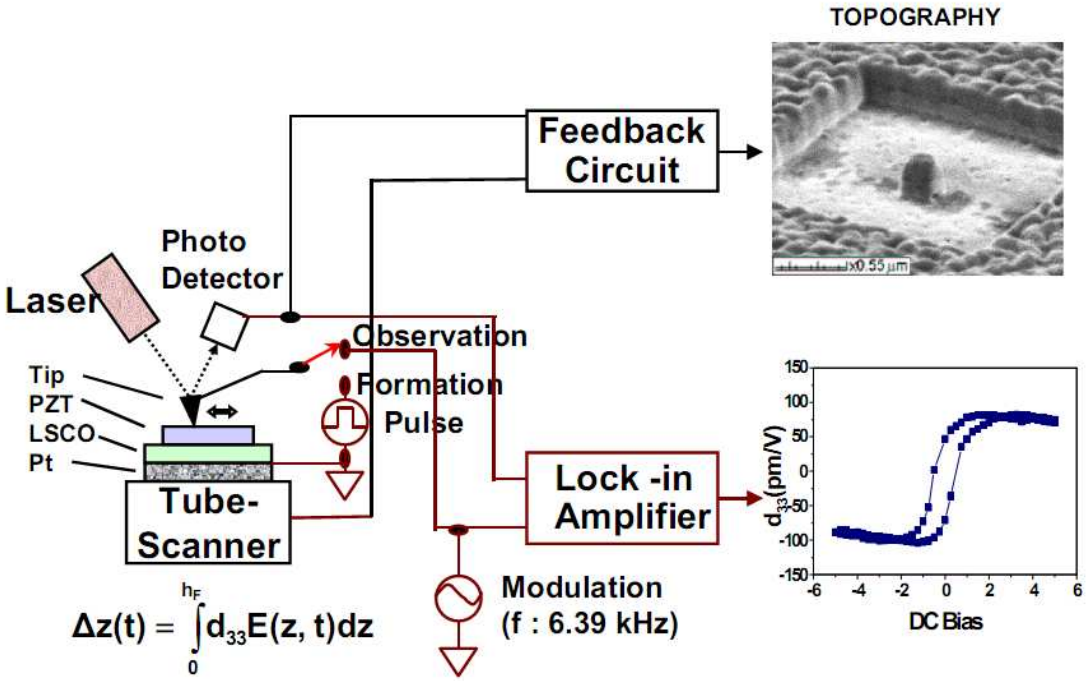

Figure A.1. Schematic illustration of the PFM setup. Figure adapted from Chandran S. G.[136]

Piezoelectric property characterizations, the d_{33} measurement and ferroelectric domain imaging are performed using atomic force microscope (AFM). This technique has been used to characterize ferroelectric thin films by many groups.[40, 137-139] The system uses an AFM tip to detect the vibration of a ferroelectric sample, which is induced by an ac voltage. Figure A.1 describes schematically the typical system set up. A voltage at frequency ω is applied through the conducting tip, which causes the sample area under the electric field to vibrate at the same frequency due to the

converse piezoelectric effect. This vibration then forces the AFM tip to oscillate, and the modulated deflection signal is detected using the lock-in amplifier. The outputs from the lock-in amplifier (internal or external) can be displayed quantitatively (d_{33}) or qualitatively (domain imaging).

In the imaging mode, the conducting tip is placed directly on the sample surface. An electric field is generated underneath the tip and excites local response. The response reveals local domain orientation information. By scanning the tip along the sample surface, domain configurations of the sample can be mapped out. The resolution of the domain features depends on the sharpness of the tip.

In the quantitative (or d_{33}) mode, the voltage is usually applied through the tip to a Pt top electrode prepared by normal photolithography method. This is to ensure a homogenous electric field under the electrode. It also prevents the buildup of charges underneath the tip and minimizes the electrostatic interaction between the cantilever and the sample. Usually, the frequency of the AC field applied through the tip is lower than the resonant frequency for quantitative d_{33} measurement. This is to avoid mechanical resonance of the cantilever, which may leads to exaggeration of the d_{33} value. We use heavily doped silicon tips, which were coated with a layer of Pt/Ir alloy for the measurements. The measurement frequency used is 10 kHz.

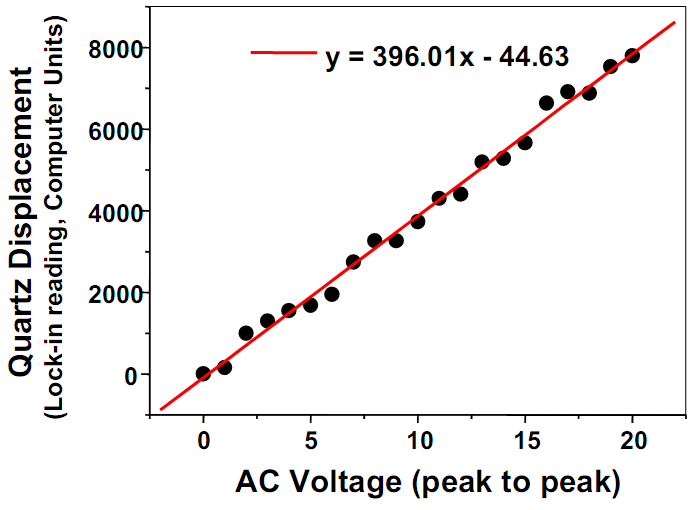

Figure A.2. Calibration of piezoelectric response using a quartz sample. Figure adapted from Chandran S. G.

To calibrate the output signal from the photodiode, we used x-cut quartz crystal coated Au electrodes on both sides. The crystal is driven from 0 to 20 V (peak-to-peak) and the displacement of the tip is recorded. The result is shown in Figure A.2. The slope of the linear displacement vs. voltage plot is equal to the d_{33} of quartz, i.e., 2.3 pm/V.[140] This approach has been used by many groups, and the results are consistent [136]and reliable.

Reference

1. Reutte, B., MS Thesis, Virginia Tech, 2003.
2. Li, H., Ph. D Thesis, University of Maryland, College Park, 2001.
3. B., J., C. WR, and J. H., *Piezoelectric Ceramics.* Academic press, London, 1971: p. 131.
4. Noheda, B., et al., *A monoclinic ferroelectric phase in the Pb(Zr1-xTix)O-3 solid solution.* Applied Physics Letters, 1999. **74**(14): p. 2059-2061.
5. Du, X.H., et al., *Crystal orientation dependence of piezoelectric properties of lead zirconate titanate near the morphotropic phase boundary.* Applied Physics Letters, 1998. **72**(19): p. 2421-2423.
6. Izyumskaya, N., et al., *Processing, structure, properties, and applications of PZT thin films.* Critical Reviews in Solid State and Materials Sciences, 2007. **32**(3-4): p. 111-202.
7. Jaffe, B., R.S. Roth, and S. Marzullo, *Properties of Piezoelectric Ceramics in the Solid-solution Series Lead Titanate-Lead Zirconate-Lead Oxide: Tin Oxide and Lead titanate-Lead Hafnate.* J. Res. Natl. Bur. Stand, 1955.
8. Noheda, B., *Structure and high-piezoelectricity in lead oxide solid solutions.* Current Opinion in Solid State & Materials Science, 2002. **6**(1): p. 27-34.
9. Scott, J.F., in *Ferroelectric Memories*. 2000, Springer: Berlin.
10. Uchino, K., in *Ferroelectric devices*. 2000, Marcel Dekker: New York.
11. Busch-Vishniac, I.J., *Trends in electromechanical transduction.* Physics Today, 1998. **51**(7): p. 28-34.
12. Cross, E., *Materials science - Lead-free at last.* Nature, 2004. **432**(7013): p. 24-25.
13. Cohen, R.E., *ORIGIN OF FERROELECTRICITY IN PEROVSKITE OXIDES.* Nature, 1992. **358**(6382): p. 136-138.
14. Guo, R., et al., *Origin of the high piezoelectric response in PbZr1-xTixO3.* Physical Review Letters, 2000. **84**(23): p. 5423-5426.
15. Egerton, L. and D.M. Dillon, *PIEZOELECTRIC AND DIELECTRIC PROPERTIES OF CERAMICS IN THE SYSTEM POTASSIUM SODIUM NIOBATE.* Journal of the American Ceramic Society, 1959. **42**(9): p. 438-442.
16. Jaeger, R.E. and L. Egerton, *HOT PRESSING OF POTASSIUM-SODIUM NIOBATES.* Journal of the American Ceramic Society, 1962. **45**(5): p. 209-213.
17. Guo, Y.P., K. Kakimoto, and H. Ohsato. *Structure and electrical properties of lead-free (Na0.5K0.5)Nbo(3)-BaTiO3 ceramics*. in *21st Meeting on Ferroelectric Materials and Their Applications (FMA-21)*. 2004. Kyoto, JAPAN: Inst Pure Applied Physics.
18. Guo, Y.P., K. Kakimoto, and H. Ohsato, *Dielectric and piezoelectric properties of lead-free (Na0.5K0.5)NbO3-SrTiO3 ceramics.* Solid State Communications, 2004. **129**(5): p. 279-284.
19. Guo, Y., K.-i. Kakimoto, and H. Ohsato, *Phase transitional behavior and piezoelectric properties of (Na[sub 0.5]K[sub 0.5])NbO[sub 3]--LiNbO[sub 3] ceramics.* Applied Physics Letters, 2004. **85**(18): p. 4121-4123.
20. Matsubara, M., et al., *Synthesis and characterization of (K0.5Na0.5)(Nb0.7Ta0.3)O-3 piezoelectric ceramics sintered with sintering aid K5.4Cu1.3Ta10O29.* Japanese Journal of Applied Physics Part 1-Regular Papers Brief Communications & Review Papers, 2005. **44**(9A): p. 6618-6623.

21. Saito, Y., et al., *Lead-free piezoceramics.* Nature, 2004. **432**(7013): p. 84-87.
22. Saito, Y. and H. Takao. *High performance lead-free piezoelectric ceramics in the (K,Na)NbO3-LiTaO3 solid solution system*. in *11th International Meeting on Ferroelectricity (IMF-11)*. 2005. Iguassu Falls, BRAZIL: Taylor & Francis Ltd.
23. Spaldin, N.A. and M. Fiebig, *The renaissance of magnetoelectric multiferroics.* Science, 2005. **309**(5733): p. 391-392.
24. Zhao, T., et al., *Electrical control of antiferromagnetic domains in multiferroic BiFeO3 films at room temperature.* Nature Materials, 2006. **5**(10): p. 823-829.
25. Uchida, H., et al., *Crystal structure and ferroelectric properties of rare-earth substituted BiFeO3 thin films.* Journal of Applied Physics, 2006. **100**(1): p. 9.
26. Kubel, F. and H. Schmid, *STRUCTURE OF A FERROELECTRIC AND FERROELASTIC MONODOMAIN CRYSTAL OF THE PEROVSKITE BIFEO3.* Acta Crystallographica Section B-Structural Science, 1990. **46**: p. 698-702.
27. Michel, C., et al., *ATOMIC STRUCTURE OF BIFEO3.* Solid State Communications, 1969. **7**(9): p. 701-&.
28. Kiselev, S.V., R.P. Ozerov, and G.S. Zhdanov, Sov. Phys. Dokl. , 1963. **7**(742).
29. Sosnowska, I., T. Peterlinneumaier, and E. Steichele, *SPIRAL MAGNETIC-ORDERING IN BISMUTH FERRITE.* Journal of Physics C-Solid State Physics, 1982. **15**(23): p. 4835-4846.
30. Teague, J.R., R. Gerson, and W.J. James, *DIELECTRIC HYSTERESIS IN SINGLE CRYSTAL BIFEO3.* Solid State Communications, 1970. **8**(13): p. 1073-&.
31. Wang, J., et al., *Epitaxial BiFeO3 multiferroic thin film heterostructures.* Science, 2003. **299**(5613): p. 1719-1722.
32. Yun, K.Y., et al., *Enhancement of electrical properties in polycrystalline BiFeO3 thin films.* Applied Physics Letters, 2006. **89**(19): p. 3.
33. Shvartsman, V.V., et al., *Large bulk polarization and regular domain structure in ceramic BiFeO3.* Applied Physics Letters, 2007. **90**(17): p. 3.
34. Lebeugle, D., et al., *Room-temperature coexistence of large electric polarization and magnetic order in BiFeO3 single crystals.* Physical Review B, 2007. **76**(2): p. 8.
35. Singh, S.K. and H. Ishiwara, *Reduced leakage current in BiFeO3 thin films on Si substrates formed by a chemical solution method.* Japanese Journal of Applied Physics Part 2-Letters & Express Letters, 2005. **44**(20-23): p. L734-L736.
36. Martin, L.W., et al., *Nanoscale control of exchange bias with BiFeO3 thin films.* Nano Letters, 2008. **8**(7): p. 2050-2055.
37. Palkar, V.R., J. John, and R. Pinto, *Observation of saturated polarization and dielectric anomaly in magnetoelectric BiFeO3 thin films.* Applied Physics Letters, 2002. **80**(9): p. 1628-1630.
38. Wang, Y.P., et al., *Room-temperature saturated ferroelectric polarization in BiFeO3 ceramics synthesized by rapid liquid phase sintering.* Applied Physics Letters, 2004. **84**(10): p. 1731-1733.
39. Eerenstein, W., et al., *Experimental difficulties and artefacts in multiferroic and magnetoelectric thin films of BiFeO3, Bi0.6Tb0.3La0.1FeO3 and BiMnO3.* Philosophical Magazine Letters, 2007. **87**(3-4): p. 249-257.

40. Nagarajan, V., et al., *Realizing intrinsic piezoresponse in epitaxial submicron lead zirconate titanate capacitors on Si.* Applied Physics Letters, 2002. **81**(22): p. 4215-4217.
41. Cheng, Z.X., et al., *Enhanced electrical polarization and ferromagnetic moment in a multiferroic BiFeO3/Bi3.25Sm0.75Ti2.98V0.02O12 double-layered thin film.* Applied Physics Letters, 2006. **88**(13): p. 3.
42. Huang, F.Z., et al., *Multiferroic properties and dielectric relaxation of BiFeO3/Bi3.25La0.75Ti3O12 double-layered thin films.* Applied Physics Letters, 2007. **90**(25): p. 3.
43. Kumar, M.M., A. Srinivas, and S.V. Suryanarayana, *Structure property relations in BiFeO3/BaTiO3 solid solutions.* Journal of Applied Physics, 2000. **87**(2): p. 855-862.
44. Cheng, J.R., N. Li, and L.E. Cross, *Structural and dielectric properties of Ga-modified BiFeO3-PbTiO3 crystalline solutions.* Journal of Applied Physics, 2003. **94**(8): p. 5153-5157.
45. Smith, R.T., et al., *DIELECTRIC PROPERTIES OF SOLID SOLUTIONS OF BIFEO3 WITH PB(TI,ZR)O3 AT HIGH TEMPERATURE.* Journal of Applied Physics, 1968. **39**(1): p. 70-&.
46. Singh, S.K. and H. Ishiwara. *Doping effect of rare-earth ions on electrical properties of BiFeO3 thin films fabricated by chemical solution deposition*. in *International Conference on Solid State Devices and Materials (*2005. Kobe, JAPAN: Inst Pure Applied Physics.
47. Singh, S.K., K. Maruyama, and H. Ishiwara, *Reduced leakage current in La and Ni codoped BiFeO3 thin films.* Applied Physics Letters, 2007. **91**(11): p. 3.
48. Singh, S.K., K. Maruyama, and H. Ishiwara, *The influence of La-substitution on the micro-structure and ferroelectric properties of chemical-solution-deposited BiFeO3 thin films.* Journal of Physics D-Applied Physics, 2007. **40**(9): p. 2705-2709.
49. Lee, C.C. and J.M. Wu, *Studies on leakage mechanisms and electrical properties of doped BiFeO3 films.* Electrochemical and Solid State Letters, 2007. **10**(8): p. G58-G61.
50. Uchida, H., et al., *Ion modification for improvement of insulating and ferroelectric properties of BiFeO3 thin films fabricated by chemical solution deposition.* Japanese Journal of Applied Physics Part 2-Letters & Express Letters, 2005. **44**(16-19): p. L561-L563.
51. Lee, D., et al., *Epitaxially grown La-modified BiFeO[sub 3] magnetoferroelectric thin films.* Applied Physics Letters, 2005. **86**(22): p. 222903-3.
52. Lee, Y.-H., J.-M. Wu, and C.-H. Lai, *Influence of La doping in multiferroic properties of BiFeO[sub 3] thin films.* Applied Physics Letters, 2006. **88**(4): p. 042903-3.
53. Lee, Y.H., et al., *Epitaxial growth of the La-substituted BiFeO3 thin films.* Electrochemical and Solid State Letters, 2006. **9**(5): p. F38-F40.
54. Das, S.R., et al., *Effect of La substitution on structural and electrical properties of BiFeO3 thin film.* Journal of Applied Physics, 2006. **99**(6): p. 3.
55. Gao, F., et al., *Preparation of la-doped BiFeO3 thin films with Fe2+ ions on Si substrates.* Journal of Applied Physics, 2006. **99**(9): p. 4.
56. Chu, Y.H., et al., *Low voltage performance of epitaxial BiFeO3 films on Si substrates through lanthanum substitution.* Applied Physics Letters, 2008. **92**(10): p. 3.

57. Simões, A.Z., et al., *Improvement of fatigue resistance on La modified BiFeO3 thin films.* Current Applied Physics, 2009. **9**(2): p. 520-523.
58. Simoes, A.Z., et al., *Piezoelectric behavior of SrRuO[sub 3] buffered lanthanum modified bismuth ferrite thin films grown by chemical method.* Applied Physics Letters, 2008. **93**(14): p. 142902-3.
59. Li, Y.W., et al., *Oxygen-vacancy-related dielectric relaxation in BiFeO3 films grown by pulsed laser deposition.* Journal of Physics D-Applied Physics, 2008. **41**(21): p. 4.
60. Prashanthi, K., et al., *Enhancement in multiferroic properties of Bi0.7-xLaxDy0.3FeO3 system with removal of La.* Solid State Communications, 2009. **149**(5-6): p. 188-191.
61. Wang, Y., et al., *Charged defects and their effects on electrical behavior in Bi(1-x)LaxFeO(3) thin films.* Journal of Applied Physics, 2009. **105**(1): p. 3.
62. Yan, Z., et al., *Processing and properties of Yb-doped BiFeO[sub 3] ceramics.* Applied Physics Letters, 2007. **91**(8): p. 082906-3.
63. Huang, F., et al., *Effect of Nd dopant on magnetic and electric properties of BiFeO[sub 3] thin films prepared by metal organic deposition method.* Applied Physics Letters, 2006. **89**(24): p. 242914-3.
64. Hu, Z.Q., et al., *Enhanced multiferroic properties of BiFeO3 thin films by Nd and high-valence Mo co-doping.* Journal of Physics D-Applied Physics, 2009. **42**(18): p. 5.
65. Wang, Y. and C.W. Nan, *Effect of Tb doping on electric and magnetic behavior of BiFeO3 thin films.* Journal of Applied Physics, 2008. **103**(2): p. 5.
66. Fujino, S., et al., *Combinatorial discovery of a lead-free morphotropic phase boundary in a thin-film piezoelectric perovskite.* Applied Physics Letters, 2008. **92**(20): p. 202904-3.
67. Singh, S.K., H. Ishiwara, and K. Maruyama, *Room temperature ferroelectric properties of Mn-substituted BiFeO3 thin films deposited on Pt electrodes using chemical solution deposition.* Applied Physics Letters, 2006. **88**(26): p. 3.
68. Kim, J.K., et al., *Enhanced ferroelectric properties of Cr-doped BiFeO3 thin films grown by chemical solution deposition.* Applied Physics Letters, 2006. **88**(13): p. 3.
69. Kim, D.H., et al., *Large ferroelectric polarization in antiferromagnetic BiFe0.5Cr0.5O3 epitaxial films.* Applied Physics Letters, 2007. **91**(4): p. 3.
70. Lee, S.U., et al., *Electrical properties of Cr-doped BiFeO3 thin films fabricated on the p-type Si(100) substrate by chemical solution deposition.* Journal of Applied Physics, 2007. **102**(4): p. 5.
71. Khomchenko, V.A., et al., *Effect of diamagnetic Ca, Sr, Pb, and Ba substitution on the crystal structure and multiferroic properties of the BiFeO3 perovskite.* Journal of Applied Physics, 2008. **103**(2): p. 6.
72. Qi, X.D., et al., *Greatly reduced leakage current and conduction mechanism in aliovalent-ion-doped BiFeO3.* Applied Physics Letters, 2005. **86**(6): p. 3.
73. Yu, B.F., et al., *Enhanced multiferroic properties of the high-valence Pr doped BiFeO3 thin film.* Applied Physics Letters, 2008. **93**(18): p. 3.
74. Cheng, Z.X., et al., *La and Nb codoped BiFeO[sub 3] multiferroic thin films on LaNiO[sub 3]/Si and IrO[sub 2]/Si substrates.* Applied Physics Letters, 2008. **92**(9): p. 092902-3.
75. Singh, S.K., et al. *Bottom electrodes dependence of ferroelectric properties in epitaxial BiFeO3/SrRuO3/SrTiO3 structures*. in *18th International Symposium on Integrated Ferroelectrics*. 2006. Honolulu, HI: Taylor & Francis Ltd.

76. Zheng, R.Y., et al., *Effects of SRO Buffer Layer on Multiferroic BiFeO3 Thin Films.* Journal of the American Ceramic Society, 2008. **91**(10): p. 3240-3244.
77. Fujino, S., Ph. D Thesis, University of Maryland, College Park, 2008.
78. Koinuma, H. and I. Takeuchi, *Combinatorial solid-state chemistry of inorganic materials.* Nat Mater, 2004. **3**(7): p. 429-438.
79. Chen, Y.P., et al., *Study on ferroelectric and dielectric properties of La-doped SrBi4Ti4O15 ceramics.* Materials Letters, 2003. **57**(22-23): p. 3623-3628.
80. Simoes, A.Z., et al., *Ferroelectric fatigue endurance of Bi4-xLaxTi3O12 thin films explained in terms of x-ray photoelectron spectroscopy.* Journal of Applied Physics, 2007. **101**(8): p. 6.
81. Yao, Y.Y., et al., *Doping effect on the dielectric property in bismuth titanate.* Journal of Applied Physics, 2004. **95**(6): p. 3126-3130.
82. Singh, V.R., A. Garg, and D.C. Agrawal, *Structural changes in chemical solution deposited lanthanum doped bismuth ferrite thin films.* Applied Physics Letters, 2008. **92**(15): p. 152905-3.
83. Polomska, M., Kaczmare.W, and Z. Pajak, *ELECTRIC AND MAGNETIC-PROPERTIES OF (B1-XLAX)FEO3 SOLID-SOLUTIONS.* Physica Status Solidi a-Applied Research, 1974. **23**(2): p. 567-574.
84. Zhang, S.-T., et al., *Substitution-induced phase transition and enhanced multiferroic properties of Bi[sub 1 - x]La[sub x]FeO[sub 3] ceramics.* Applied Physics Letters, 2006. **88**(16): p. 162901-3.
85. Zhang, S.T., et al., *Preparation, structures, and multiferroic properties of single phase Bi1-xLaxFeO3 (x=0-0.40) ceramics.* Journal of Applied Physics, 2006. **100**(11): p. 6.
86. Yuan, G.L., et al., *Multiferroic properties of single-phase Bi0.85La0.15FeO3 lead-free ceramics.* Journal of the American Ceramic Society, 2006. **89**(10): p. 3136-3139.
87. Zalesskii, A.V., et al., *Composition-induced transition of spin-modulated structure into a uniform antiferromagnetic state in a Bi1-xLaxFeO3 system studied using Fe-57 NMR.* Physics of the Solid State, 2003. **45**(1): p. 141-145.
88. Lin, Y.-H., et al., *Enhancement of ferromagnetic properties in BiFeO[sub 3] polycrystalline ceramic by La doping.* Applied Physics Letters, 2007. **90**(17): p. 172507-3.
89. Cheng, Z.X., et al. *Structure, ferroelectric properties, and magnetic properties of the La-doped bismuth ferrite*. in *52nd Annual Conference on Magnetism and Magnetic Materials*. 2007. Tampa, FL: Amer Inst Physics.
90. Kalinin, S.V., et al., *Intrinsic single-domain switching in ferroelectric materials on a nearly ideal surface.* Proceedings of the National Academy of Sciences, 2007. **104**(51): p. 20204-20209.
91. Simoes, A.Z., et al., *Improvement of fatigue resistance on La modified BiFeO3 thin films.* Current Applied Physics, 2009. **9**(2): p. 520-523.
92. Shannon, R.R., *Acta Crystallogr Sec A: Cryst. Phys. Diffr. Theor. Gen. Crystallogr.* . 32, 1976. **751**.
93. Junling, W., Ph. D Thesis, University of Maryland, College Park, 2005.
94. Jackson, T.J. and S.B. Palmer, *OXIDE SUPERCONDUCTOR AND MAGNETIC METAL THIN-FILM DEPOSITION BY PULSED-LASER ABLATION - A REVIEW.* Journal of Physics D-Applied Physics, 1994. **27**(8): p. 1581-1594.
95. Hall, D.A., *Review nonlinearity in piezoelectric ceramics.* Journal of Materials Science, 2001. **36**(19): p. 4575-4601.

96. Fujino, S., et al., *Combinatorial discovery of a lead-free morphotropic phase boundary in a thin-film piezoelectric perovskite.* Applied Physics Letters, 2008. **92**(20).
97. Chu, Y.H., et al., *Controlling magnetism with multiferroics.* Materials Today, 2007. **10**(10): p. 16-23.
98. Jang, H.W., et al., *Domain Engineering for Enhanced Ferroelectric Properties of Epitaxial (001) BiFeO Thin Films.* Advanced Materials, 2009. **21**(7): p. 817-+.
99. Bea, H., et al., *Investigation on the origin of the magnetic moment of BiFeO3 thin films by advanced X-ray characterizations.* Physical Review B, 2006. **74**(2).
100. You, L., et al., *Influence of oxygen pressure on the ferroelectric properties of epitaxial BiFeO[sub 3] thin films by pulsed laser deposition.* Physical Review B (Condensed Matter and Materials Physics), 2009. **80**(2): p. 024105-5.
101. Go, H., et al., *Effect of oxygen annealing on ferroelectricity of BiFeO3 thin films formed by pulsed laser deposition.* Japanese Journal of Applied Physics Part 1-Regular Papers Brief Communications & Review Papers, 2007. **46**(6A): p. 3491-3494.
102. Chu, Y.H., et al., *Ferroelectric size effects in multiferroic BiFeO3 thin films.* Applied Physics Letters, 2007. **90**(25).
103. Pabst, G.W., et al., *Leakage mechanisms in BiFeO3 thin films.* Applied Physics Letters, 2007. **90**(7).
104. Qi, X.D., et al., *Greatly reduced leakage current and conduction mechanism in aliovalent-ion-doped BiFeO3.* Applied Physics Letters, 2005. **86**(6).
105. Lee, S.U., et al., *Electrical properties of Cr-doped BiFeO3 thin films fabricated on the p-type Si(100) substrate by chemical solution deposition.* Journal of Applied Physics, 2007. **102**(4).
106. Li, Y.B., et al., *Multiferroic properties of sputtered BiFeO3 thin films.* Applied Physics Letters, 2008. **92**(13).
107. Chu, Y.H., et al., *Low voltage performance of epitaxial BiFeO3 films on Si substrates through lanthanum substitution.* Applied Physics Letters, 2008. **92**(10).
108. Wang, Y., et al., *Charged defects and their effects on electrical behavior in Bi(1-x)LaxFeO(3) thin films.* Journal of Applied Physics, 2009. **105**(1).
109. Kerr, J.A. and D.W. Stocker, *Handbook of Chemistry and Physics*. 83 ed. 2002: CRC Press LLC.
110. Hauser, A.J., et al., *Characterization of electronic structure and defect states of thin epitaxial BiFeO3 films by UV-visible absorption and cathodoluminescence spectroscopies.* Applied Physics Letters, 2008. **92**(22).
111. Basu, S.R., et al., *Photoconductivity in BiFeO3 thin films.* Applied Physics Letters, 2008. **92**(9).
112. Kumar, A., et al., *Linear and nonlinear optical properties of BiFeO3.* Applied Physics Letters, 2008. **92**(12).
113. Gao, F., et al., *Preparation and photoabsorption characterization of BiFeO3 nanowires.* Applied Physics Letters, 2006. **89**(10).
114. Kanai, T., S. Ohkoshi, and K. Hashimoto, *Magnetic, electric, and optical functionalities of (PLZT)(x)(BiFeO3)(1-x) ferroelectric-ferromagnetic thin films.* Journal of Physics and Chemistry of Solids, 2003. **64**(3): p. 391-397.

115. Gujar, T.P., V.R. Shinde, and C.D. Lokhande, *Nanocrystalline and highly resistive bismuth ferric oxide thin films by a simple chemical method.* Materials Chemistry and Physics, 2007. **103**(1): p. 142-146.
116. Fruth, V., et al. *Preparation and characterization of BiFeO3 ceramic*. in *International Conference on Perovskites Properties and Potential Applications*. 2007. Dubendorf, SWITZERLAND.
117. Neaton, J.B., et al., *First-principles study of spontaneous polarization in multiferroic BiFeO3.* Physical Review B, 2005. **71**(1).
118. Clark, S.J. and J. Robertson, *Band gap and Schottky barrier heights of multiferroic BiFeO3.* Applied Physics Letters, 2007. **90**(13).
119. Rosencher, E., *Optoelectronics*. 2002.
120. Pankove, J.I., *Optical Processess in Semiconductors*. 1971, Dover.
121. Ichiki, M., et al., *Photovoltaic effect of crystalline-oriented lead lanthanum zirconate titanate in layered film structure.* Japanese Journal of Applied Physics Part 1-Regular Papers Brief Communications & Review Papers, 2006. **45**(12): p. 9115-9118.
122. Qin, M., K. Yao, and Y.C. Liang, *High efficient photovoltaics in nanoscaled ferroelectric thin films.* Applied Physics Letters, 2008. **93**(12).
123. Qin, M., K. Yao, and Y.C. Liang, *Photovoltaic mechanisms in ferroelectric thin films with the effects of the electrodes and interfaces.* Applied Physics Letters, 2009. **95**(2).
124. Kim, S.R., S.K. Choi, and H.M. Lee, *Non-steady-state photovoltaic current in (Pb0.85La0.15)TiO3 and BaTiO3 ceramics.* Journal of Materials Research, 2000. **15**(6): p. 1354-1357.
125. Nakamura, M., et al., *Photovoltaic effect and photoconductivity in Sc-doped near-stoichiometric LiNbO3 crystals.* Optical Materials, 2008. **31**(2): p. 280-283.
126. Glass, A.M., D.V.D. Linde, and T.J. Negran, *HIGH-VOLTAGE BULK PHOTOVOLTAIC EFFECT AND PHOTOREFRACTIVE PROCESS INLINBO3.* Applied Physics Letters, 1974. **25**(4): p. 233-235.
127. Yao, K., et al., *Large photo-induced voltage in a ferroelectric thin film with in-plane polarization.* Applied Physics Letters, 2005. **87**(21).
128. Choi, T., et al., *Switchable Ferroelectric Diode and Photovoltaic Effect in BiFeO3.* Science, 2009. **324**(5923): p. 63-66.
129. Yang, S.Y., et al., *Photovoltaic effects in BiFeO3.* Applied Physics Letters, 2009. **95**(6).
130. Fridkin, V.M., *Bulk photovoltaic effect in noncentrosymmetric crystals.* Crystallography Reports, 2001. **46**(4): p. 654-658.
131. Poosanaas, P., K. Tonooka, and K. Uchino, *Photostrictive actuators.* Mechatronics, 2000. **10**(4-5): p. 467-487.
132. Qin, M., K. Yao, and Y.C. Liang. *Photovoltaic characteristics in polycrystalline and epitaxial (Pb0.97La0.03)(Zr0.52Ti0.48)O-3 ferroelectric thin films sandwiched between different top and bottom electrodes*. in *20th International Symposium on Integrated Ferroelectrics*. 2008. Singapore, SINGAPORE: Amer Inst Physics.
133. Poosanaas, P., et al., *Influence of sample thickness on the performance of photostrictive ceramics.* Journal of Applied Physics, 1998. **84**(3): p. 1508-1512.
134. Peithmann, K., A. Wiebrock, and K. Buse, *Photorefractive properties of highly-doped lithium niobate crystals in the visible and near-infrared.* Applied Physics B-Lasers and Optics, 1999. **68**(5): p. 777-784.

135. Zhang, Z., et al., *Systematic Variations of Structural and electronic properties by A-site substitution in BiFeO3.*Physical Review B (Submitted), 2009.
136. Ganpule, C.S., Ph. D Thesis, University of Maryland, College Park, 2001.
137. Maiwa, H. and N. Ichinose. *Measurement of electric-field-induced displacements in (Pb, La)TiO3 thin films using scanning probe microscopy*. in *17th Meeting on Ferroelectric Materials and Their Applications (FAM-17)*. 2000. Kyoto, Japan: Inst Pure Applied Physics.
138. Buhlmann, S., et al., *Size effect in mesoscopic epitaxial ferroelectric structures: Increase of piezoelectric response with decreasing feature size.* Applied Physics Letters, 2002. **80**(17): p. 3195-3197.
139. Kalinin, S.V. and D.A. Bonnell, *Imaging mechanism of piezoresponse force microscopy of ferroelectric surfaces.* Physical Review B, 2002. **65**(12): p. 125408.
140. Hellwege, K.H., et al., Numerical Data and Functional Relationships in Science and Technology 16, Springer Verlag, Berlin, 1981.

List of Publications:

1. "Effect of La substitution on the properties of $BiFeO_3$ films prepared by Pulsed Laser Deposition", Ngeah Theng Chua, Lu You, Zhen Zhang, Kui Yao, Lang Chen, Jan Ma, Junling Wang. (Submitted to Phys. Rev. B)
2. "Properties of $(K,Na)NbO_3$-based Lead-free Piezoelectric Films Prepared by Pulsed Laser Deposition", Ngeah Theng Chua, Lu You, Jan Ma, Junling Wang. (Submitted to Thin Solid Films)
3. "Influence of Oxygen Pressure on the Ferroelectric Properties of Epitaxial $BiFeO_3$ Thin Films by Pulsed Laser Deposition", Lu You, Ngeah Theng Chua, Kui Yao, Lang Chen, Junling Wang, Phys. Rev. B, 80, 024105 (2009).
4. "Development of Lead-free Piezoceramic", Ngeah Theng Chua, Junling Wang, and Jan Ma, Advanced Structural and Functional Materials for Protection, edited by W. Lau, S. H. Min, L. N. Sua et al. (Trans Tech Publications Ltd, Stafa-Zurich, 2008), Vol. 136, pp. 63-66.